

2005

Adaptive beam shaping using electro-optic micro-lenses and hybrid acousto-optics

Yasser A. Abdelaziez
University of Dayton

Follow this and additional works at: https://ecommons.udayton.edu/graduate_theses

Recommended Citation

Abdelaziez, Yasser A., "Adaptive beam shaping using electro-optic micro-lenses and hybrid acousto-optics" (2005). *Graduate Theses and Dissertations*. 7.
https://ecommons.udayton.edu/graduate_theses/7

This Dissertation is brought to you for free and open access by the Theses and Dissertations at eCommons. It has been accepted for inclusion in Graduate Theses and Dissertations by an authorized administrator of eCommons. For more information, please contact mschlange1@udayton.edu, ecommons@udayton.edu.

Adaptive Beam Shaping using Electro-Optic Micro-lenses and Hybrid Acousto-Optics

Submitted to the School of Engineering of the
UNIVERSITY OF DAYTON

in Partial Fulfillment of the Requirements for

the Degree

Doctor of Philosophy in Electrical Engineering

By

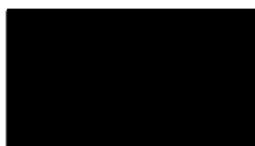
Yasser A. Abdelaziez

UNIVERSITY OF DAYTON

May 2005

ADAPTIVE BEAM SHAPING USING ELECTRO-OPTIC MICRO-LENSES, AND HYBRID ACOUSTO-OPTICS

APPROVED BY:



Partha P. Banerjee, Ph.D.
Advisory Committee Chairman
Professor and Chair, Electrical and
Computer Engineering Department



Guru Subramanyam, Ph.D.
Committee Member
Associate Professor, Electrical and
Engineering Department



Andrew Sarangan Ph.D.
Assistant Professor, Electrical and
Computer Engineering Department



Khalid Lafdi, Ph.D., D.Sc.
Resident Scientist, UD Research
Research Institute and Adjunct
Adjunct Professor, Materials
Engineering Department



Donald L. Moon, Ph.D.
Associate Dean
Graduate Engineering Program & Research
School of Engineering



Joseph E. Saliba, Ph.D., P.E.
Dean, School of Engineering

Abstract

The control of laser beam shape is of great importance for many applications, such as imaging, telecommunications and materials processing. The ability to adaptively implement this process will add another degree of freedom to further enhance its modularity. In this work we explore two different techniques to achieve such goal.

In the first technique we implement and characterize adaptive electro-optic micro-lens array. By splitting the optical beam wavefront and/or distorting such wavefront, one can achieve beam shaping. We provide the basis for such systems using electro-optic microlenses. Since characterization of microlens arrays is quite challenging, the adaptive microlens characterization will provide another hurdle for rapid device prototyping. We introduce, for the first time, a simple technique that allow for in-situ characterization with minimum tools required. Using a simple z-scan we can determine the microlens focal length and characterize its aberration properties. We have used finite element analysis to model the lenslet array and found the model is in agreement with the measured data. We also address lens design and optimization issues to achieve aberration free optical system.

Second, we implement hybrid acousto-optics with feedback for beam shaping. We demonstrate that using electronic feedback one can obtain beam shaping in a hybrid acousto-optic device. Feedback as used and illustrated in the dissertation helps to generate the additional sound pressure which can give additional beam shaping. Previous analysis of hybrid acousto-optic devices with feedback have been restricted to plane wave

treatments only. We show that over a region of convergence, one can achieve beam shaping by using the detected optical output and feeding it back electronically, together with the external radio frequency (RF) input signal. This is fundamentally different than just increasing the electrical input to the transducer. In general, we can also select, in this way, a certain range of spatial frequencies at the optical detector and use this for feedback purposes. We can selectively feed back a range of spatial frequencies of the optical beam, and hence have better control over the resulting beam shape.

To my Parents to whom I will always in debt, for without their perseverance and support, nothing would have ever happened

To my Wife whose patience made it possible for this work to be completed

To my Brother, Sister In-law and Sister for their all positive support

To my kids Rahaf and Ammar for putting a smile on my face

What I have learned from working in Optics is that:

95% of getting the job done relies on the experimental setup

Good optical alignment is vital: you have to know your forest well

to be able to pick up the right tree

*There can be no compromise in sensitivity, accuracy or precision for
good measurements*

Acknowledgments

Thanks to many people, and in spite of all the odds against it, this work is finally complete. Without their support the challenging task of completing this work would have been impossible.

I am indebted to my advisor, and department chair, Professor Partha Banerjee for his dedication and immense efforts in helping bring this work to conclusion. Whether on campus or off campus, I always enjoyed Dr. Banerjee's depth of knowledge and his sense of humor. I would like to thanks Professors Guru Subramanyam, Andrew Sarangan, and Khalid Lafdi for their participation in my committee and having their doors always open for me; Professor John Loomis for his positive contribution to my z-scan program; Dr. Dean Evans for his positive support during the entire course of my first project and supporting me financially; Dr. Donald Moon for always supporting me; Osama Meselhi, and Ahmad El-Kadi, my friends, for proof-reading and helping with my programs. It has been a humbling experience to be just around such group of dedicated and strong professionals.

Also, I would like to extend my appreciation to ECE department staff members, Loretta Christon, Colleen Hyland, and Rebecca Ossio for helping me on a wide array of administrative work; Lisa Hauk who received me here on my first day and made things looks much simpler; Prathan Buranasiri and George Nehmetallah for helping with my experimental environment; Aziz Mahfoud for helping with the SPIE travel grants; and

Marilyn Knisley for being so patient and understanding during the dissertation submission process. Thanks to all for making me feel at home.

I would like to extend my gratitude to my wife Ilham, and kids Rahaf and Ammar, who sacrificed a lot during this difficult period, my parents, brother, sister, and sister in-law for cheering me on, and my friends, Tarek Sobeih, Ahmad El-Kadi, Tamer Orabi and Mustafa Zoghoul for helping and believing in me.

Preface

The ability to adaptively implement laser beam shaping will add another degree of freedom to further enhance optical system modularity. In this dissertation we explore the basis and means upon which such modules can be realized.

Table of Contents

Abstract.....	iii
Acknowledgments.....	vii
Preface.....	ix
Table of Contents.....	x
List of Figures.....	xiii
List of Tables.....	xix
Chapter 1.....	1
Background.....	1
1.1 Introduction.....	1
1.2 Beam Shaping Techniques.....	3
1.3 The Scope of This Research.....	5
1.4 Miniaturization and Microsystems.....	5
1.4.1 Background.....	6
1.4.2 Micro-optics Technology Applications.....	7
1.4.3 Why Microlens Module?.....	10
1.5 Elements of Lenslet Array Module.....	11
1.5.1 PLZT: Material of Choice.....	11
1.5.2 Microlens Arrays: A Brief Review.....	12
1.5.3 Variable Focal Length Microlenses.....	13
1.6 Acousto-optics Background.....	15
1.7 Dissertation Organization.....	16
Chapter 2.....	18
Microlens Testing and Theoretical Foundation.....	18
2.1 Summary.....	18
2.2 Electro-optic effect.....	18
2.3 Current microlens structure.....	19
2.4 Microlens testing background.....	20
2.4.1 Our Approach.....	23
2.5 General Formulation of the Problem.....	25
2.6 Diffraction (wave) picture.....	26
2.6.1 Fresnel Diffraction Approximation.....	27
2.6.2 The Z-Scan Method.....	28
2.6.2.1 Aperture effects.....	34
2.6.3 Fraunhofer Diffraction Approximation.....	37
2.6.4 Focal Length Obtained from Diffraction Size.....	39
2.7 The Geometrical Picture of the Z-scan.....	40
2.8 Effect of Applied Electric Field on Focal Length.....	43
Chapter 3.....	46
Device Design, Fabrication, and Testing Setup.....	46
3.1 Summary.....	46
3.2 Device Design and Layout.....	46
3.3 Device Fabrication.....	48
3.3.1 Wafer Cleaning.....	49

3.3.2	Lift-off Lithography.....	49
3.2.3	ITO/Pt deposition and Electrode Formation	51
3.2.4	Device packaging.....	51
3.3	Electro-optic Properties Testing	52
3.4	Micro-lens Array Testing.....	54
Chapter 4	55
Simulation and Experimental Results	55
4.1	Summary	55
4.2	PLZT EO Properties	56
4.3	Finite Element Simulation Results	58
4.3.1	Electrostatic Field Effects	60
4.3.2	Focal Length Estimation	61
4.3.3	Effect of Electrode Widths.....	68
4.4	Experimental Determination of Focal Length	74
4.5	Experimental Results	76
4.6	Micro-lens Array Results.....	78
4.6.1	Aperture Effects	79
Chapter 5	82
Beam Shaping using Hybrid Acousto-Optics with Feedback	82
5.1	Summary	82
5.2	Background.....	82
5.3	AO Cell Spatial Transfer Functions for near-Bragg Incidence	84
5.4	Acousto-optics with External Feedback	90
5.5	Simulation Scheme and Results.....	92
5.6	Concluding remarks: effect on noise cancellation	98
Chapter 6	101
Hybrid Acousto-Optics Beam Shaping Results	101
6.1	Introduction.....	101
6.2	Experimental Setup.....	101
6.3	Feedback Circuit	103
6.3.1	Background.....	103
6.3.2	Circuit Used in Our Experiment	104
6.3.3	Our Feedback Circuit.....	105
6.4	Experimental Results	106
6.4.1	Feedback Circuit Results	106
6.4.2	Beam Shaping Results	106
Chapter 7	110
Discussion and Conclusions	110
7.1	Summary	110
7.2	Microlens Fabrication Process.....	110
7.3	Microlens Characterization and Performance Optimization.....	112
7.3.1	Microlens Tuning Range.....	113
7.3.2	Electrode Design Optimization and Aberration Control	114
7.3	Future Work for PLZT-based Microlenses.....	116
7.4	Hybrid AO Beam Shaping; Comments and Future Work	117
Appendix A	119

A.1 Beam Shaping Using Zero-order Feedback	119
A.2 Beam Shaping Using First-order Feedback	123
A.3. Z-Scan Program	128
Bibliography	130

List of Figures

- Figure 1.1 A Gaussian beam (left) is usually preferred to obtain highest possible energy concentration. A typical Eximer laser beam (center) used for laser ablation, in the unmodified mode, that result in reduced performance. The output of a Nd:YAG laser used for cutting that appears to be more flat topped. (Images courtesy of SPIRICON, Inc.)
- Figure 1.2 A misaligned (left) and aligned (right) flat-top Eximer laser used for ablation. This indicates the importance of being able to look at the beam profile and the consequence of miss-alignment on the laser performance. (Images courtesy of SPIRICON, Inc.)
- Figure 1.3 The proposed PLZT based modules for excitation and detection for capillary electrophoresis (CE) system in a CD arrangement. Parts (1) and (3) represent the fixed lower and upper parts of a CD drive, where excitation signal and detection takes place respectively. Part (2) represents the disposable or frequently used CE or bio-analytical chip under test.
- Figure 1.4 Various electrode shapes demonstrated and suggested by different authors to achieve variable focal lens using PLZT.
- Figure 2.1. The PLZT microlens design with annular electrode that has inner and outer radius of r_1 , and r_2 respectively as indicated in reference [91].
- Figure 2.2. A depiction of the experimental layout.
- Figure 2.3 3-D representation of the on-axis Z-scanned Intensity for positive and negative lenses (a) without diffraction effects, and (b) with diffraction effects.
- Figure 2.4. A 2-D representation of the z-scan shown in Figure 2.3a; (a) the normalized irradiance variation along the scanning distance; (b) the normalized slope at $\Delta z = 0$
- Figure 2.5. A 2-D representation of the z-scan shown in Figure 2.3b showing aperture size diffraction effects; (a) the normalized irradiance variation along the scanning distance; (b) the normalized slope at $\Delta z = 0$.

- Figure 2.6. 3-D representation of the z-scan using $20\mu m$ probing beam; (a) without aperture diffraction effects; (b) including diffraction effects.
- Figure 2.7. A 2-D representation of the z-scan shown in Figure 2.6a for probing beam of $20\mu m$ size; (a) the normalized irradiance variation along the scanning distance; (b) the normalized slope at $\Delta z = 0$.
- Figure 2.8 Irradiance peaks are slightly to the right of the focal length locations. The shift gets larger as the focal length gets longer.
- Figure 2.9 A close-up of the z-scan in Figure 2.7. By accounting for increasing the Z and subtracting Δz from Z , the observation distance, we shift the irradiance maxima location to exactly the focal point.
- Figure 2.10 A trace of the normalized maximum on-axis irradiance values; (a) without any aperture diffraction effects; (b) with aperture diffraction effects. Note that the scanning distance increased with the increase of the aperture size.
- Figure 2.11 The effect of probing beam size on slope of the normalized on-axis irradiance as a function of the focal length. Note that $q_0 = p_0$.
- Figure 2.12. Simulated on-axis normalized irradiance as a function of the focal length of the lens under test placed at a fixed distance $\Delta z = \pm 5q_0 = \pm 5p_0$ while changing the applied voltage. Comparing to Figure 2.3b, it represents a cross-section at fixed Δz towards the end of the scanned distance.
- Figure 2.13 On-axis far-field intensity obtained by Fraunhofer diffraction approximation
- Figure 2.14 The experimental setup layout based on the geometrical (ray) optics explanation.
- Figure 2.15 An illustration to the difference in the maximum on-axis intensity between the ray and wave optics.
- Figure 2.16 Simulated focal length (a), and refractive index (b) dependence on the applied voltage.
- Figure 3.1 4" mask design layout generated by AutoCAD. Note that each die area has a difference lens dimensions and various lenslet array packing density.
- Figure 3.2 A Close-up for one set of dies from the mask illustrated in Figure 3.1; (a) a 500/1000 μm inner/outer electrode diameters; (b) 200/600 μm lens array.
- Figure 3.3 Fabrication steps of an electro-optic module: (a) PLZT wafer lapping and polishing to the desired thickness, (b) photolithography for electrode

structure definition, (c) ITO/Pt deposition, (d) photoresist removal and ITO/Pt annealing, (e) repeating steps (b-d) on the other side of the wafer, (f) laser micromachining of the contact vias in a plastic wafer, and (g) bonding the top and bottom wafer to the plastic wafers and filling up the vias with conductive epoxy for the final PLZT module package

- Figure 3.4 An illustration of the PLZT microlens array packaging module. The PLZT substrate is sandwiched between 2 plastic holders that have been formed using precision machining.
- Figure 3.5 The experimental setup for the electro-optic coefficient and light modulator measurements.
- Figure 3.6 The experimental setup for the programmable micro-lens array measurements. This setup can be utilized for lens aberration studies as well.
- Figure 4.1 Refractive index variation as a function of the wavelength for a PLZT 9/65/35 substrate. These results were obtained using ellipsometry.
- Figure 4.2 The EO measurement results, (a) the normalized intensity variation with applied electric field, (b) the phase variation induced due to applied electric field, (c) the relative change induced in the PLZT due to the applied electric field, and (d) the quadratic fit of the experimental results of the phase variation, where Equation 2.52 was used to extrapolate the quadratic EO coefficient.
- Figure 4.3 The estimated PLZT microlens focal length variation based on the EO coefficient determined experimentally by using Equation 2.54.
- Figure 4.4 (a) The adaptive mesh generation using FEMLABTM, and (b) The surface plot of an induced electrostatic potential due to an applied voltage of 180 V.
- Figure 4.5 Cross-sectional slice of the PLZT microlens structure under test. Note that the cross-section is along the x - z direction and represents one-half of the lens structure. If we revolve this cross-section around the z -axis we will obtain a cylinder where the lens aperture lays in middle, with inner and outer radiuses of r_1 , r_2 .
- Figure 4.6 Surface and contour plots for the induced electrostatic field within the PLZT due to 300 V applications; (a) the z -component, and (b) the r -component. Note that the horizontal axis is r while z is the vertical axis.
- Figure 4.7 The radial change, i.e. x - y plane, of the electrostatic field components as a function of r ; (a) z -component, (b) r -component. These are 5-level cross-

sections at 100 μm intervals in the z -direction, hence the electric field variation at different heights of the PLZT substrate thickness.

- Figure 4.8 Utilizing Equation 2.48 one can obtain surface and contour plots for the Δn change within the PLZT material; (a) x -polarization, and (b) y -polarization.
- Figure 4.9 The corresponding radial change of Δn at 100 μm intervals in the z -direction; (a) x -polarization, (b) y -polarization. Note the total resemblance with the z -components of the electrostatic potential.
- Figure 4.10 The net phase change due to various applied voltages. Note that we have a fill factor of 80%. Hence, we calculate the phase over 80% of the lens aperture. The plots are for $\frac{1}{2}$ of the lens aperture, since we have circularly symmetric lens design.
- Figure 4.11 Surface and contour plots of the electrostatic field variation, z -component as a function of electrode width. Note that as the electrode widths increase the field changes becomes less.
- Figure 4.12 The net phase variation for various electrode widths at 300 V.
- Figure 4.13 Effect of electrode width on the focal length variation. Note that the focal length values are moving towards saturation as the electrode width becomes very large.
- Figure 4.14 On-axis slope as a function of focal length. This is simulated data for longer focal length lenses.
- Figure 4.15 The measured on-axis irradiance as a function of Δz for various applied voltages. The quadratic fit is based on Equation 2.43.
- Figure 4.16 A comparison between the simulated and measured focal lengths.
- Figure 4.17 The AFM scan of polished PLZT wafer using the blocking technique described in [110].
- Figure 4.18 Packaging of the electro-optic module: (a) laser micromachined vias etched in a 2" plastic wafer, and (b) the final PLZT packaged module.
- Figure 4.19 (a) A $1cm^2$ die diced off a 4" wafer. The wafer's thickness was 500 μm and contains 57 dies with various lens design. As mentioned in Chapter 3; (b) the packaged device that was tested.
- Figure 4.20 A mini-picture of the experimental testing of the micro-lens array at different applied voltages, (a) at 50 V, and (b) at 150 V.

- Figure 4.21 A photograph sequence taken by SPIRICON laser beam profiler of the diffraction pattern, of a lenslet, variation as a function of the applied voltage. The lenslet was set before the focal point of the external lens such that a Gaussian beam much larger than its aperture.
- Figure 4.22 The inner lobe size of Airy pattern as a function of the applied potential. The lens under test was located before the focal point of the external lens f_2 .
- Figure 4.23 The measured on-axis intensity variation of the inner diffraction lobe with the applied voltage. Note the quadratic dependence, as indicated by Equation 2.32. This also means that the focal length decreases with higher voltages values.
- Figure 5.1 Diagram of the sound-light interaction.
- Figure 5.2 AO transfer functions as a function of spatial frequency for (a) the 0th order and (b) the -1st order with $Q \cong 21$ (corresponding to acoustic frequency of 40 MHz).
- Figure 5.3 (a) The spectrum of input Gaussian profile with a beam waist of $75\mu m$. (b) the spectrum of processed profile with $\alpha_0 = 0.35\pi$ at acoustic frequencies 30/40/50/60 MHz, which correspond to $Q = 11/21/32/46$, respectively.
- Figure 5.4 Schematic of AO interaction in the presence of feedback, according to Equation (5.16).
- Figure 5.5 The details of the feedback stage necessary for the beam-shaping scheme. The input is $V_{det} = R\kappa P_{det}$, with κ is the responsivity of the photodetector and P_{det} is the detected power. The output is V_{fdbk} .
- Figure 5.6 The effect of feedback on the AO transfer function, a) 0th order and b) -1st order. The sound frequency is taken as 45 MHz, which is equivalent to $Q = 26$. In this simulation $\alpha_0 = 0.35\pi$ and the incident power is 10 mW.
- Figure 5.7 Beam shapes for an $75\mu m$ incident beam of 10 mW, corresponding to the parameters in Figure 5.6 for (a) 0th feedback, and (b) -1st order feedback. The far-field distance is 1 meter.
- Figure 5.8 A cross section of the 0th order beam shapes from Figure 7. (a) 0th order feedback, and (b) -1st order feedback.
- Figure 5.9 (a) The $\Delta\alpha$ variation with the feedback amplifier gain factor G for various initial α_0 for 0th order feedback; (b) the corresponding normalized power detected in the undiffracted order; (c) The $\Delta\alpha$ variation with the feedback

amplifier gain factor G for various initial α_0 for -1^{st} order feedback; (d) the corresponding normalized power detected in the undiffracted order.

- Figure 5.10 The spatial filtering of the high frequency noise as detected from -1^{st} diffracted order. (a) Added high frequency noise in the spatial domain; (b) the detected signal without noise; (c) 3-D representation as a function of the feedback factor.
- Figure 6.1 An illustration of the beam shaping experimental layout.
- Figure 6.2 Experimental setup photographs, (a) a general view, and (b) a close up to the feedback circuit.
- Figure 6.3 A depiction of (a) 1-stage difference amplifier, and (b) 3-stage difference amplifier.
- Figure 6.4 A simplified block diagram for the *AD620 IA* from Analog Devices. The gain is controlled only by R_G .
- Figure 6.5 Simulated Optical beam shapes because of various V_{rms} values.
- Figure 6.6 Cross sections of the optical beam showing the beam shaping effects are taking place only in (a) the x-direction, (b) while the Gaussian shape is preserved along the y-direction. Note that the amplitude of the beam in the y-direction is reduced as the total beam energy is reduced.
- Figure 6.7 Snap shots of the experimental results using SPIRICON beam profiler. A quick comparison with Figure 5. indicates a similar beam shaping trend, however, at higher V_{rms} values, we do not achieve similar shape. We believe this is due to the alignment accuracy.
- Figure 7.1 Surface and contour plots of the induced change in refractive index for x-polarization for PLZT substrate thickness of $50\mu m$ and electrode width of $25\mu m$. Note that the lens aperture diameter is $50\mu m$, and the inner aperture size ratio w.r.t. electrode width is the same as the $500\mu m$ diameter lens discussed in Chapter 6.
- Figure 7.2 Surface and contour plots of the relative change of refractive index in the x-polarization for (a) Trapezoidal and (b) elliptical electrode configurations.

List of Tables

- Table 4.1 The fitting coefficients of Equation 4.3 for the simulated net $\Delta\phi$ for various applied voltages and the corresponding focal length based on Equation 4.5.
- Table 6.1 The gain values of the feedback circuit and the corresponding output voltage and RMS value of the RF signal. These values correspond to 0.5 V input signal to the feedback circuit.
- Table 7.1 The calculated relative phase error in radians due to different electrode configurations and PLZT substrate thicknesses. Note that we kept the ratio between the electrode widths to lens aperture the same.

Chapter 1

Background

1.1 Introduction

One important consideration in an optical system is the characteristics of the optical beam that passes through that system to deliver energy, power, or information in appropriate and efficient manner [1]. Thus, the ability to control laser beam shape becomes of great importance for many applications, such as imaging, telecommunications and materials processing.

Laser beam shaping, LBS, can be defined as the art of controlling the amplitude and phase of that beam [2]. The benefit of controlling laser beam shape can be seen in improving on the uniformity and brightness for imaging and interferometry. Furthermore, the challenge of image resolution and quality depends mainly on the optical beam properties [1]. Also, in materials processing, the delivery of uniform energy during laser ablation is crucial [3]. Another application is lithography, where laser application demands well controlled beam to enhance resolution, and registration errors from one layer to another and overall process yield [4]. In addition to lithography, tightly focused laser beams are essential in components' trimming process in the integrated circuit (IC) industry. This is necessary for achieving excellent matching, e.g. resistor elements, for excellent device performance control [5]. Numerous applications

can benefit from LBS such as laser printing, optical data storage, isotope separation, optical metrology, and medical applications [2].

It is very hard to cover all applications in more detail due to constraints of time and space. Figure 1.1 and 1.2 shows several examples of laser beam profiles for Eximer and Nd: YAG lasers. It is important to notice that laser beam shape optimization is application driven. Furthermore, alignment of optical systems is crucial in affecting the overall performance.

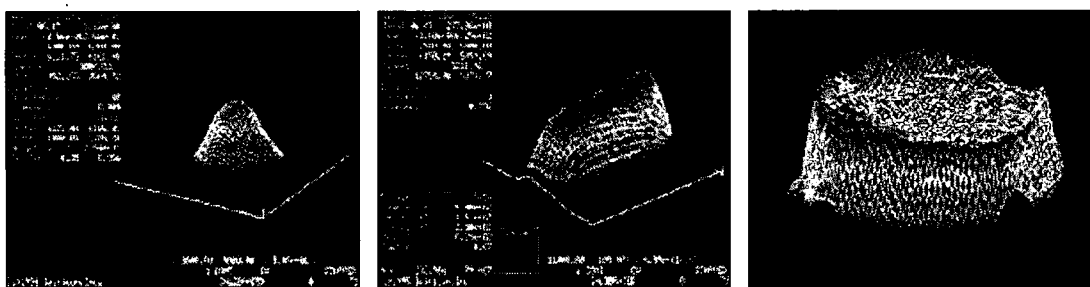


Figure 1.1 A Gaussian beam (left) is usually preferred to obtain highest possible energy concentration. A typical Eximer laser beam (center) used for laser ablation, in the unmodified mode, that result in reduced performance. The output of a Nd:YAG laser used for cutting that appears to be more flat topped. (Images courtesy of SPIRICON, Inc.)

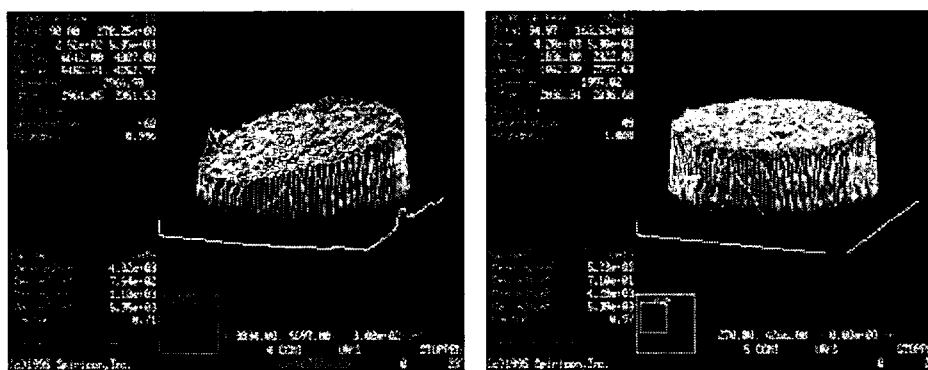


Figure 1.2 A misaligned (left) and aligned (right) flat-top Eximer laser used for ablation. This indicates the importance of being able to look at the beam profile and the consequence of miss-alignment on the laser performance. (Images courtesy of SPIRICON, Inc.)

It is difficult to present a brief history of laser beam shaping since most of this work has been done in industry where they consider such information as proprietary [2].

1.2 Beam Shaping Techniques

There are several techniques that can be implemented for controlling laser beam shape. In this section we will summarize some of such major methods.

Array generation involves an optical system that splits an incoming beam of light into an array of beamlets. This configuration is implemented for multiple imaging, illumination of array of optoelectronics devices, and beam shaping. Lenslet arrays are used as phase gratings that have many diffraction orders with equal intensity. In this case distributed index lens is used with pinholes gratings placed at the focus plane of the lenslet array to alleviate the uniformity problem of the generated array [6].

Computer generated beam shaping and focusing optical elements for laser material processing has also been researched. Theoretical and experimental investigation has been conducted of computer generated optical elements having microstructures on planar substrates. The optical elements are based on the idea of matching the wavefront phase by a Fresnel zone plate not only at the zone border, but also within the zones. For this purpose rigorous diffraction theory has been used [7].

Efficient beam shaping of linear, high power diode laser by use of micro-optics has also been investigated. Diffractive micro-optical elements have been used for beam shaping to optimize the coupling of an incoherent, linearly extended high power diode laser into multi-mode fibers. The devices use two aligned diffractive optical elements (DOE) in combination with conventional optics with 28% coupling efficiency. An improvement of the coupling efficiency of 50% can be achieved using gray-tone

elements. Since high power diode laser have low spatial coherence, coherent beam shaping elements are not suitable. This case therefore requires an incoherent beam shaping method [8].

Also, for photolithographic projection systems, beam shaping optical elements have been proposed to create a unique intensity distribution along the optical axis, where the highest depth of focus is achieved with hyper Gaussian ring, whose transmission function is similar to an annulus. But since a high depth of focus (DOF) requires a small annulus, only a small amount of energy passes through the imaging system. Therefore the use of phase only filters that produces non-diffracting optical beams has been suggested in addition to lenses in the optical system. A shift in the focal point may occur, but the focal depth cannot be changed [9].

Also, it has been shown that a small spot size in an optical recording system can be accomplished by changing the optical system F number, while the beam shape can be altered by inserting a phase filter in the beam path or operating the laser in doughnut mode [10].

Finally, optical beam shaping has been demonstrated using polarization effects. In principle, an aperture whose transmission varies from point to point over its cross section can suppress secondary diffraction maxima, and thus profile laser beams. By using the EO crystals and polarizer combination, beam profiling can be achieved [11].

From the forgoing discussion, we find that micro-optics plays a crucial rule in beam shaping. In addition diffractive optics takes also a prominent rule. It is our intent in this dissertation to build the foundation for utilizing adaptive micro-optics and adaptive gratings in laser beam shaping. Such adaptive techniques will not only give a better

control over the desired beam shape, but also will allow for building more modular systems.

1.3 The Scope of This Research

As seen in the previous section, laser beam shaping is quite a challenging area. Furthermore, our goal to introduce the adaptive element as a factor for better control over the beam complicates matters more. Thus, it is impossible to cover the topic precisely and treat it efficiently as one would hope for. We believe that one may combine several techniques in one application to control the beam shape, namely adaptive microlens arrays. We will show that one can control the focal length, phase and general lens properties of an electro-optic microlens by varying the applied voltage and adjusting electrode shape. In addition, one may use induced adaptive gratings, e.g. acousto-optics (AO) interaction, to achieve the same goal.

It is our intent to cover only the above two subjects. First, we will address electro-optic microlens modeling and characterization. This will serve as the main tool by which one can set it up in applications pertaining to laser beam shaping, as described earlier [6]. Second, we will utilize a novel technique, namely electronic feedback of the detected optical signal to adaptively change induced gratings strength in an AO cell, and hence exercise adaptive control over the beam shapes of the resulting undiffracted and diffracted orders.

1.4 Miniaturization and Microsystems

This dissertation work is of relevance to miniaturization and microsystems. Having this in mind, it would be educational if we overview MEMS applications. Also, this

discussion would not be complete without pointing out some of the issues related to microsystems integration and adaptive microlens rule in the current MEMS applications.

1.4.1 Background

Over the past two decades the advances in semiconductors, miniaturization technologies have grown rapidly with dimensions comparable to the wavelength of light [12]. Parallel to that, Micro-Electro-Mechanical Systems (MEMS) [13], that is based on such technologies has evolving and outgrown its founder technology, namely VLSI. The ambitious dream of miniaturization of complete functions and systems for different applications has been paving the way to introduce new ideas and techniques to produce such devices. Nowadays, the field of MEMS has been split, based on applications, into MOEMS [15, 16], Bio-MEMS [17] and NMEMS [18]. Such acronyms stand for optical, biological and Nano-applications respectively with sub-titles such as Bio-Photonics [19] as a subset of Bio-MEMS and MOEMS. For MEMS, as an enabling technology, the objectives will always drive the technology. A wide array of applications has been demonstrated. Automotive applications such as pressure sensors [20], gyroscopes [21] and accelerometers [22] to information and telecommunication applications [23] such as 3-D memories [24], micro-relays [25], optical switches [26] displays [27] and tunable filters [28] have been realized. With more advances in new, cheaper production techniques, health and biotechnology application have gained major interest. Diagnostics [29], invasive [30], non-invasive surgical instruments [31], drug delivery [32], and discovery [33] devices have been demonstrated. Finally, instrumentation based on micro-fabricated devices is coming more into commercial use such as pressure [34], food quality [35] and shock sensors [36].

The most crucial element of MEMS technology is materials. Materials' use for MEMS will affect the way we are making devices, their functionality and reliability [37, 38]. For these reasons, a careful consideration of materials implemented is necessary. Initially, silicon has been the dominant material for MEMS [13], but gradually other materials have evolved such as GaAs [39], InP [40], SiC [41], polymers [42], functional ceramics [43] etc., and other functional materials have been used for various applications. Since the objective of MEMS is the realization of a specific function, it is worthwhile to use materials that are optimized for such application.

1.4.2 Micro-optics Technology Applications

Micro-optics technology, or MOEMS as preferred by some, is an area of research that addresses wide a variety of applications. Wide and diverse as the MEMS field itself, micro-optics serves the telecommunication [23], displays [27], biosensors [44], optical detection [45] and imaging [46] industries. Microlens arrays [47] are used in lithography [48], array generation [49], interconnect [50], Steering [51] and beam shaping [52]. Also, and micro-mirror arrays are implemented in switching [53] and projection displays [27]. They also serve in building a miniature optical-bench system [54]. Integrated miniaturized optical fluorescence detection systems [55] in drug discovery and DNA sequencing have been demonstrated. Last, but not least, image intensifiers [56, 57] are basic components in commercially produced CCD image sensors nowadays. By using integrated microlenses or by using hollow micro-tubes in conductive glass one can enhance electron collection efficiency. The technological advances in flip-chip bonding [58] and multi-chip modules [59] have allowed for the integration of various active

optical materials, such as active tunable filters with passive devices such as microlenses and detectors to have a complete function [59].

In addition to the aforementioned general areas, there has been growing interest in the fabrication of integrated micro-total-analysis systems for bio-chemical analysis μ -TAS [60, 61]. μ -TAS is a means for drug discovery and DNA analysis, to name a few of their applications. In such systems, electro-kinetically driven flow in capillaries is used for electrophoretic separation of differently charged chemical species. Fluorescent dye is attached to those species, where they fluoresce upon shining laser light on them. Due to its high sensitivity, Laser Induced Fluorescence (LIF) is the most preferable method for detection [62]. Ultimately, fluid pumping, mixing, sampling and signal detection should be integrated to achieve a high throughput system [60].

One of the crucial components of μ -TAS is the optical detection system. Waveguides have been used for fluorescence detection [45, 63]. However, the most frequently used method for detection is confocal epifluorescence microscopy [64]. In such systems, the signal in a single channel is detected each time. In addition, the setup is bulky and limits the throughput of the entire system where multi-lane capillary is used. To get higher throughput, an array of waveguides integrated with flow channels [45] and a rotary confocal-fluorescence scanner with radial capillary array [65] are used. In the waveguide scheme, where the evanescent field is the sensing signal, an inherent conflict may be present in maintaining the light by Total Internal Reflection (TIR) and maximizing the evanescent field [45]. In the scanner scheme [65], the speed of the stepper motor for scanning should be consistent with the electrophoretic fragment velocity. This is a limiting step for the entire system; especially the detection is done one channel at a time.

To overcome the bulky optical setup of the above systems and enhance detection parallelism, several systems have been proposed and implemented [45,66-67]. In these systems, passive micro-optical elements, such as microlens arrays, diffraction gratings, and active elements such as miniaturized multi-anodic Photo-Multiplier Tube (PMT) and enhanced CCD camera are used. Such systems represent a good example of integrated μ -TAS. Those excellent systems need more modular functionality and design flexibility.

Earlier, we have proposed an integrated μ -TAS with a different perspective [68]. Disposable plastic microchips have become more dominant in bio-analytical system for their cost effectiveness, but the optical system involved is usually expensive and bulky. Therefore, system lifetime and modularity should be considered as factors in the design of the bio-analytical system. To realize such systems, we have proposed the use of a compact disk (CD) drive arrangement for bio-analytical systems [68], where the excitation and detection parts are fixed, but modular to accommodate various conditions. The proposed system is shown in Figure 1.3. The systems have four main components, one of which is signal conditioning that is not shown in the figure. The other three components are: the excitation module (1), the capillary electrophoresis (CE) chip (2), and the detection module (3). The implementation of EO ceramic, such as Lanthanum modified Lead Zirconate Titanate (PLZT) allows for various modular configurations to the optical detection system as indicated in Figure 1.3. One of the central elements to such modular configuration is variable focal length microlens array module. The microlens module utilizes both fixed and variable focal length microlens array.

1.4.3 Why Microlens Module?

In a high throughput system, it is imperative to use multi-lane capillary microchips. A CCD camera is used for detection in such arrangements. One of the technical drawbacks of miniaturization in bio-chemical analysis is the small sample volumes used. These small volumes limit the sensitivity of the system. It has been shown previously that light amplification of about three fold, or more, of the signal [69] can be achieved using micro-lens array. This amplification is driven from the combination of a CCD-camera objective combined with a microlens. The numerical aperture (NA), which expresses the ability a lens to collect light, is [70]

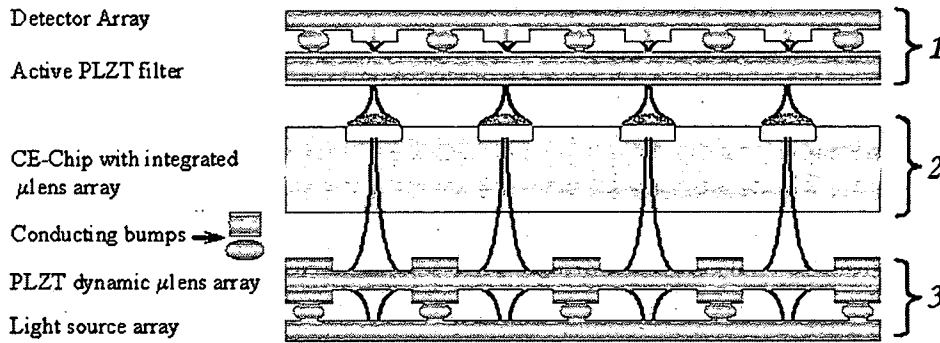


Figure 1.3 The proposed PLZT based modules for excitation and detection for capillary electrophoresis (CE) system in a CD arrangement. Parts (1) and (3) represent the fixed lower and upper parts of a CD drive, where excitation signal and detection takes place respectively. Part (2) represents the disposable or frequently used CE or bio-analytical chip under test.

$$NA = \frac{1}{2f\#}, \quad (1.1)$$

where $f\#$ is the f-number [70]

$$f\# = \frac{F}{D}, \quad (1.2)$$

where F is lens focal length, and D is the effective clear aperture. Substituting (1.2) into (1.1),

$$NA = \frac{D}{2F}. \quad (1.3)$$

By controlling the focal length, one can change the NA, for the same aperture size, and therefore enhance the system's ability to collect the signal. Upon stacking such PLZT dynamic programmable micro-lenses, one can optimize the optical system for best sensitivity, hence enhancing the signal to noise (S/N) ratio. Modular lenslet arrays can be utilized for both beam shaping and focusing of the light source and detection of florescence. The above argument is valid for other applications where weak signals are inevitable.

1.5 Elements of Lenslet Array Module

In this section, we present a brief background on the elements of the microlens array modules.

1.5.1 PLZT: Material of Choice

Lanthanum modified Lead Zirconate Titanate ceramic, PLZT, has been in use since 1971 [71]. PLZT is a class of ferroelectrics with simple oxygen octahedral ABO_3 group [72]. By applying an electrical field, the internal dipole of the crystallite (domain) realigns and causes the ceramic to act very similar to a single crystal material. The successful introduction has helped to increase the optical translucency of the conventional Lead Zirconate Titanate, PZT. The addition of La in PZT is effective in producing good transparency due to the following reasons [72]:

- 1 Lanthanum oxide has the ability to reduce the distortion, or anisotropy, of the oxygen octahedral ABO_3 , therefore reducing light scattering;
- 2 Its high solubility in the PLZT perovskite structure produces homogenous solid solutions that are free from any second phases or light scattering;

- 3 Its ability to produce significant number of lattice vacancies results in the enhancement of the densification process, control of the grain growth behavior and the promotion of a highly uniform microstructure.

PLZT constitutes a broad category of compositions most widely known for its high transparency and electrooptic effect. It is well suited for such applications as light shutters, coherent modulators, color filter, segmented displays, tunable lenses and imaging devices [72].

PLZT ceramics display optically uniaxial properties when polarized and activated with electric field. It has one unique symmetry axis, the optical axis that is collinear with the ferroelectric polarization vector, which possesses optical properties different from the other 2 orthogonal axes. There are two types of electrooptic birefringent effects within the PLZT:

- 1 Non-memory: quadratic, Kerr effect.
- 2 Memory: linear, Pockel effect.

The PLZT has the advantage of high quadratic EO coefficients, fast switching speeds, and ease of use. The PLZT ceramic composition $\text{Pb}_{0.92-0.905}\text{La}_{0.08-0.095}\text{Zr}_{0.65}\text{Ti}_{0.35}$ possess the quadratic EO effect and transparent from 340 nm to 6.5 μm range.

1.5.2 Microlens Arrays: A Brief Review

It was over 300 years ago that Hook [73], first melted rods of Venetian glass to form small lenses. These lenses have good imaging quality, and used as microscope objective to study insects. In the 1940s, Dennis Gabor [74, 75], suggested the use of arrays of small lenses, called super lenses to replicate the action of conventional large lenses with more advantages.

Since late 1980's and due to the realization of the advantage of photonics over electronics, the demand for microlens arrays have increased. New applications have been found with the advances in the fabrication technologies.

Several applications have utilized microlens arrays. Beam shaping [52] and intensity distribution of a single beam or the generation of an array of beam-lets has been realized [49]. One simple application for such lenslet is wavefront sensing, aberration correction [76], and generating array of masks for the semiconductor lithography applications [48]. In addition, they are used for interconnections where steering of arrays of independent optical information channels for optical computing and telecommunication applications are needed [51]. One last application is imaging. Macro-image can be formed from the integration of an array of beam-lets and microlens array may be utilized for 3-D imaging applications and concentrating light onto CCD arrays [77].

Several fabrication techniques have been utilized to realize microlens arrays. Selectively diffusing dopant through a mask [78] can achieve refractive index gradient, e.g. in a planar glass substrate, which produces a distributed planar lenslet array. Photothermal etching [79], photoresist reflow [80], molding [81], and ink-jetting [82] techniques have been also used to realize microlens arrays with variable properties and characteristics.

1.5.3 Variable Focal Length Microlenses

The ability to alter the focal length within an array offers the opportunity to track a moving object or to steer optical channels and therefore attracting a significant amount of interest, particularly from the optical computing community. Moreover, microlenses are also of great importance in biomedical and microfluidics as indicated earlier. This class of

microlenses can be divided into categories based on the material and principle used. Electrically tunable microlenses utilize the electro-optic (EO) properties of liquid crystals (LC) [83, 84] and ferroelectric FE materials such as LiTaO_3 [85]. In addition, an electrically tunable microlens using liquid bubble has been demonstrated [86]. More recently hydrodynamic pressure was implemented to have adaptive microlenses for microfluidics network applications [87]. For the purpose of our current research, we will address only EO tunable microlenses that utilize PLZT ceramics.

LC materials alter their refractive index as a function of the applied voltage. LC layers have been utilized in conjunction with the reflowed photoresist microlens, and sandwiched between two glass layers to achieve focal length variations [83]. In addition, several authors have used a variety of electrodes shapes and configurations not only to vary the focal length, but also to steer an optical beam. The advantage of using LC is the low voltage required to operate [83]. However, the drawback is the associated higher value of aberration with LC lenses, and low switching speeds [80]. The reason behind that is the LC layer is thinner at the center of the lens so the resistance of deformation is greater and molecules are tilted less. This leads to higher refractive index at the center of the lens and reaches only to its ordinary values at the edges. This factor coupled with the pre-tilt of the molecule is distorted by the high contact angle where the lens meets the substrate [80]. More recently, a polymer network LC (PNLC) has been fabricated and tested [84], but a major concern is its long-term stability. The reason behind this is the destruction of the polymer network due to continuous application of the driving voltage [85]. This in turn reduces the focusing capability of the microlens. Another issue with the

LC tunable lenses is its sensitivity to polarization that limits their applications to a specific direction.

PLZT: Fe ceramics with their high quadratic EO coefficient have been utilized as well for adaptive lenses [88-89]. PLZT have advantage over the LC lenses due to its solid-state nature, large quadratic EO coefficient, fast switching, multicolor capability, and its wide range transparency from near UV to mid infrared [72]. Several researchers have utilized various electrodes configurations, as shown in Figure 1.4, to achieve focal length variations. Due to the interdigitated or arrayed electrodes' structure, they have inherent diffraction effects that degrade optical information [88-89]. More recently, an annular electrode structure has been proposed [90] as shown Figure 1.4c., and the theoretical background and modeling of such adaptive micro-lens has been carried out. However, this design has not been realized by the author [91]. This design, with its ring electrodes structure, is simple to realize, free of diffraction effects and allows for the maximum possible fill factor. It is worth noting that the microlens realized with ring electrodes can be operated in a mode that is polarization independent.

1.6 Acousto-optics Background

We have chosen acousto-optic interaction as an attractive means of controlling laser beam shaping since it has been well established field with numerous applications already in production. For over four decades, acousto-optic (AO) interactions have been extensively studied and applied to signal processing. AO modulators (AOMs) are 1-dimensional (1-D) devices in the sense that light is diffracted in the direction of propagation of the sound. The use of AOMs for image processing has been more recently explored [92-98]. The novel feature of this technique is that lensless optical

image processing can be achieved without the use of Fourier plane spatial filters. In fact, the 2-D optical image interacts with the sound fields in the AOMs, and the scattering or diffraction of the 2-D optical image actually carries the processed versions of the original 2-D input image. While 1-D image processing can be performed with one AOM, 2-D processing requires two AOMs with the sound field in each AOM propagating in the two orthogonal transverse directions.

The easiest way to understand lensless spatial filtering of images using AO is through spatial transfer functions describing AO interaction between the sound-induced moving grating and the input angular plane wave spectrum of the light field. The spatial transfer functions for an AO modulator working in the Bragg regime have been derived recently to show the spatial frequency selectivity of both the diffracted and the un-diffracted orders [92-99]. In short, under certain conditions, the undiffracted order has the characteristics of spatial high-pass filtering or spatial derivative operation [100] on the image, while the transfer function for the diffracted order shows low-pass characteristics. 2-D edge enhancement and corner detection have also been achieved with two AO cells with orthogonally propagating sound [95,101].

The processing operation is programmable in real-time by electronically varying the sound amplitude or frequency within the AOM. This means that the characteristics of diffracted and un-diffracted order can be controlled. Accordingly beam shaping can be achieved.

1.7 Dissertation Organization

The work in this dissertation is divided into two parts. Chapters 2, 3, and 4 address the microlens part, while Chapter 5 and 6 are dedicated to the AO beam shaping.

In Chapter 2 we provide the theoretical foundation for the microlens characterization. In Chapter 3 the device design, mask layout and fabrication steps are discussed. Finally further microlens device simulation using FEMLAB package and preliminary experimental results are described in Chapter 4.

In Chapter 5, the theoretical aspects of hybrid acousto-optic devices are discussed in details. Further, we provide the simulated results illustrating the effect of feedback on the diffracted and un-diffracted orders shape. The feedback circuit design and preliminary experimental results are introduced in Chapter 6.

Comments and conclusions regarding theoretical and experimental aspects of parts I and II are provided in Chapter 7. Suggestions for future work are discussed in detail as well.

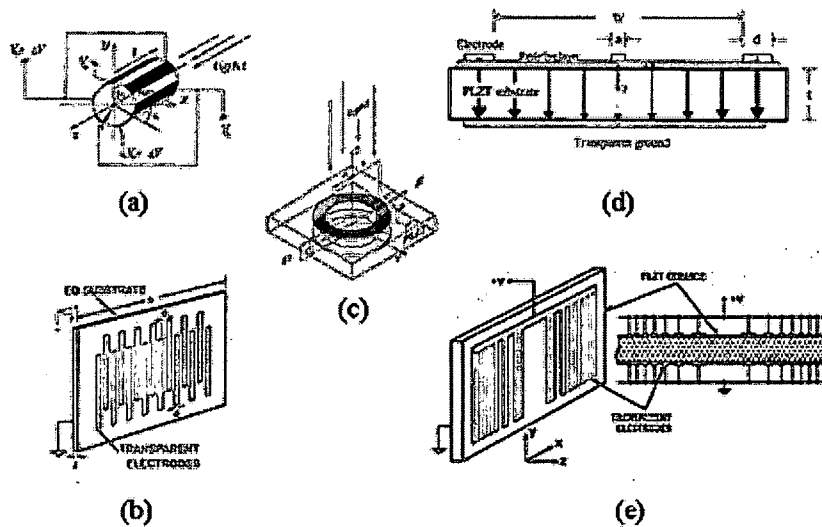


Figure 1.4 Various electrode shapes demonstrated and suggested by different authors to achieve variable focal lens using PLZT [88-90].

Chapter 2

Micro lens Testing and Theoretical Foundation

2.1 Summary

In this chapter, we will lay the foundation of the work needed to characterize the PLZT-based adaptive micro-lens array. First, we will have a brief description of the EO effect. This will be followed by an overview of the available methods for micro-lens array characterization.

Our analysis, based on wave and ray optics, for the first time to our knowledge, will provide a new method for characterizing microlens arrays. We will show that both approaches are in total agreement.

2.2 Electro-optic effect

PLZT is a polycrystalline EO material that has many advantages over single crystal EO materials such as Lithium Niobate, including ease of fabrication, low operating voltages, and reduced long-range strain effects. It also has advantage over liquid crystals and ferroelectric LC due to its solid phase nature and fast switching speeds [72]. In the absence of applied field, the PLZT is optically isotropic. An applied electric field induces refractive index anisotropy. This leads to an optical phase difference φ for the two orthogonally polarized light components passing through the material. The relative phase change, i.e. the EO response, is assumed to be quadratic, that is $\varphi \propto E^2$; where E is the

amplitude of the applied electric field. The transmission intensity I of the light through the EO system is given by [101]

$$I = \frac{1}{2} \sin^2\left(\frac{\varphi}{2}\right). \quad (2.1)$$

Where, φ is the phase change incurred during travel through the material. The relative change in the phase $\Delta\varphi$ due the applied voltage is [101]

$$\Delta\varphi = k_o \Delta n L, \quad (2.2)$$

where, $k_o = \frac{2\pi}{\lambda_o}$, L is the PLZT wafer thickness, λ_o is the incident light wavelength, and

Δn the change of the refractive index birefringence due to the applied voltage. The induced ordinary and extraordinary index of refraction is determined by

$$n_o = n_0 - \frac{1}{2} n_0^3 r_{12}, \quad n_e = n_0 - \frac{1}{2} n_0^3 r_{11}, \quad (2.3)$$

where, r_{11}, r_{12} are the quadratic EO coefficients.

$$\Delta n = n_o - n_e = \frac{1}{2} n^3 r_{eff} E^2, \quad r_{eff} = r_{21} - r_{11}. \quad (2.4)$$

2.3 Current microlens structure

Our proposed work is based on the foregoing discussion. One can induce an electric field distribution within the PLZT, which depends on the size and shape of addressing electrodes in order to induce refractive index distribution that will contribute to lensing effect. As shown in Chapter 1, several authors have demonstrated or suggested various electrode shapes for PLZT microlenses. We have chosen to work with annular ring electrodes [91] as shown below. This has the advantage of no diffraction effects due to the absence of interdigitated electrodes within the lens aperture, light polarization

independence, and better fill factor. The applied potential $\pm V_0$ on both electrodes will induce axially symmetric electric field within the PLZT substrate. As noted in Figure 2.1, the light propagation direction is the same as the applied potential. The ring electrode has inner and outer radius of r_1 and r_2 respectively.

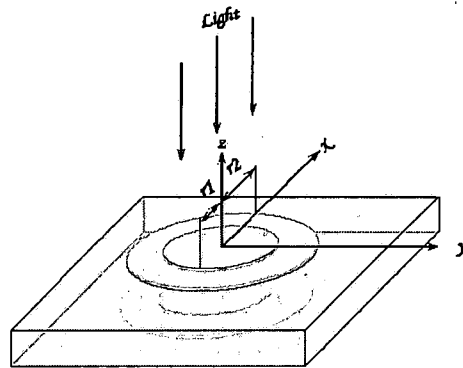


Figure 2.1 The PLZT microlens design with annular electrode that has inner and outer radii of r_1 , and r_2 respectively as indicated in reference [91].

2.4 Microlens testing background

For individual common non-planar fixed focal length microlenses the most common parameters to be measured are [80]

- Diameter
- Depth or sag
- Focal length
- Depth of focus
- Point spread function (PSF)
- Encircled energy function
- Modulation transfer function (MTF)
- Shape of wave front
- Off axis performance

- Shape of referencing surface
- Radius of curvature of the surface
- Index distribution of graded index lenses

Also, for the microlens array, one shall need to expand on the above measurements and the add the following items of interest

- Consistency of the focal length
- Fill factor
- MTF of the integral image
- Coherence of the array
- Cross talk between channels
- Stray light through interstitial areas

From the above list, we observe that the most two fundamental measurements that can completely define the lens performance is the focal length and the wavefront aberration [80]. From the wavefront aberration, other parameters such as the PSF and MTF can be deduced.

By definition, the focal point is the point on the optical axis where the intensity of the central peak of the PSF is maximized [80]. This is the circle of least confusion and is the place where the image will have the maximum spatial resolution. If the complete picture of the focal length performance is required, the paraxial focal length is given along with the description of the lens aberrations, which gives the least ambiguous results. Therefore, the wavefront aberration and diffraction effects make defining and measuring the focal point a non-trivial task [80].

At this point, we would like to point out the following distinctions between variable focal lengths, i.e. adaptive, and fixed focal length microlens arrays. First, the adaptive lenslet array is planar design, i.e. no curvature or profiles are measured. Second, the lensing effect comes from the applied voltage that induces a refractive index grading. Therefore, it will be essential for us to measure the following parameters, focal length, wavefront aberration and refractive index grading.

For a fixed focal length lenslet array, the characterization of the surface profile, surface roughness, wave aberration, and uniformity is done by using profilometric, interferometric [102] and Shack-Hartmann methods [103]. Most of these methods are precise but very elaborate, which allow only for random sampling of the microlens array. In addition, the current commercially available interferometers are not suitable for microlens characterization [80]. This leads to the necessity to custom build an interferometer, which adds another dimension of complexity. Characterizing a variable focal lenslet array will definitely make matters more difficult.

More recently, it has been shown that the average shape and aberrations of microlens array could be done only from the far field intensity distribution [104]. This elegant method has been used for getting a better picture on the whole lenslet array, and hence the statistical variations of focal length as well as lens shape and aberrations. In this method, the microlens array under test is illuminated with a plane wave beam and the far field of the transmitted field immediately behind the array is observed at the back focal plane of another lens. Because the far field intensity distribution is obtained by the Fourier transform of the field behind the lenslet array, one can obtain the amplitude and phase of wave function from intensity recording in the image and diffraction planes. Such

information may be obtained by using the algorithm introduced by Grechberg and Saxton [105]. Filtering mechanisms have been used to obtain correct results since the detected far-field intensity distribution is strongly modulated, and the Grechberg and Saxton Algorithm (GSA) shown previously will fail unless given suitable start parameters [104]. Our main task is to measure the focal lens variation as a function of the applied voltage, get the exact phase profile, i.e. the refractive index gradient, and finally have a general method from which aberration information can be obtained. In the following section, we will describe our approach with the necessary mathematical formulation of the problem.

2.4.1 Our Approach

In the previous section, we have described briefly the far-field intensity distribution method for lenslet shape and aberration characterization method. This method has several limitations and less precision due to the following reasons. The GSA requires the detailed knowledge of the intensity distribution immediately in front of the micro-lens array. This means that we must have a uniform illumination of the array. The technique makes a great demand on the detector system and restricts its measurements to 1-dimensional far field patterns and numerical apertures smaller than 0.2. Finally, the technique is only applicable to lens arrays with fill factors near unity. Such restriction originates from the application of the GSA. As the authors suggest, this restriction may be overcome by using more complex retrieving algorithm [104].

In our case of a PLZT-based adaptive lens, we have an annular metallic electrode, within which an induced refractive index grading due to the applied field occurs. This field distribution is a function of the ring electrode dimensions. Assuming uniform material structural and composition characteristic one can consider the refractive index

gradient for each element in an array is similar and hence uniform phase profile. We can state our problem as follows. We have a variable focal length with an unknown phase profile. Therefore, the use of GSA and the technique mentioned previously will not be suitable for our case. Rather we propose to start with single lens characterization. Since we assumed material uniformity, one can consider the lenslet array should have the same phase profile for each lens.

In our method, we will use the more general, and exact, Fresnel diffraction formula to derive an expression to the on-axis intensity for one lens. The detected intensity can be monitored at any suitable distance Z , which does not have to be the in the far field. Then we will introduce a simple Z -scan technique to determine the focal length. In this technique, an intensity variation plot resulting from the scanning of the lenslet under test along the beam propagation direction will provide the information about the focal length. This is of course at a specific applied voltage. This will provide an accurate unambiguous value for the focal length for the given applied voltage. In addition, we will show the on-axis intensity changes, for a fixed lens position, as a function of the applied voltage. The next step is to proceed with the complete derivation for an expression of the diffraction pattern resulting from focused Gaussian beam illumination of the lenslet, taking into consideration the lens aperture, using the Fresnel diffraction formula. Two pieces of information can be obtained from the diffraction pattern. First, we can obtain the focal length. Second, we will be able to retrieve the actual phase profile of the lenslet. By adding the aberration term to the Fresnel diffraction formula, one can extract aberration coefficients. Also, by comparing the actual phase profile with the ideal quadratic profile, one can get the aberration information.

2.5 General Formulation of the Problem

Gaussian beams represent a special solution to the electromagnetic wave equation. These beams of light have a characteristic radial intensity profile which varies along the width of the beam. Because these Gaussian beam wavefronts behave somewhat like spherical waves, we can match them to the phase curvature of the microlens to find exactly what form of beam will result from a particular gradient index of the lens.

The optical field of a Gaussian beam propagating in the Z -axis in the q -formalism has the general form of [106]

$$E(x, y, z) = E_0 \frac{q_0}{q(z)} \exp\left(-j \frac{(x^2 + y^2)}{2q(z)}\right) \exp(-jkz), \quad (2.5)$$

with the beam width at a distance z , $w(z)$, expressed as

$$w(z) = w_0^2 \left(1 + \left(\frac{z}{z_0}\right)^2\right), \quad (2.6)$$

and its radius of curvature $R(z)$ as

$$R(z) = z \left(1 + \left(\frac{z_0}{z}\right)^2\right), \quad (2.7)$$

where, w_0 is the minimum beam width or waist, and z_0 is the Raleigh length. z_0 is given by $z_0 = k_0 w_0^2 / 2$, and k_0 is the wave number.

Our proposed experimental setup is shown in Figure 2.2. The microlens under test with focal length f and aperture size of radius r , is placed around the focal point of a converging Gaussian beam, where the beam has a plane wavefront. In the two-step test, first the lenslet will be scanned for $\pm \Delta z$ distance about the focal point.

The scanned Δz range will be chosen to be a multiple of the Raleigh length, and such that the beam width at $w(z)$ at a distance Δz is smaller than the lens aperture r_o . For a scanning distance $\Delta z = nz_0$, where n is an integer, and from Equation (2.6) above

$$w(z) \approx nw_0. \quad (2.8)$$

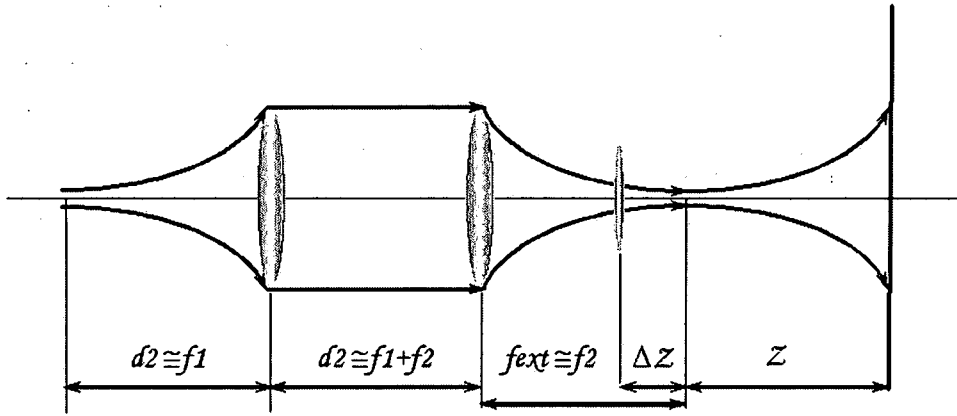


Figure 2.2 A depiction of the experimental layout.

For example, for an original beam diameter at the focal point $w_0 = 10\mu m$, the minimum lens aperture that can be used if we would like to scan for $5z_0$ will be $50\mu m$. By plotting the on-axis intensity versus the scanned distance Δz , we can infer the focal length of the micro-lens. The second step in our test is to have the lens under test in the path of light such that the beam size will be larger than the lenslet. A diffraction pattern will form. By changing the applied voltage the diffraction pattern shape will change. The focal length can be inferred from the size of the inner lobe while the diffraction pattern in general can produce information about the wave front aberration.

2.6 Diffraction (wave) picture

In this section, we will implement two approaches for the diffraction. The first uses the Fresnel diffraction approximation where the observation plane is a distance Z away from

the lens under test. Then we incorporate the Fraunhofer approximation to check for the validity of our calculation.

2.6.1 Fresnel Diffraction Approximation

From the experimental depiction in Figure 2.2, we can express the Gaussian electric field distribution a distance Δz before the lens under test as

$$E(x, y) = \frac{q_0}{q_0 + \Delta z} \exp\left(-\frac{j(x^2 + y^2)k_0}{2(q_0 + \Delta z)}\right), \quad (2.9)$$

where q_0 is the q -parameter ($= jk_0 w_0^2/2$) where the beam has plane wavefront.

Using Equation (2.6) and Fresnel Diffraction formula [106], one can express the optical field distribution right after the lens under test f , taking into consideration the lens aperture, as

$$E(x, y, Z) = \frac{jk_0}{2\pi Z} \iint \mathfrak{S}(x', y') \times \exp\left(-\frac{jk_0}{2Z} \left[(x - x')^2 + (y - y')^2\right]\right) dx' dy', \quad (2.10)$$

$$\text{where } \mathfrak{S}(x', y') = E(x', y') \times p_f(x', y') T_f(x', y'). \quad (2.11)$$

Equation (2.11) has 3-terms:

(a) the Gaussian field distribution $E(x, y)$ that was expressed in (2.9),

$$\text{(b) the aperture function, } p_f(x', y') = \text{circ}(r/r_0) = \begin{cases} 1 \rightarrow \text{for } r < r_0 \\ 0 \rightarrow \text{otherwise} \end{cases}, \quad (2.12)$$

$$\text{(c) the lens transmission function, } T_f(x', y') = \exp\left(\frac{j(x^2 + y^2)k_0}{2f}\right). \quad (2.13)$$

After simple algebra, Equation (2.10) becomes

$$E(x, y, Z) = C \iint p_f(x', y') \exp\left[\frac{-jk_0}{2Z} (xx' + yy')\right] \exp\left[\frac{-jk_0}{2q_z} (x'^2 + y'^2)\right] dx' dy' \quad (2.14)$$

where

$$C = \frac{jk_0}{2\pi Z} \times \frac{q_0}{q_0 + \Delta z} \exp\left[\frac{-jk_0}{2Z}(x^2 + y^2)\right], \quad (2.15)$$

$$\text{and } \frac{1}{q_z} = \frac{1}{q_0 + \Delta z} + \frac{1}{Z} - \frac{1}{f}. \quad (2.16)$$

Equation (2.6.5) can be solved numerically to provide the diffraction pattern at a distance Z from the lens under test. Such a diffraction pattern will be a function of the applied voltage and the lens aperture, since the lens focal length varies with the applied voltage.

The diffracted light intensity is $I(x, y, Z) \propto |E(x, y, Z)|^2$.

2.6.2 The Z-Scan Method

The Z-scan technique [107], originally developed in 1989 is a simple single beam method for characterizing the third order response of a non-linear optical material. Z-scan offers information on the sign and magnitude of the non-linear refractive index both simplicity and sensitivity. As shown in Figure 2.2, scanning the lens under test f for a distance $\pm \Delta z$ while monitoring the on-axis intensity for a set of fixed voltages, one can plot a family of curves. These set of curves for various voltages, i.e. various focal lengths, have a slopes at $\Delta z = 0$ that are proportional to the induced focal lengths. This means that for the Z-scan method we need to evaluate the integration in Equation (2.14) on-axis only. The value of the above integral on-axis is

$$E(0,0,Z) = \frac{-jk_0}{2\pi Z f} \left(\frac{q_0}{q_0 + \Delta z} \right) q_z \left[\exp\left(\frac{-jk_0 r_0^2}{2q_z} \right) - 1 \right]. \quad (2.17)$$

The complex conjugate of the above equation is

$$E^*(0,0,Z) = \frac{jk_0}{2\pi Z f} \left(\frac{q_0^*}{q_0^* + \Delta z} \right) q_z^* \left[\exp\left(\frac{jk_0 r_0^2}{2q_z^*} \right) - 1 \right]. \quad (2.18)$$

Therefore, the on-axis intensity is

$$I(0,0,Z) \propto E(0,0,Z)E^*(0,0,Z) \quad (2.19)$$

$$I(0,0,Z) = \Re_z \left[1 + \exp\left(\frac{jk_0 r_0^2}{2q_z^*} - \frac{jk_0 r_0^2}{2q_z}\right) - \exp\left(\frac{jk_0 r_0^2}{2q_z^*}\right) - \exp\left(\frac{jk_0 r_0^2}{2q_z}\right) \right], \quad (2.20)$$

$$\text{where, } \Re_z = \frac{k_0^2}{4\pi^2 Z^2 f^2} \frac{|q_0|^2}{|q_0|^2 + (\Delta z)^2} |q_z|^2. \quad (2.21)$$

After some algebraic manipulation we have

$$I(0,0,Z) = \Re_z \left\{ 1 + \exp\left(\frac{-k_0 r_0^2 b}{|q_z|^2}\right) - 2 \exp\left(\frac{-k_0 r_0^2 b}{2|q_z|^2}\right) \cos\left(\frac{k_0 r_0^2 a}{2|q_z|^2}\right) \right\}, \quad (2.22)$$

$$\text{where } a = \text{Re}al(q_z), \quad \text{and} \quad b = \text{Im}g(q_z). \quad (2.23)$$

The first set of simulated data was obtained for a probing beam of size 50 μm . At this beam size, the confocal parameter q_0 of the probing beam is $\approx 12.5\text{mm}$ at HeNe laser wave length $\lambda = 0.633\mu\text{m}$. The 3-D representation of the normalized on-axis detected irradiance, detected 1 m away, as a function of the scanning distance Δz for both positive and negative focal lengths, i.e. diverging and converging lenses are shown in Figure 2.3. In Figure 2.3a, lens diameter was set to 1000 μm so that it is much larger than the probing beam for the total scanning distance. It is worth noting that the normalized on-axis irradiance increases as the focal length increases for both cases of converging and diverging lenses. Furthermore, the normalized irradiance peaks lies on the positive and negative sides Δz for the converging and diverging lenses respectively. This a unique distinction between our linear Z-scan and the non-linear Z-scan initially developed by Sheik-bahae et al [107].

In Figure 2.3b, we assume a lens aperture of 250 μm such that the probing beam is comparable to the lens aperture and the end of the scanning distance. Hence, the on-axis

Fresnel intensity is expected to show the diffraction effects from the lens edges. Notice the intensity oscillation occurs towards the scanning distance end.

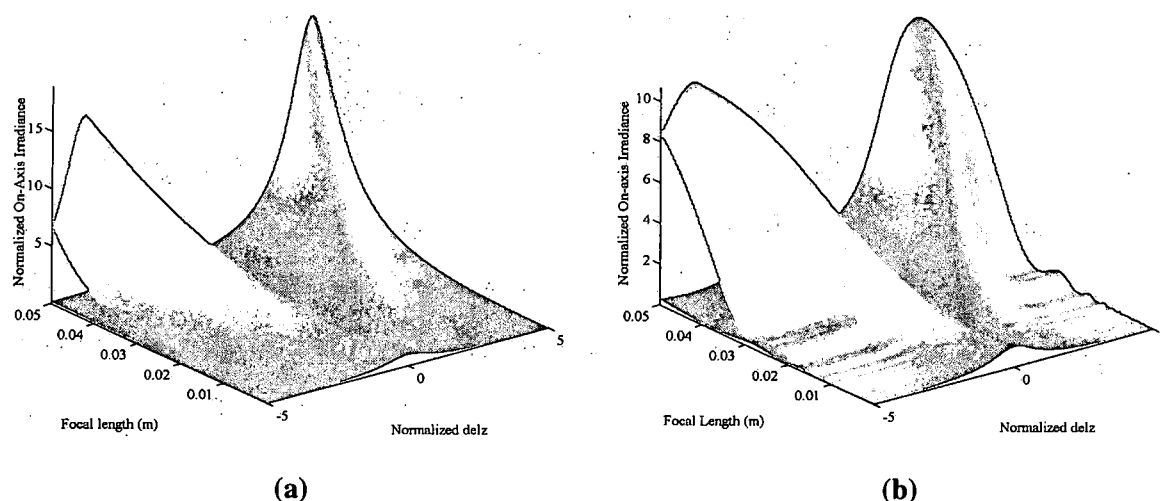


Figure 2.3 3-D representation of the on-axis Z-scanned Intensity for positive and negative lenses (a) without diffraction effects, and (b) with diffraction effects.

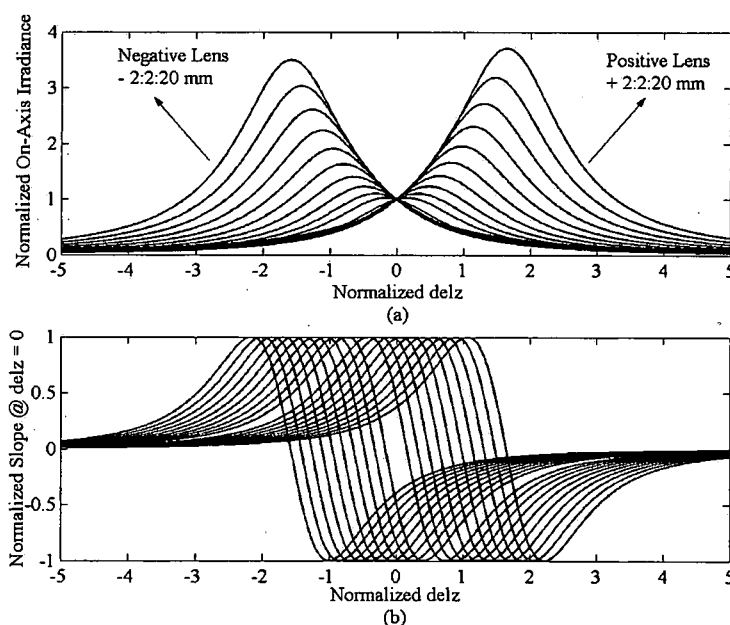


Figure 2.4 A 2-D representation of the z-scan shown in Figure 2.3a; (a) the normalized irradiance variation along the scanning distance; (b) the normalized slope at $\Delta z = 0$

In Figure 2.4a, a simplified cross-section of Figure 2.3a is shown for focal length variation of ± 2 -20 mm in increments of 2 mm. Figure 2.4b, is obtained by taking the slope at each point of the normalized irradiance plot of Figure 2.4a, and then normalizing

it with respect to the slope at $\Delta z = 0$. One may observe a similar behavior of Figure 2.4b with the original non-linear z-scan; however note that Figure 2.4b is drawn with the slope as the vertical axis. Figure 2.5 shows aperture diffraction effects on the z-scan. Notice that the variation of both normalized irradiance and slope in Figures 2.5a and 2.5b deviate from the smooth decrease of their values due to diffraction. In addition, peaks and minimas of Figure 2.5b are less than +1 and -1 for positive and negative longer focal lengths lenses respectively. Finally, one may observe that the normalized irradiance peaks' locations, w.r.t. the scanned distance, are closely packed to each other.

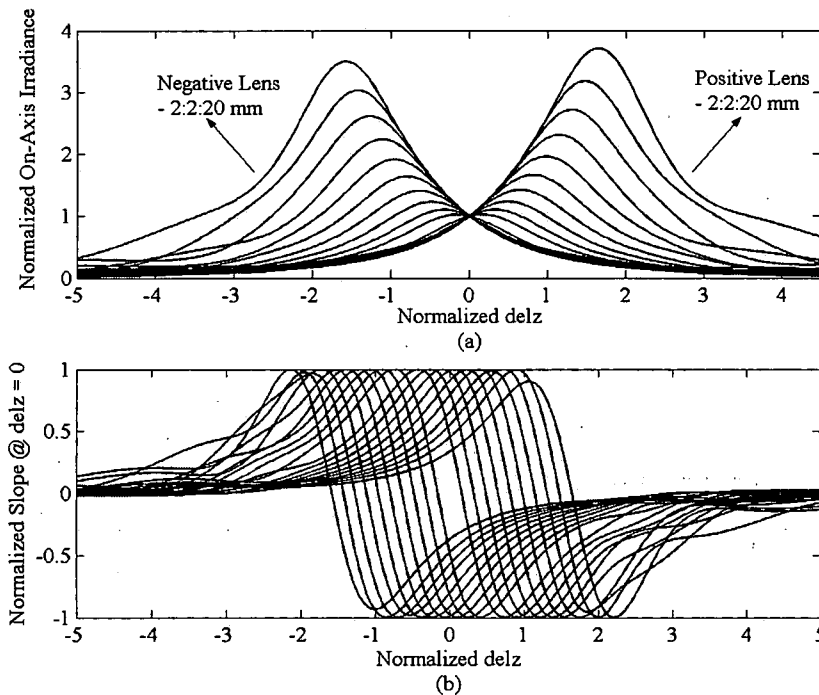


Figure 2.5 A 2-D representation of the z-scan shown in Figure 2.3b showing aperture size diffraction effects; (a) the normalized irradiance variation along the scanning distance; (b) the normalized slope at $\Delta z = 0$

A second set of simulated results were obtained using a probing beam of $20\mu\text{m}$. The confocal parameter q_0 in this case is $\approx 2\text{mm}$. Figure 2.6 illustrate the 3-D z-scan similar to that of Figure 2.3, with 2.6a without aperture diffraction effects, and 2.6b including diffraction effects. Note the reduction of diffraction effects comparing Figures 2.3b, and

2.6b. Furthermore, cases without diffraction effects shown in Figure 2.3a, is almost identical to that of case in Figure 2.6a.

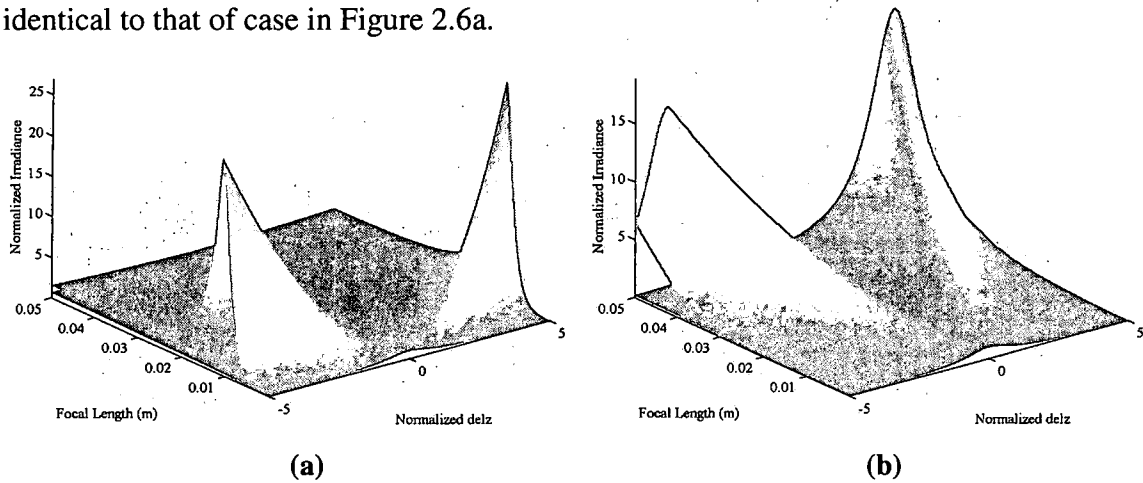


Figure 2.6 3-D representations of the z-scan using $20\mu m$ probing beam; (a) without aperture diffraction effects; (b) including diffraction effects.

A cross-section of Figure 2.6a is shown in Figure 2.7a, while Figure 2.7b is similar to Figure 2.4b. Comparing both figures, we observe that normalized irradiance peaks are more spaced out from each other. This is expected due to the fact that the confocal parameter in the latter case is smaller. Furthermore, such peaks are located approximately at a distance from the focal point of the external lens, i.e. $\Delta z = 0$, equivalent to the focal length of the lens under test. This is also illustrated in Figure 2.7b, where the location of the normalized slope value of zero is shifted around $\Delta z = 0$ by a value almost equals to the focal length of the lens under test.

In Figure 2.8 we illustrate that peak is not exactly located at a distance equal to the focal point. Two factors are contributing to this. First, the confocal parameter is not exactly 2mm. Second, in our simulation program, the observation plane distance was fixed w.r.t. to the external lens focal point.

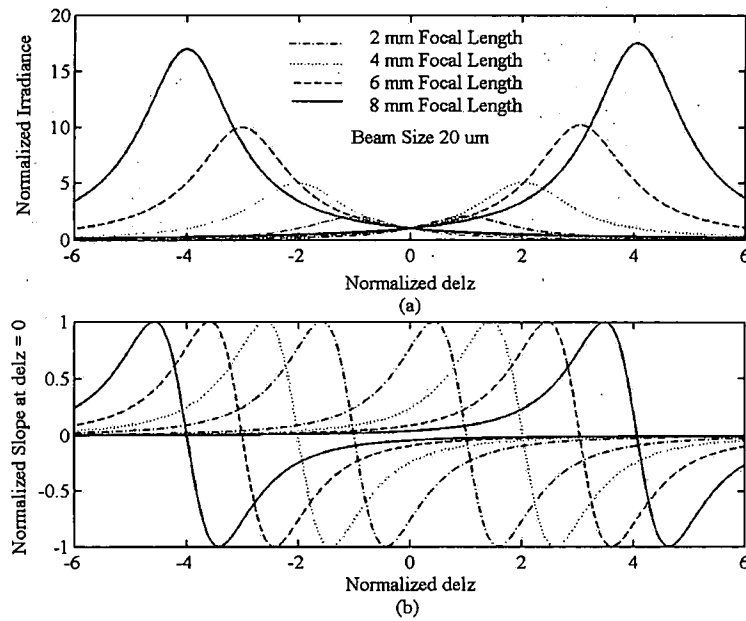


Figure 2.7 A 2-D representation of the z-scan shown in Figure 2.6a for probing beam of $20\mu m$ size; (a) the normalized irradiance variation along the scanning distance; (b) the normalized slope at $\Delta z = 0$.

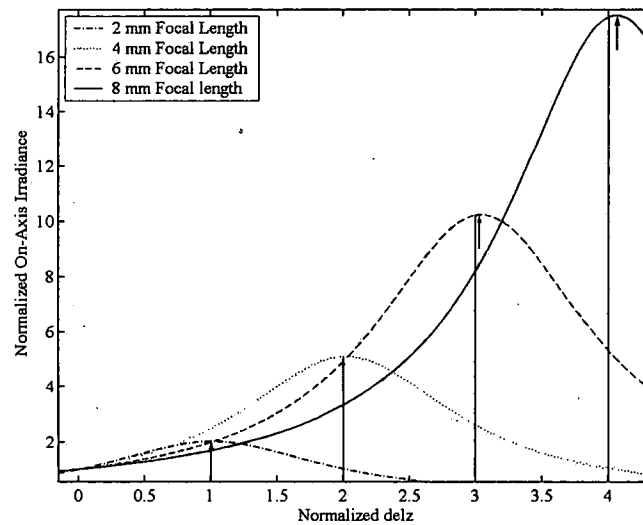


Figure 2.8 Irradiance peaks are slightly to the right of the focal length locations. The shift gets larger as the focal length gets longer.

These facts may contribute to an about 1% error in the focal length value. This error will almost double with doubling the focal length. By setting the observation plane at almost infinity and subtracting Δz from the observation distance one may cut such errors by one order of magnitude. Figure 2.9 illustrate such improvements. For an 8 mm lens, we can

cut the error in focal length value from 1% to 0.1%. Although this is not a big factor, we demonstrate the versatile accuracy of this method.

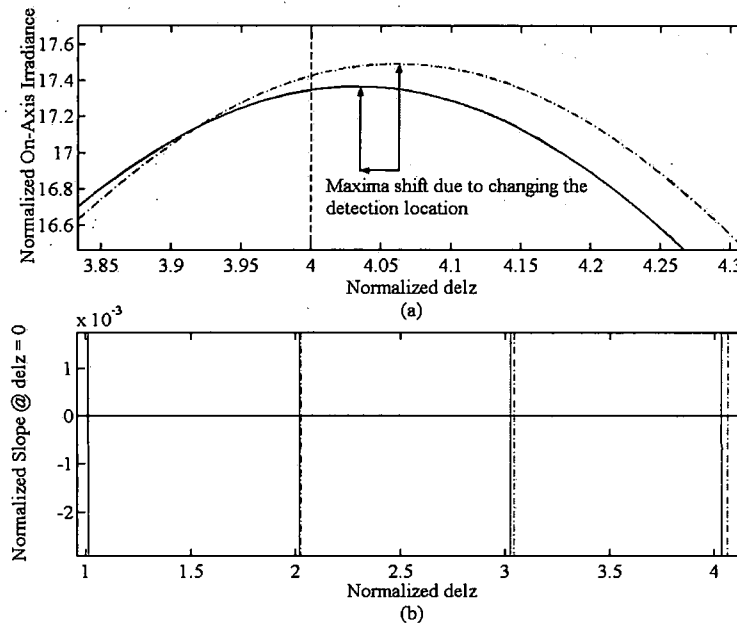


Figure 2.9 A close-up of the z-scan in Figure 2.7. By accounting for increasing the Z and subtracting Δz from Z , the observation distance, we shift the irradiance maxima location to exactly the focal point.

2.6.2.1 Aperture effects

For the sake of completeness we will look into the limitations on the z-scan method with respect to two issues. The first is the focal length determination certainty. Second, how long of a focal length can be determined.

We have three quantities that can be determined for the z-scan. First, the peak value of the normalized on-axis irradiance and its location with respect to the external lens focal point, i.e. $\Delta z = 0$. Second, the slope of the normalized irradiance at $\Delta z = 0$ accounts for the third quantity. A plot of the trace of the maximum on-axis irradiance as a function of the induced lens focal length is shown in Figure 2.10a. We have used lens aperture that is much larger than the probing beam. In addition, we have scanned for a longer distance such that we cover focal lengths up to 5 cm. Observe the quadratic increase of normalized

maxima, with higher value on the positive lens side than that of the negative lens side. Now, if we limit the scanning distance and also limit the lens aperture as indicated in Figure 2.10b, we start to see a clipping of the intensity peaks. This means that for specific aperture and probing beam sizes, one may have a limited range of lens focal lengths that can be determined directly from the graph looking only at the irradiance peak value. As a consequence the location of that peak will also depend on the scanning distance, i.e. limiting our ability to directly determine the focal length directly from the graph.

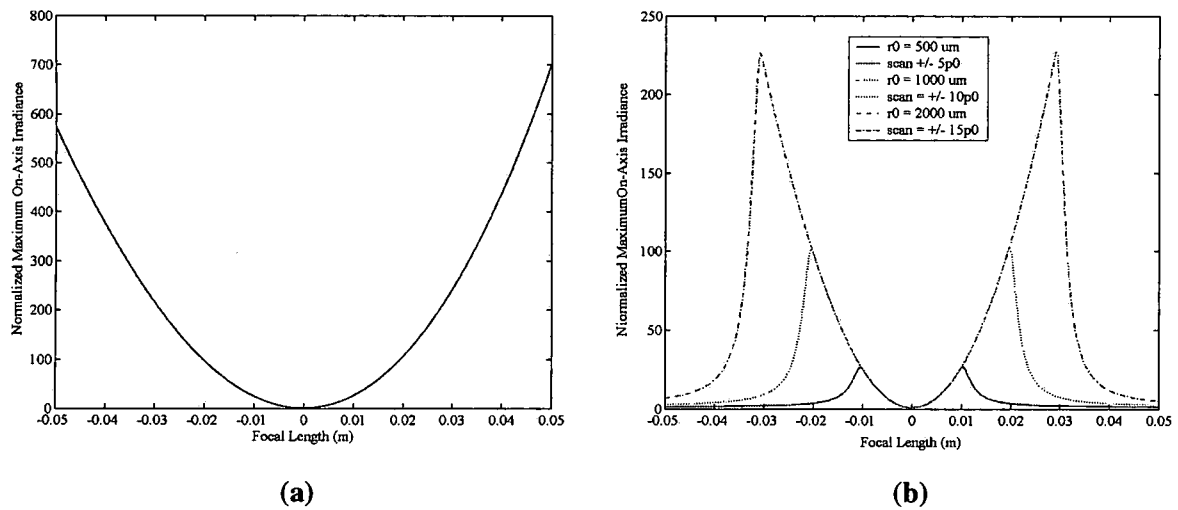


Figure 2.10 A trace of the normalized maximum on-axis irradiance values; (a) without any aperture diffraction effects; (b) with aperture diffraction effects. Note that the scanning distance increased with the increase of the aperture size.

The second item on the list is the slope of the irradiance curve at $\Delta z = 0$. This is indicated in Figure 2.11. We have plotted the normalized slope of the irradiance at $\Delta z = 0$ versus the induced focal length. We have used normalized irradiance raw data divided by the actual scanned distance in mm here, which is different from Figure 2.4b.

For a specific slope value, we have two focal length values. This will contribute to some uncertainty considering the focal length values range is unknown. Notice that the

smaller the probing beam, the higher and more closer the slope values are. This means that reducing the beam size will reduce the focal length range where uncertainty exists.

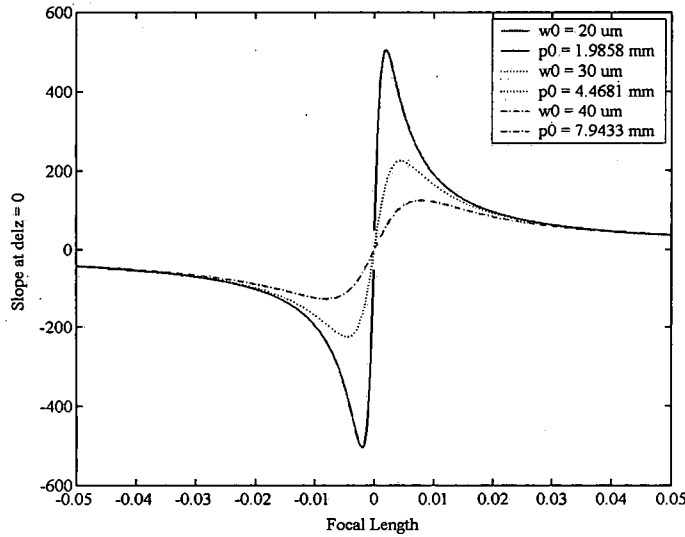


Figure 2.11 The effect of probing beam size on slope of the normalized on-axis irradiance as a function of the focal length. Note that $q_0 = p_0$.

In Figure 2.12, we assume that the lens under test is situated at a location $\mp \Delta z$ before and after the focal point of the external lens f_2 , referring to Figure 2.2, respectively. This $\Delta z = \mp 5q_0$, i.e. 5 times the Raleigh length, ensures that a probing beam of $50\mu\text{m}$ is approximately equal to the lens aperture ($250\mu\text{m}$). This configuration shows the onset of the diffraction effects as indicated in Figure 2.3b. The simulation indicates opposite behavior for positive and negative lenses. If we have a negative lens, the on-axis intensity starts with maximum value then decreases to a minimum, while the opposite is true of a positive lens.

This behavior oscillates as \cos^2 with diminishing amplitude. The opposite occurs for a positive lens where we start with a minimum and reaches maximum. If the lens under test is located after the focal point of f_2 , the maximas becomes minimas for both cases.

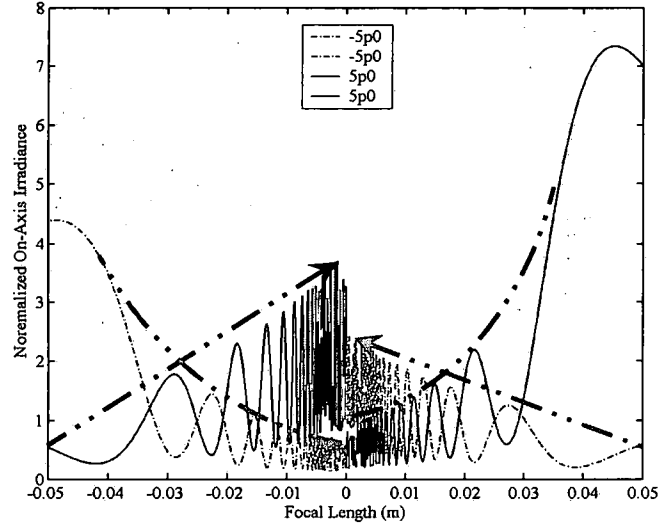


Figure 2.12 Simulated on-axis normalized irradiance as a function of the focal length of the lens under test placed at a fixed distance $\Delta z = \mp 5q_0 = \mp 5p_0$ while changing the applied voltage. Comparing to Figure 2.3b, it represents a cross-section at fixed Δz towards the end of the scanned distance.

Furthermore, we have traced the peaks of the oscillated irradiance. For a positive lens located before the external lens focal point, such peaks increase linearly with the decreased lens focal length. This behavior is shared also by the negative lens if it is located after the focal point of the external lens.

2.6.3 Fraunhofer Diffraction Approximation

It is difficult to solve the integral in Equation (2.14) in a closed form. However, it can be solved numerically. A first hand approximation to the foregoing discussion is the on-axis far field intensity obtained by Fraunhofer diffraction approximation [106]. The lens can be modeled by a circular pupil function of diameter r_0 .

$$p(x, y) = p(r) = \text{circ}(r / r_0), \quad (2.24)$$

multiplied by the phase curvature introduced by the lens of the form

$$\exp jk_0(x^2 + y^2) / 2f, \quad (2.25)$$

where f is the focal length of the lens. The far field pattern when the lens is illuminated by a uniform plane wave is proportional to the Fourier transform of

$$p(x, y) \exp jk_0(x^2 + y^2)/2f ,$$

and can be expressed as the convolution of the Fourier transforms of $p(x, y)$ and $\exp jk_0(x^2 + y^2)/2f$:

$$\begin{aligned} & \left(\frac{2\pi r_0}{\sqrt{k_x^2 + k_y^2}} J_1(r_0 \sqrt{k_x^2 + k_y^2}) \right) * \left(\frac{-j2\pi f}{k_0} \exp(j \frac{k_x^2 + k_y^2}{2k_0} f) \right) \\ & \propto \int_{-\infty}^{\infty} \int_{-\infty}^{\infty} \frac{r_0}{\sqrt{k_x'^2 + k_y'^2}} J_1(r_0 \sqrt{k_x'^2 + k_y'^2}) \bullet f \exp(j \frac{(k_x - k_x')^2 + (k_y - k_y')^2}{2k_0} f) dk_x' dk_y', \quad (2.26) \end{aligned}$$

where $J_1(x)$ is the Bessel function of the first kind. The on-axis optical far field (f, f) is given by setting $k_x = k_y = 0$:

$$E_{f,f}(r_0, f) \propto \int_{-\infty}^{\infty} \int_{-\infty}^{\infty} \frac{r_0}{\sqrt{k_x'^2 + k_y'^2}} J_1(r_0 \sqrt{k_x'^2 + k_y'^2}) \bullet f \exp(j \frac{(k_x'^2 + k_y'^2)}{2k_0} f) dk_x' dk_y'.$$

Changing to polar co-ordinates, this becomes

$$= \int_0^{2\pi} \int_0^{\infty} \frac{r_0 f}{k_r} J_1(r_0 k_r) \exp(j \frac{k_r^2}{2k_0} f) k_r dk_r d\theta, \quad (2.27)$$

$$\begin{aligned} & = 2\pi r_0 f \int_0^{\infty} J_1(r_0 k_r) \exp(j \frac{k_r^2}{2k_0} f) dk_r \\ & = 2\pi r_0 f \left(\int_0^{\infty} J_1(r_0 k_r) \cos(\frac{k_r^2}{2k_0} f) dk_r + j \int_0^{\infty} J_1(r_0 k_r) \sin(\frac{k_r^2}{2k_0} f) dk_r \right) \\ & = 2\pi f \left(\left\{ 1 - \cos(\frac{k_0 r_0^2}{2f}) \right\} + j \left\{ \sin(\frac{k_0 r_0^2}{2f}) \right\} \right). \quad (2.28) \end{aligned}$$

The far field on-axis intensity, after some algebra, becomes proportional to

$$I_{f.f.}(r_0, f) \propto 4f^2 \sin^2\left(\frac{k_0 r_0^2}{4f}\right). \quad (2.29)$$

Equation (2.29) is plotted in Figure 2.13, which indicates a behavior similar to the diffraction pattern as illustrated in Figure 2.12.

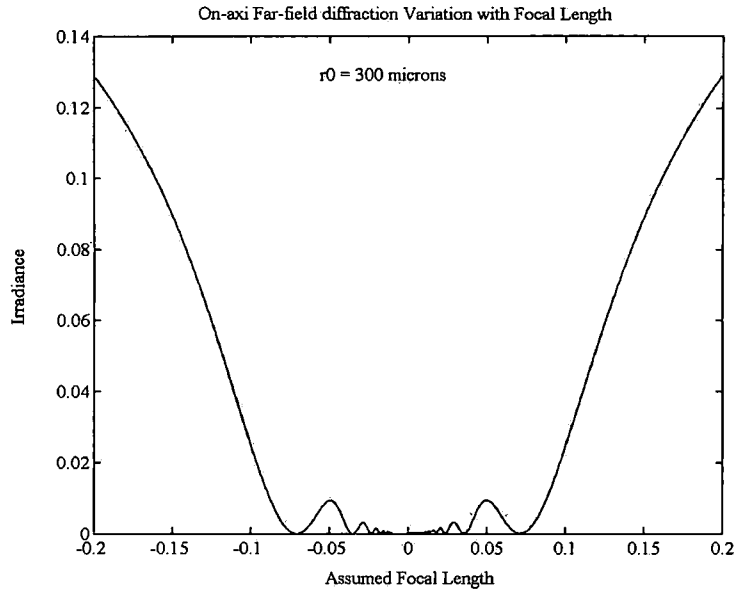


Figure 2.13 On-axis far-field intensity obtained by Fraunhofer diffraction approximation

2.6.4 Focal Length Obtained from Diffraction Size

In general, the far-field Intensity distribution of a lens with aperture r_0 is [108]

$$I(\theta, f) = I_0(f) [2J_1(r, f)/F(r, f)]^2, \quad (2.30)$$

where I_0 is the on axis intensity, θ is the diffraction angle, J_1 is the Bessel function of first kind and F is a function of r, f .

The formed diffraction pattern consists of a series of rings, but most of the light energy concentrates on the 0th-order ring called the Airy disc. The Airy disc size will vary with focal length, i.e. with the applied voltage. By measuring the disc size and knowing the power detected within one can determine the focal length of the lens. It has shown previously that the central disc of Airy pattern contains 83% of the total incident energy

at the image plane [109]. Furthermore, it has been shown that the electric field distribution at the focal (image) plane of a circular lens taking into account the lens aperture is [108]

$$E(\rho, f) \propto E_0 \frac{k_0 r_o}{j8f} \left[2 \frac{J_1(k_0 \rho r_o / 2f)}{k_0 \rho r_o / 2f} \right], \quad (2.31)$$

where ρ is measured in the xy-plane, and r_o is the lens aperture size. The intensity distribution is given by

$$I(\rho, f) \propto E_0^2 \frac{k_o^2 r^2}{64 f^2} \left[2 \frac{J_1(k_0 \rho r_o / 2f)}{k_0 \rho r_o / 2f} \right]^2. \quad (2.32)$$

The size of the focus S can be approximated by [108]

$$S = 1.22 \left(\frac{\lambda f}{r_o} \right). \quad (2.33)$$

Thus, by monitoring the inner lobe size, one can find the focal length of the lens.

2.7 The Geometrical Picture of the Z-scan

The following discussion provides the geometrical optics picture, using ray optics; to shed more light on the z-scan results achieved using the rigorous Fresnel diffraction formula. Furthermore, as we shall see by the end of this discussion, that both geometrical (ray optics), and physical (wave optics) pictures are in complete agreement.

Suppose that we have the above optical layout where the lens under test f_{ind} with a focal length f_i is located at a distance s in front of the focal point of an external positive lens f_{ext} . The focal length of that external lens is f . Moreover, one can write the ray coordinates at the exit face of the external lens in terms of the height x from the optical axis and the its angle or slope v that makes with the optical axis.

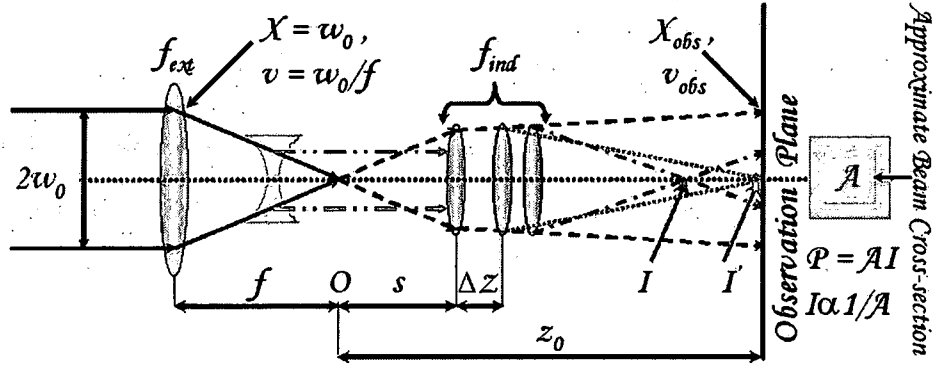


Figure 2.14 The experimental setup layout based on the geometrical (ray) optics explanation.

Similar coordinates at the observation plane of (x_{obs}, v_{obs}) indicated in Figure 2.14. This ray can be traced through the optical system, using the matrix method [106], where one can relate the input beam of width $2w_0$ to the output beam at the observation plane in terms of f, s, f_i , and z_0 . Since we are restricting ourselves to paraxial approximation in ray optics, the angle that the exit ray at the external lens make with the optical axis is small and can be expressed as w_0/f , thus the total optical system transfer function becomes

$$\begin{bmatrix} x_{obs} \\ v_{obs} \end{bmatrix} = \begin{bmatrix} 1 & z_0 - s \\ 0 & 1 \end{bmatrix} \begin{bmatrix} 1 & 0 \\ -1/f_i & 1 \end{bmatrix} \begin{bmatrix} 1 & f + s \\ 0 & 1 \end{bmatrix} \begin{bmatrix} -w_0 \\ w_0/f \end{bmatrix}, \quad (2.34)$$

$$= \begin{bmatrix} 1 & z_0 - s \\ 0 & 1 \end{bmatrix} \begin{bmatrix} 1 & 0 \\ -1/f_i & 1 \end{bmatrix} \begin{bmatrix} -w_0 + w_0 + sw_0/f \\ w_0/f \end{bmatrix}, \quad (2.35)$$

$$= \begin{bmatrix} 1 & z_0 - s \\ 0 & 1 \end{bmatrix} \begin{bmatrix} sw_0/f \\ w_0/f - sw_0/ff_i \end{bmatrix} = \begin{bmatrix} z_0 w_0/f - sw_0 z_0/ff_i + s^2 w_0/ff_i \\ w_0/f - sw_0/ff_i \end{bmatrix} \quad (2.36)$$

From Equation (2.36), we have

$$x_{obs} = \frac{w_0}{ff_i} [z_0 f_i - z_0 s + s^2], \quad (2.37a)$$

$$v_{obs} = \frac{w_0}{f} - s \frac{w_0}{ff_i}. \quad (2.37b)$$

For the sake of simplicity, assume that cross-sectional area of the optical beam at the observation plane is square with area A in shape with on-axis intensity I . Since the power is conserved and equal to

$$P = IA, \quad (2.38)$$

$$\text{hence, } I \propto 1/A, \quad (2.39)$$

$$\text{thus, approximately, the on axis intensity } I \propto 1/x_{obs}^2. \quad (2.40)$$

To characterize the on-axis intensity variation at the observation plane we take the derivative of Equation (2.40) with respect to s , and using Equation (2.37a) we get

$$\frac{dI}{ds} = -\frac{2}{x_{obs}^3} \frac{dx_{obs}}{ds} = -\frac{2}{x_{obs}^3} \frac{w_0}{ff_i} (2s - z_0). \quad (2.41)$$

Substituting Equation (2.37a) into (2.41),

$$\frac{dI}{ds} = \frac{(z_0 - 2s)f^2 f_i^2}{w_0^2 (z_0 f_i - z_0 s + s^2)^3}. \quad (2.42)$$

To find change of the on-axis intensity and its sign at the focal point of the external lens f we set $s = 0$ in Equation (2.42), hence

$$\left. \frac{dI}{ds} \right|_{s=0} = \frac{f^2}{w_0^2 z_0^2 f_i}. \quad (2.43)$$

Taking a closer look at Equation (2.43) clearly indicate that for induced lens $f_i > 0$ the change in the slope is positive, while for $f_i < 0$ the slope is negative. Furthermore, the change of the on-axis intensity is maximized, hence $I \rightarrow \infty$ if the denominator is equal to zero, hence

$$z_0 f_i - z_0 s + s^2 = 0. \quad (2.44)$$

By solving Equation (2.44), the location where the induced lens must be located to achieve maximum on axis intensity, thus

$$s = \frac{z_0 \pm z_0 \sqrt{1 - 4f_i / z_0}}{2}. \quad (2.45)$$

The positive part of the numerator will make $s > z_0$ which is non-physical solution, thus Equation (2.45) becomes

$$s = \frac{z_0 - \sqrt{1 - 4f_i / z_0}}{2}. \quad (2.46)$$

Since z_0 is large quantity, we can expand square root term, hence

$$s \cong \frac{z_0 - z_0(1 - 2f_i / z_0)}{2} \cong f_i. \quad (2.47)$$

The on-axis intensity as expressed in Equation (2.42) will be maximum when $s \approx f_i$. This result is in agreement with the previous result obtained from the rigorous analysis using diffraction theory. This concept is illustrated in Figure 2.15, where at a distance $s \cong f$, the geometrical (ray) optics predicts that the on axis intensity will be ∞ , while physical (wave) optics predicts a maximum. This makes sense since geometrical optics corresponds to the limiting case $\lambda \rightarrow 0$ [109]. This means that w_0 in Equation (2.42) is zero, i.e. Equation (2.42) reaches ∞ .

2.8 Effect of Applied Electric Field on Focal Length

It has been previously shown that the induced a refractive index distribution inside the PLZT wafer can for the two orthogonally polarized light components for the incident light due to the applied electric field can be expressed as

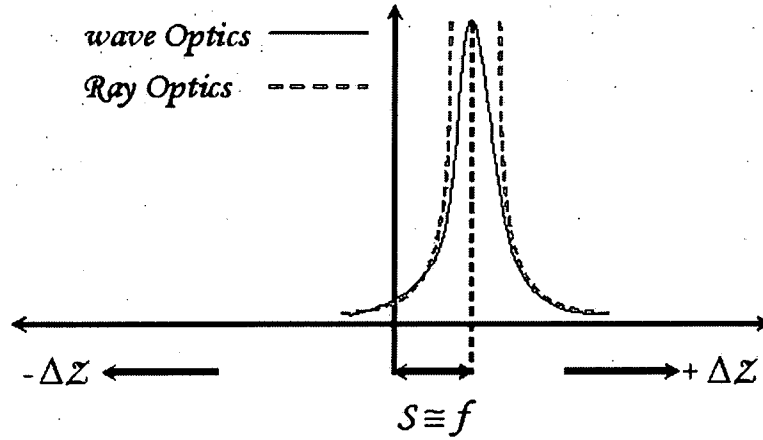


Figure 2.15 An illustration to the difference in the maximum on-axis intensity between the ray and wave optics.

$$n_1(r, z) = n_0 \left\{ 1 - \frac{n_0^2}{2} [r_{11} E_r^2(r, z) + r_{12} E_z^2(r, z)] \right\}, \quad (2.48)$$

$$n_2(r, z) = n_0 \left\{ 1 - \frac{n_0^2 r_{12}}{2} [E_r^2(r, z) + E_z^2(r, z)] \right\}. \quad (2.49)$$

By finding the electric field distribution within the PLZT, we can use Equations (2.48) and (2.49) to find the refractive index distribution. This technique will be utilized in conjunction with FEMLAB, to solve for the electrostatic distribution with the lens structure, and hence finding the refractive index distribution and phase. Since the optical field distribution behind the lens is

$$E(r, V) \propto \exp\left(\frac{jk_0 r^2}{2f}\right), \quad (2.50)$$

$$\text{where } \varphi = \frac{k_0 r^2}{2f} \text{ is the phase function of the lens.} \quad (2.51)$$

We can rewrite Equation (2.51) as

$$\phi(r, V_o) = \frac{k_0 r^2}{2f(V_o)}. \quad (2.52)$$

$$\text{Since } \delta\phi(V_o) = k_0 \delta n(V_o) L \text{ is the change in phase due to the applied voltage} \quad (2.53)$$

one can rewrite Equation (2.53) as

$$f(V) = \frac{r^2}{2\delta n(V_o) L}. \quad (2.54)$$

Note that the focal length decreases with increase δn .

Using Equation 2.57, Figure 2.16, shows the refractive index, and focal length variation as a function of the applied voltage. The simulated results in this figure were done for a lens with aperture size of 300 μm and substrate thickness of 300 μm .

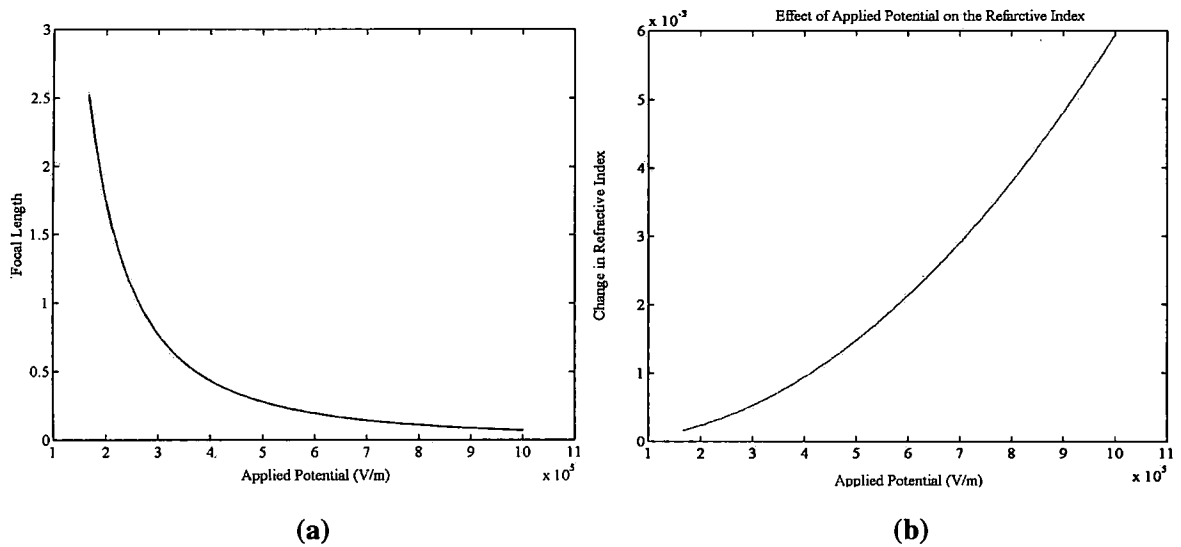


Figure 2.16 Simulated focal length (a), and refractive index (b) dependence on the applied voltage.

Chapter 3

Device Design, Fabrication, and Testing Setup

3.1 Summary

One of the key issues that affect any device realization process is its fabrication. The advantage of PLZT-based microlens arrays, described previously, is their simple design that lends itself to a simple fabrication process. In the following sections we will demonstrate a modular design that takes advantage of the integrated circuits IC die design usually implemented in the VLSI community where 1:1 step and repeat lithography process can be implemented. In addition, we will layout the experimental setup for testing the optical properties of the PLZT and microlens array.

3.2 Device Design and Layout

Using microfabrication technology, one can deposit an annular electrode array. The inner diameter of the electrodes represents the lenslet array apertures. The deposition process is being done on both sides of the PLZT wafer using backside alignment for perfectly aligning both electrodes in front and back of the wafer. Note that misalignment will result in an induced electrical field within the material that will cause the refractive index change not to follow a quadratic profile. Hence may cause higher order aberrations.

The fabrication process starts with designing the mask that is necessary to transfer the electrode pattern unto PLZT substrate. The layout of the mask has been generated using

AUTOCAD software. This mask will serve for transferring the electrode pattern, through lithography onto the substrate. The first set of designs has been done for 2" PLZT wafers.

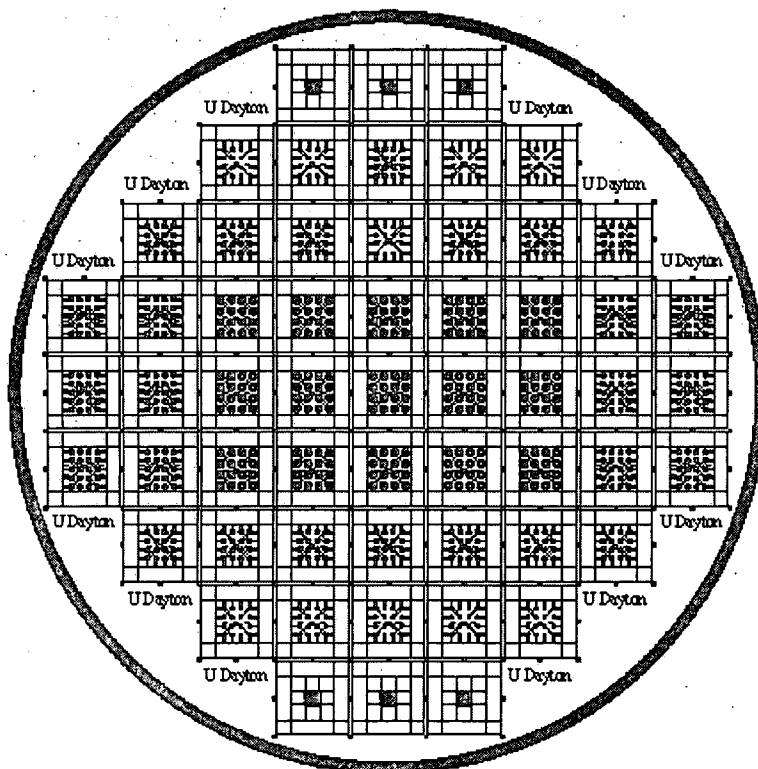


Figure 3.1 4" mask design layout generated by AUTOCAD. Note that each die area has a difference lens dimensions and various lenslet array packing density.

The first mask layout has three sets of patterns that serve for PLZT electro-optical characterization and two sets of lenslet arrays. The second-generation design, shown in Figure 3.1, is pursued on 4" wafers with thickness of 500 μm and 1000 μm respectively. In the 2 mask designs we have several sets of modular rectangular array, 57 in total, in a die like layout. Each rectangular area has a lenslet array. The inner and outer electrode diameters are unique for each area depending on the wafer thickness. The net electrode width will affect the induced electric field, i.e. refractive index profile. This shall be explained further in the simulation results in Chapter 4. In addition, it is noticeable that the lenslet packing density is different to further our abilities to study total diffraction

pattern by a set of lenslet array. Based on the initial calculation done in the previous chapter, we have chosen the inner electrode diameter to vary from 100 μm to 500 μm , with the outer electrode diameter to the inner electrode diameter ratio varying from 4:1 to 2:1 respectively. Sample dies are shown in Figure 3.2a,b. This modular design [68] allows for lenslet array variable structure for studying electrode design effects on focal length, lens phase profile, hence aberration issues. Furthermore, packaging each die separately will ease handling issues.

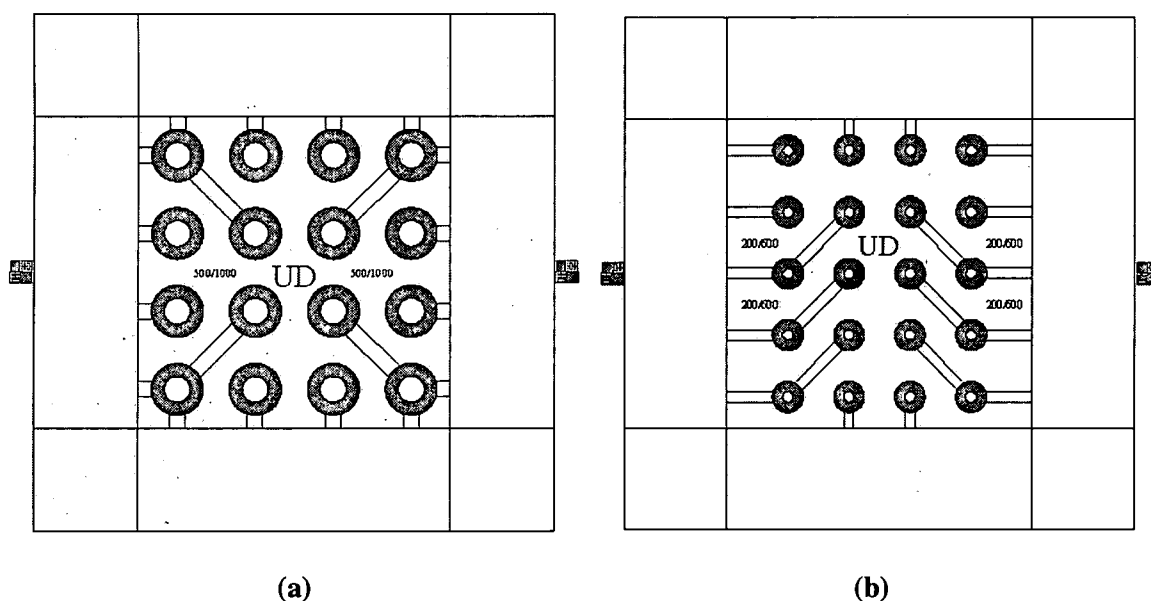


Figure 3.2 A Close-up for one set of dies from the mask illustrated in Figure 3.1; (a) a 500/1000 μm inner/outer electrode diameters; (b) 200/600 μm lens array.

3.3 Device Fabrication

The starting material is a polycrystalline PLZT substrate, of composition 9/65/36. The processing steps of the electrooptic module are shown in Figure 3.3. We start with a non-polished PLZT 2" wafer that was made using hot press techniques, of 750 μm thickness. Using blocking technique developed earlier [111], the wafer has been polished to an optically smooth surface on both sides of the wafer of thickness 280 μm to 350 μm .

Later, we have used 4" optically polished PLZT wafer. The objective of the process is to deposit the lens electrode structure according to our design. This electrode layer consists of 2 layers. The first is adhesion promotion layer, and we have chosen Indium Tin Oxide (ITO), as such layer. The second is Platinum (Pt). The reasons for choosing ITO/Pt as electrode materials will be discussed further in Chapter 7. The detailed fabrication process can be divided into the following steps

3.3.1 Wafer Cleaning

RCA [111] cleaning is a silicon standard cleaning process that consists of 3 steps. First, the wafer is degreased using Acetone, Methanol and DI water rinse for 5 minutes each. This is usually followed by base and acid cleaning steps, each lasting for 20 minutes. Since acids, particularly sulphuric acid, may attack PLZT, acid cleaning step is skipped. The composition of the base cleaning solution is ammonium hydroxide, hydrogen peroxide, and DI water with ratios of 1:1:5. This process is done for 15 minutes followed by DI rinse for 5 minutes. The wafer is then dried with N₂.

3.3.2 Lift-off Lithography

Prior to the lithography step, wafer should be heated to 120 °C for 20 minutes to drive off any moisture, and enhance photoresist adhesion. The photolithography process for lift off deposition can be summarized as follows:

- Spin-coat Shipley AZ 1818 @ 4000 rpm for 30 seconds
- Soft-bake for 20-30 minutes @ 90 °C
- UV exposure for 12 seconds @ 13 mW
- Soak the wafer in Chloro-benzene for 90 seconds
- Dry-off the wafers with dry N₂. Please, observe No Water Rinse

- Bake @ 90 °C for 4 minutes to dry off any excess Chloro-benzene
- Develop for 75 seconds in 4:1 positive developer, DI water
- Check if the photoresist was developed properly with residual left over. If not, develop longer
- Rinse the wafer in DI water for 5 minutes, then blow dry
- No hard-bake is necessary

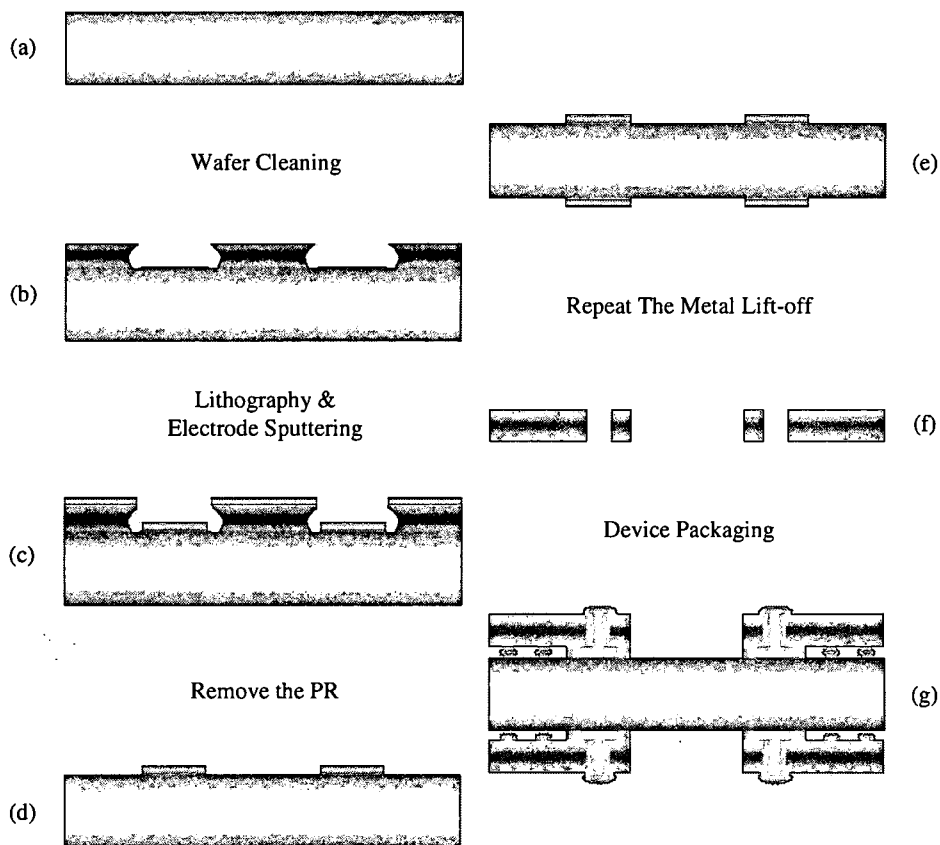


Figure 3.3 Fabrication steps of an electro-optic module: (a) PLZT wafer lapping and polishing to the desired thickness, (b) photolithography for electrode structure definition, (c) ITO/Pt deposition, (d) photoresist removal and ITO/Pt annealing, (e) repeating steps (b-d) on the other side of the wafer, (f) laser micromachining of the contact vias in a plastic wafer, and (g) bonding the top and bottom wafer to the plastic wafers and filling up the vias with conductive epoxy for the final PLZT module package

3.2.3 ITO/Pt deposition and Electrode Formation

Once the photolithography step is done, the wafer is ready for ITO/Pt deposition. The ITO is to be sputtered using 4" target at 200 Watts radio frequency (RF) signal, 5 mTorr chamber pressure, and for 30 minutes. The desired ITO thickness is 1500 Å. Afterwards, a 3000 Å Pt layer is sputtered as well.

Once the deposition is done, photoresist removal is done using a long soak in acetone. Afterwards the wafer is cleaned with methanol and rinsed with DI water. The final step in the electrode formation is annealing the ITO/Pt layer to promote adhesion and reduce the ITO layer sheet resistance. This process is to be done using rapid thermal annealing (RTA) at 450 °C for 1 minute. Now the device is ready for testing.

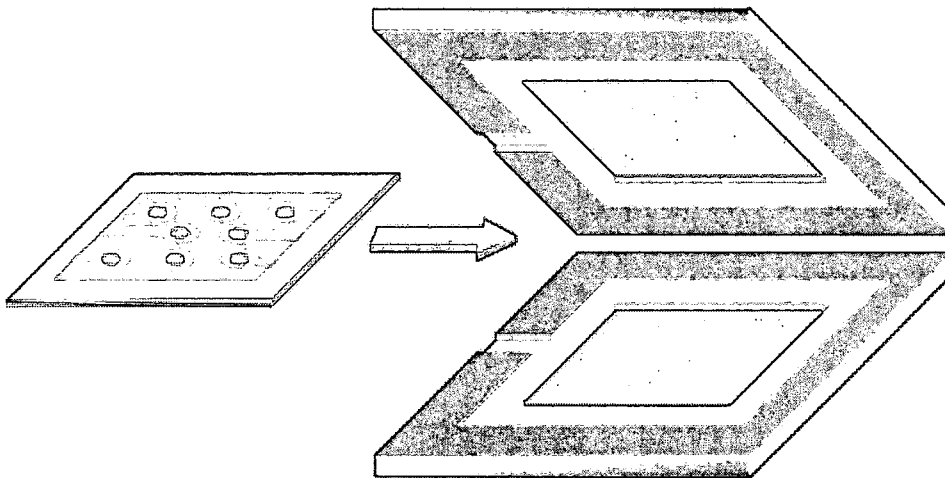


Figure 3.4 An illustration of the PLZT microlens array packaging module. The PLZT substrate is sandwiched between 2 plastic holders that have been formed using precision machining.

3.2.4 Device packaging

Once we realize the device structure, packaging is necessary. Plastic PMMA wafers of 1 mm thickness are to be used to package the PLZT to form an EO module. Using precision machining, or laser micromachining, the original mask information must be fed to the program controlling the machine. Then vias, with sizes larger than lenslet arrays

outer electrode diameters, must be etched precisely where the conducting contacts and other optical windows are needed, as shown in Figure 3.2f. The PLZT wafer will be sandwiched between the 2 plastic wafers and was aligned to the vias then boded to them with epoxy as shown in Figure 3.2g the vias will then be filled with conductive polymer and electrical contacts will made.

3.3 Electro-optic Properties Testing

Since its introduction, PLZT has been thoroughly investigated by many researchers. Different quadratic electrooptic coefficients values have been reported by various research groups. Most of such measured values have been obtained using transverse electrode structure[101] this configuration, the electric field direction is normal to the axial light direction. For PLZT composition of 8-9.5/65/35, this configuration is known as Slim Loop quadratic birefringence [72]. However, when the field is applied longitudinally in the direction of light propagation, scattering depolarization mode is obtained [112-114]. This effect produces depolarization of the incoming polarized light leading to an ON condition when the field is applied, and to an OFF condition when the field is removed [114]. Using ITO transparent electrodes allows this configuration to be utilized in spatial light modulator, displays and memories. It has been mentioned that this effect is not as strong as the birefringent effect, but it is still useful, especially in some polarization independent applications.

From the theoretical background in Chapter 2, it can be inferred that the quadratic electrooptic coefficient values will impact the focal length greatly. Also the sign of the ordinary and extraordinary EO coefficients will determine whether the lens is converging or diverging.

We have opted for measuring the EO coefficient for the PLZT wafers we use for two reasons. First, no enough data is available, to the best of our knowledge, for PLZT composition used in our experiments, in the longitudinal configuration [112]. We believe that the ring electrode structure of our device may be influenced by such configuration. Secondly, material imperfection can change the EO coefficients by factors that may affect our measurements.

The experimental setup for measuring the electro-optic coefficient and the light modulation effect is shown in Figure 3.5, [34]. Two ITO transparent electrodes are deposited on top and bottom of the PLZT substrate. A He-Ne laser, 632.8 nm of 5 mW, is used as the light source, with a beam size much smaller than the surface area of the electrode. The initial polarization state of the incident light was 45° with the transverse direction, i.e. the direction normal to the light propagation. The direction of the applied field is in the same direction as the incident light. This is a longitudinal field setup [112]. The analyzer (A) is required to convert the phase-modulated signal into amplitude-modulated [101]. A pinhole was used to filter out the scattered light [101].

From Equations (2.1), (2.2) we can determine the relative change in phase, and refractive index as a function of the applied electric field. Using curve fitting one can estimate the quadratic EO coefficient r_{eff} . By adding mirror stack to the front and the backside of the EO cell, we can realize a Fabry-Perot cavity, where the refractive index change due to the applied voltage will change the optical path length, hence tuning for various wavelengths and/or modulating the intensity of the output light.

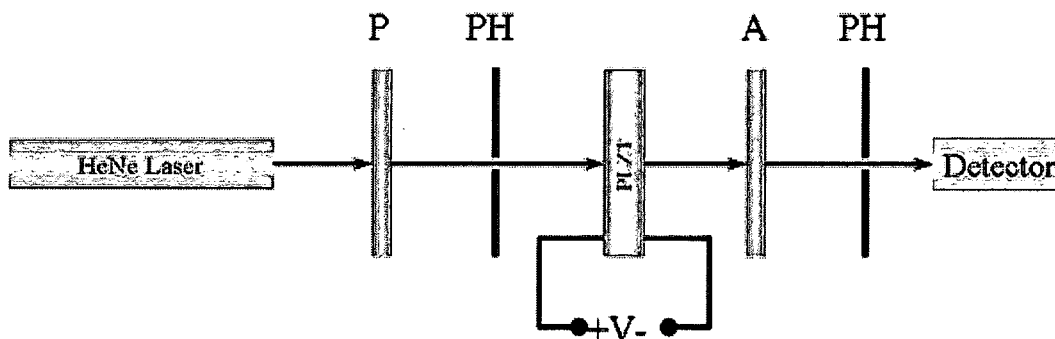


Figure 3.5 The experimental setup for the electro-optic coefficient and light modulator measurements.

3.4 Micro-lens Array Testing

The micro-lens array test setup is shown in Figure 3.6, a He-Ne laser beam is expanded with a 10x objective followed by a 500 mm and 2-100 mm 4-f system for light collimation and focusing. The uniform collimated light beam incident on the PLZT micro-lens array module is then imaged on a screen. The PLZT wafer used for this experiment is 280 μm thick. By varying applied voltage between 0 – 400 Volts, we can characterize the focal length of the lens using both Z-scan technique and the far-field diffraction pattern

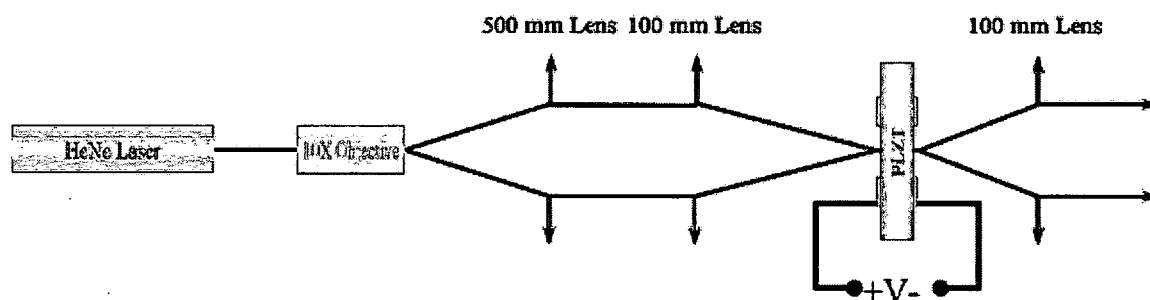


Figure 3.6 The experimental setup for the programmable micro-lens array measurements. This setup can be utilized for lens aberration studies as well.

Chapter 4

Simulation and Experimental Results

4.1 Summary

This chapter provides the reader with several preliminary simulation and experimental results. Since one of the main goals of this dissertation is to provide the basis for future work in adaptive beam shaping, the following sections will cover a broad spectrum of results.

First, the electro-optic properties results of PLZT will be introduced. Second, Finite Element (FE) based simulation for the induced electrostatic potential within the PLZT material is provided. Consequently, the refractive index profile, and phase profiles will be derived from these results. A comparison between the net phase changes obtained by a simple integration over the entire lens structure and of that obtained using simulation will be held. In addition, the results of the annular electrode widths influence on the phase change will be introduced. The third part will address the fabrication results and issues raised by our fabrication method will be addressed briefly. The fourth and final part will provide the preliminary results of the Z-scan method for finding the focal length of a single microlens. Finally, we will introduce fabrication results.

4.2 PLZT EO Properties

During any material's manufacturing process some artifacts may be introduced. Such artifacts and materials inconsistencies may results in changing material's properties. We have characterized the PLZT 9/65/35 substrates to ascertain their EO properties against published data.

We started such characterization process by measuring the refractive index as a function of the wavelength. The data generated by ellipsometry, is shown in Figure 4.1. The EO properties results are shown in Figure 4.2. The normalized output intensity as a function of the applied voltage, of the PLZT sample, after the analyzer (A) illustrated in Figure 3.4 setup is shown in Figure 4.2a.

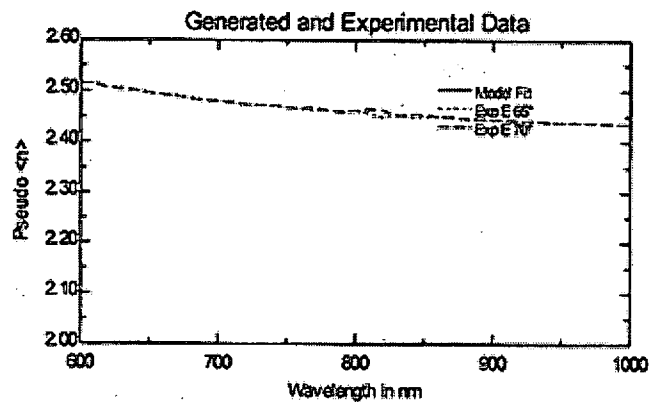


Figure 4.1 Refractive index variation as a function of the wavelength for a PLZT 9/65/35 substrate. These results were obtained using ellipsometry.

Using Equation (2.2), one can plot the phase variation due to the applied electric field as shown in Figure 4.2b. Utilizing Equation (2.2), that expresses the phase change relation of the light beam due to its passage through the PLZT EO sample, the refractive index variation as a function of the applied voltage is plotted in Figure 4.2c.

The refractive index variation can be close to 1% or about 0.02 of the original refractive index 2.52 at 0.6328 μm wavelength [68]. Using Equation 2.4 and a quadratic

fit shown in Figure 4.2d, we extrapolated that the quadratic EO coefficient is $7.69 \times 10^{-16} \text{ m}^2 / \text{V}^2$.

Based on the measured refractive index change, we calculated an approximate value for the focal length variation with the applied voltage using Equations (2.52), (2.54). The estimated focal length variation with applied electric field is shown in Figure 4.3. These values were calculated for $300 \mu\text{m}$ lens aperture and $280 \mu\text{m}$ thick PLZT substrate, without accounting for scattering and depolarization effects [101]. The estimated focal lengths will be compared later with the obtained z-scan results.

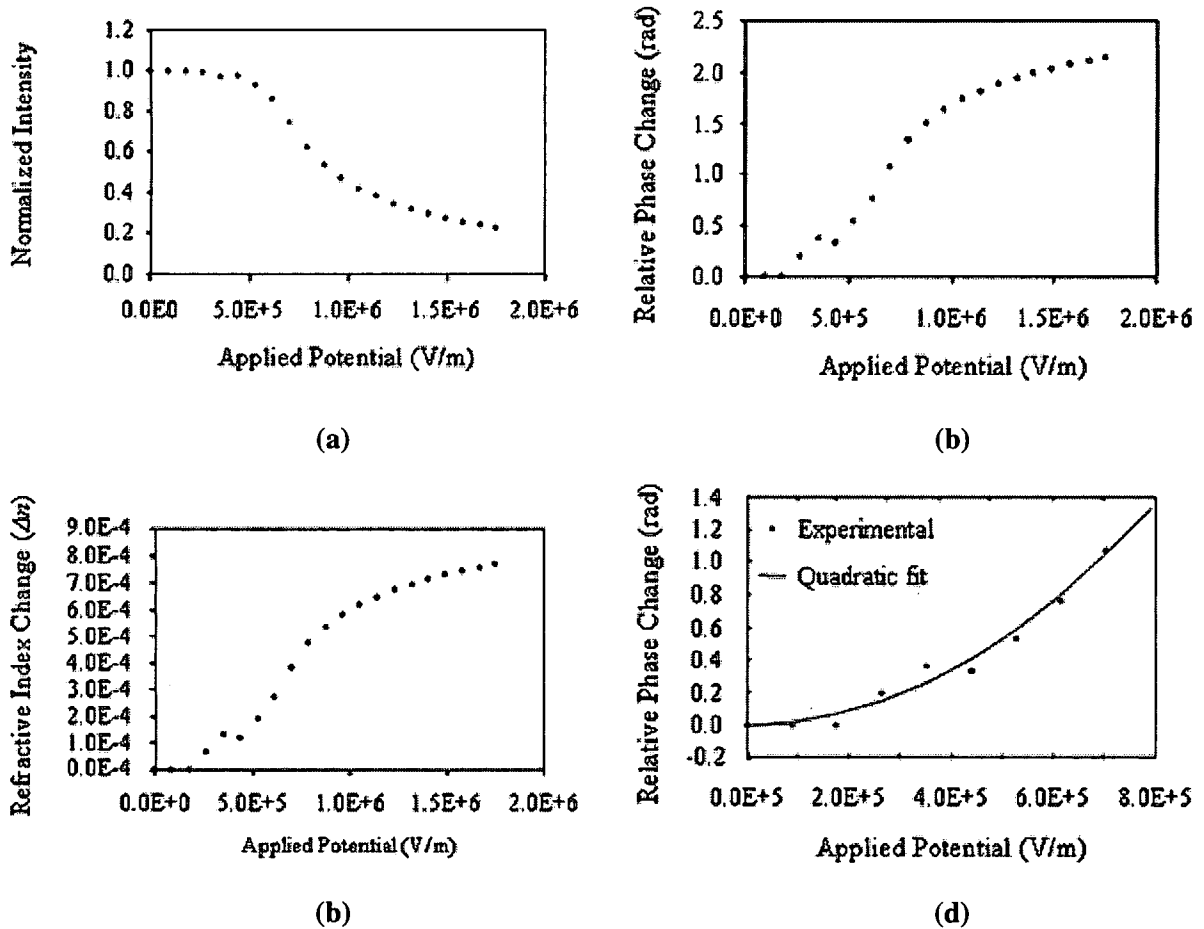


Figure 4.2 The EO measurement results, (a) the normalized intensity variation with applied electric field, (b) the phase variation induced due to applied electric field, (c) the relative change induced in the PLZT due to the applied electric field, and (d) the quadratic fit of the experimental results of the phase variation, where Equation 2.52 was used to extrapolate the quadratic EO coefficient.

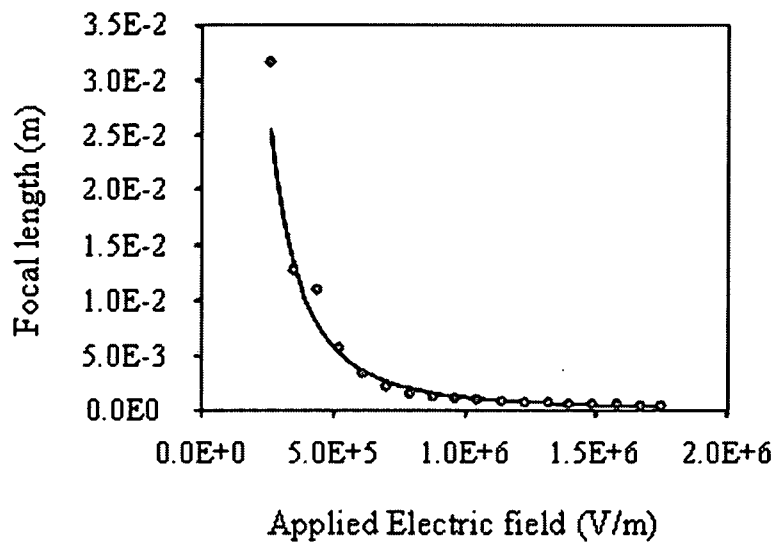


Figure 4.3 The estimated PLZT microlens focal length variation based on the EO coefficient determined experimentally by using Equation 2.54.

4.3 Finite Element Simulation Results

One of the most profound impacts that simulation tool packages has on the scientific community is the ability to model a complicated problem in a fast, efficient and accurate manner. Such tools allow for quick and precise estimate of crucial parameters of the problem at hand, hence saving substantial amount of funds that may have been wasted on the wrong prototype.

Previously, the electrostatic potential within the PLZT material, for the concentric electrode design, was found by solving Laplace's equation. This is not a trivial task, since we end up with a solution in the form of an integral equation that must be solved numerically [90]. This is a lengthy process, especially if we need to post-process the results, as suggested earlier in chapter 2 to obtain the far field diffraction pattern. Furthermore, extending the method to address a lenslet array will be difficult.

Finite Element method (FE) is powerful tool that has been implemented in many fields to model complicated physical problems [115]. As detailed elsewhere, [116], the

accuracy of solution depends on the mesh size. Smaller mesh sizes are needed for smaller structure to accurately account for the physical changes, while much larger structure can be handled nicely with coarser mesh size. This makes the FE method a very powerful tool for modeling our lens structure. To illustrate this point, we demonstrate in Figure 4.4a the cross-section of micro-lens slap with substrate thickness of $500\ \mu\text{m}$ and electrode thickness of $1\ \mu\text{m}$. The FE mesh was generated by FEMLABTM. Note the mesh density and element size variation around the electrode regions. The surface plot of the electrostatic potential due to 150 V applications is shown in Figure 4.4b.

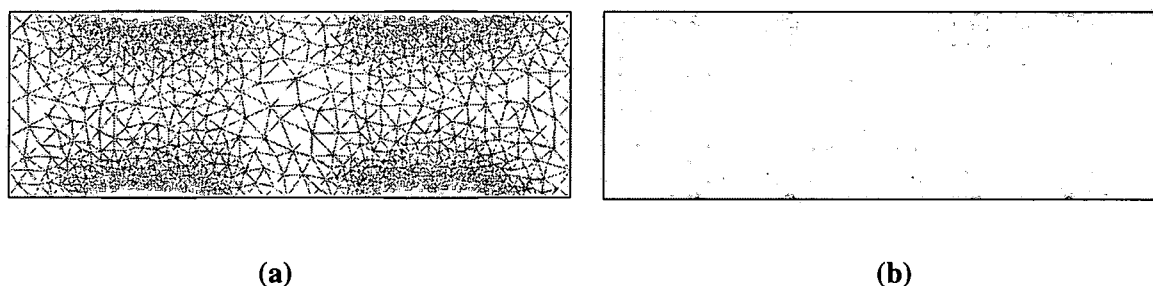


Figure 4.4 (a) The adaptive mesh generation using FEMLABTM, and (b) The surface plot of an induced electrostatic potential due to an applied voltage of 180 V.

FEMLABTM is a multi-physics software package where coupled thermal, mechanical, electrostatic effects, and chemical reactions, among other physical phenomenon, can be studied concurrently [115]. This will allow not only the phase change due to the applied electric field, but also for studying reliability issues as well. In addition, materials optical non-linearity, scattering and depolarization effects may be added for accurate modeling. Furthermore, it is seamlessly interfaced with MATLAB, which allows for easier data post-processing by using the data in other subroutines as we will show later.

4.3.1 Electrostatic Field Effects

The first item of simulation is to identify the domain within the microlens structure which the electrostatic potential distribution must be identified. Referring to Figure 2.1 and the description provided in [90], we have a circularly, i.e. axially, symmetric electrode design. This means that if we have a slice along the x - z plane as illustrated in Figure 4.4, we can revolve this cross-section around the z -axis we will obtain a cylinder where the lens aperture lays in middle, with inner and outer radii of r_1 , r_2 . Thus the horizontal axis for all plots is r while the vertical axis is z . All problems' dimensions are indicated in Figure 4.5. It is worth pointing out that we choose the lens aperture such that it matches the substrate thickness for generating the most quadratic phase profile, hence aberration free lens [90].

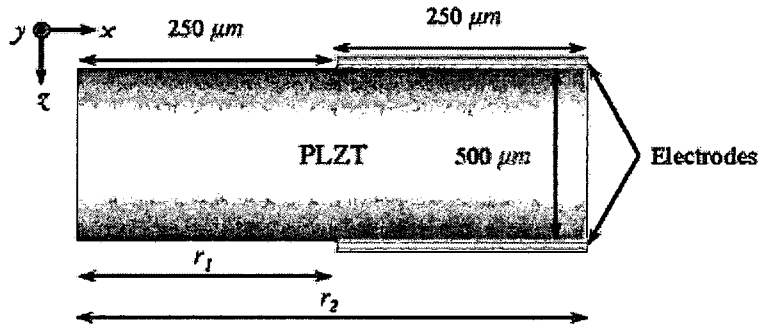


Figure 4.5 Cross-sectional slice of the PLZT microlens structure under test. Note that the cross-section is along the x - z direction and represents one-half of the lens structure. If we revolve this cross-section around the z -axis we will obtain a cylinder where the lens aperture lays in middle, with inner and outer radii of r_1 , r_2 .

Also, for the sake of convenience, we repeat above Equations (2.48), (2.49) for the refractive index change in the x - and y -polarization directions respectively. Finally, we set $R_{11} = 2.42 \times 10^{-16} \text{ m}^2 / \text{V}^2$ and $R_{12} = -1.94 \times 10^{-16} \text{ m}^2 / \text{V}^2$ [90], as the values for

electro-optic coefficients. One final note, we considered electrode thickness to be negligible.

$$n_1(r, z) = n_0 \left\{ 1 - \frac{n_0^2}{2} [r_{11} E_r^2(r, z) + r_{12} E_z^2(r, z)] \right\}, \quad (2.48)$$

$$n_2(r, z) = n_0 \left\{ 1 - \frac{n_0^2 r_{12}}{2} [E_r^2(r, z) + E_z^2(r, z)] \right\}. \quad (2.49)$$

In Figure 4.6a, b we have surface and contour plots for the induced electrostatic field components in the z - and r -directions respectively due to 300 V, i.e. 0.6 KV/m^2 , applications. The corresponding change in the refractive index Δn for the x - and y -polarization states are shown in Figures 4.8a, b respectively.

A closer examination of the radial change, i.e. w.r.t. r , of the electrostatic field, and the refractive index changes are shown in Figures 4.7, and 4.9. This corresponds to the x - y plane and was taken in $100 \mu\text{m}$ increments in the z -direction.

4.3.2 Focal Length Estimation

Figures 4.7 and 4.9 illustrate the change of refractive index, due to the electrostatic potential, in the radial direction, i.e. x - y plane, within the lenslet aperture at various z -levels perpendicular to the direction of light propagation. This means that we can divide the lens structure, in the z -direction, into subsections. Each subsection can be considered a slab of thin film that has the same refractive index profile. Now several approaches can be used to calculate the net phase delay, due to optical beam propagation through lens structure. First, we can integrate over the entire structure assuming an incident beam with plane wave fronts. Second, and more accurately, we can use the Beam Propagation Method (BPM) [117]. However, even for tightly focused beams, i.e. $20 - 40 \mu\text{m}$, the

Raleigh length will be larger than our samples thickness, which is $500\mu\text{m}$. Hence, the net phase delay can be approximately calculated as

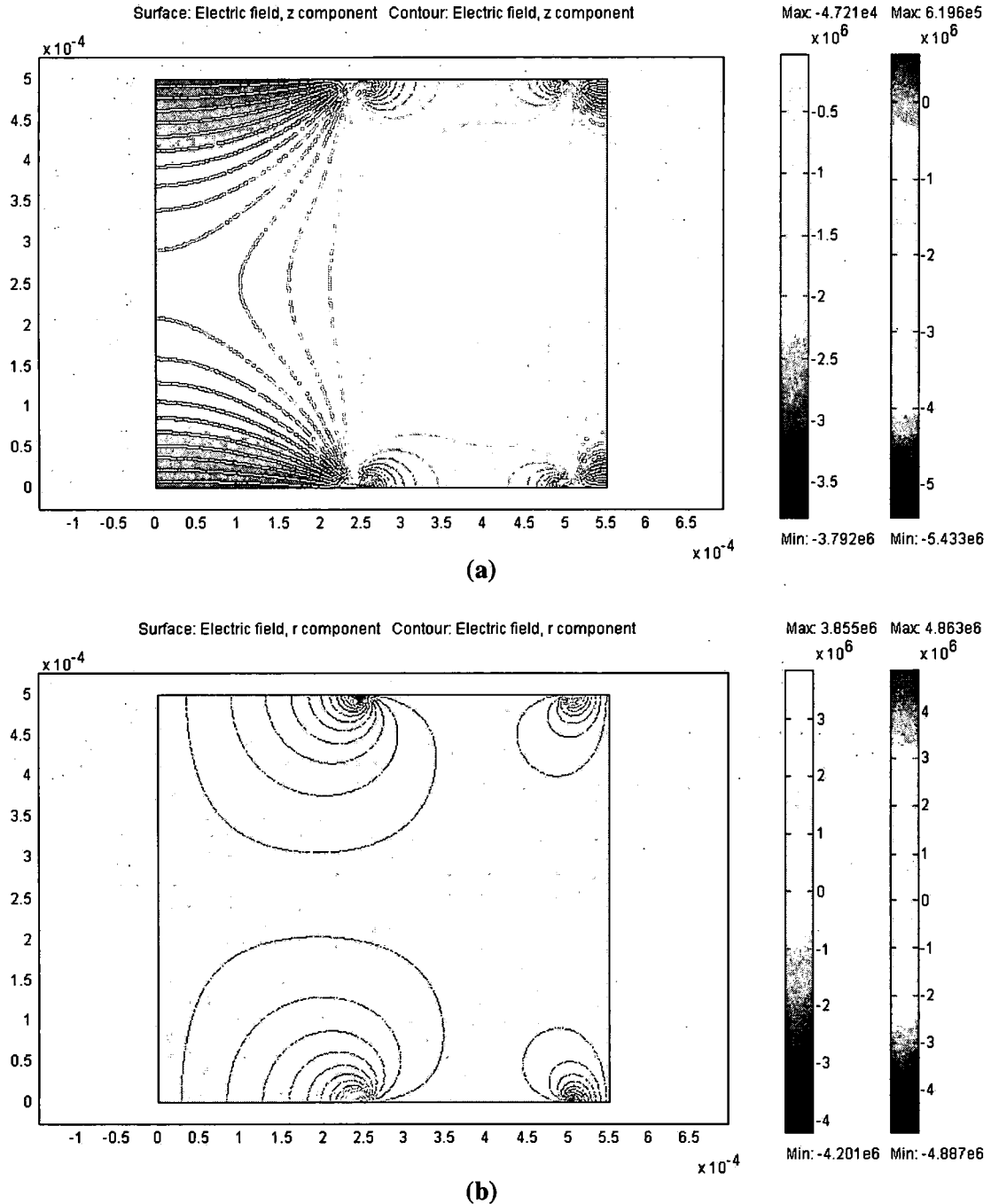


Figure 4.6 Surface and contour plots for the induced electrostatic field within the PLZT due to 300 V applications; (a) the z -component, and (b) the r -component. Note that the horizontal axis is r while z is the vertical axis.

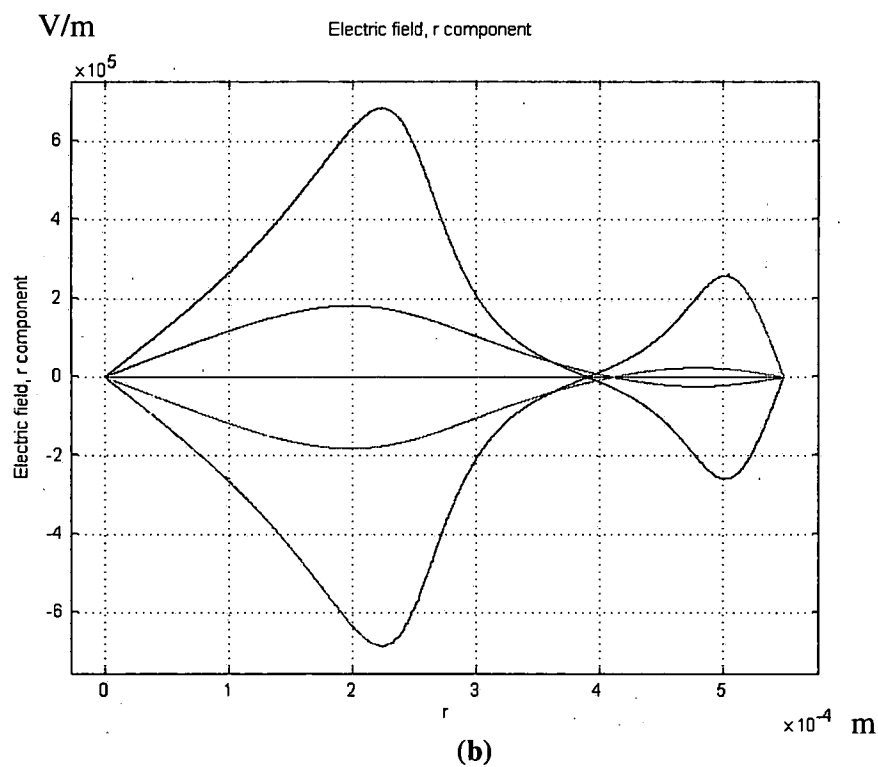
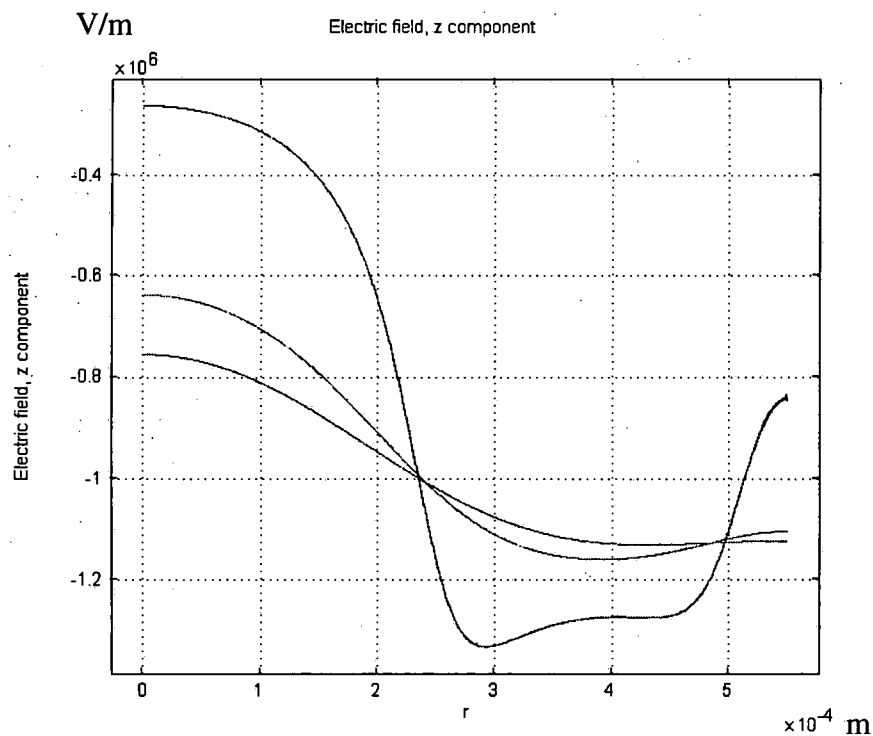


Figure 4.7 The radial change, i.e. x - y plane, of the electrostatic field components as a function of r ; (a) z -component, (b) r -component. These are 5-level cross-sections at $100\ \mu\text{m}$ intervals in the z -direction, hence the electric field variation at different heights of the PLZT substrate thickness.

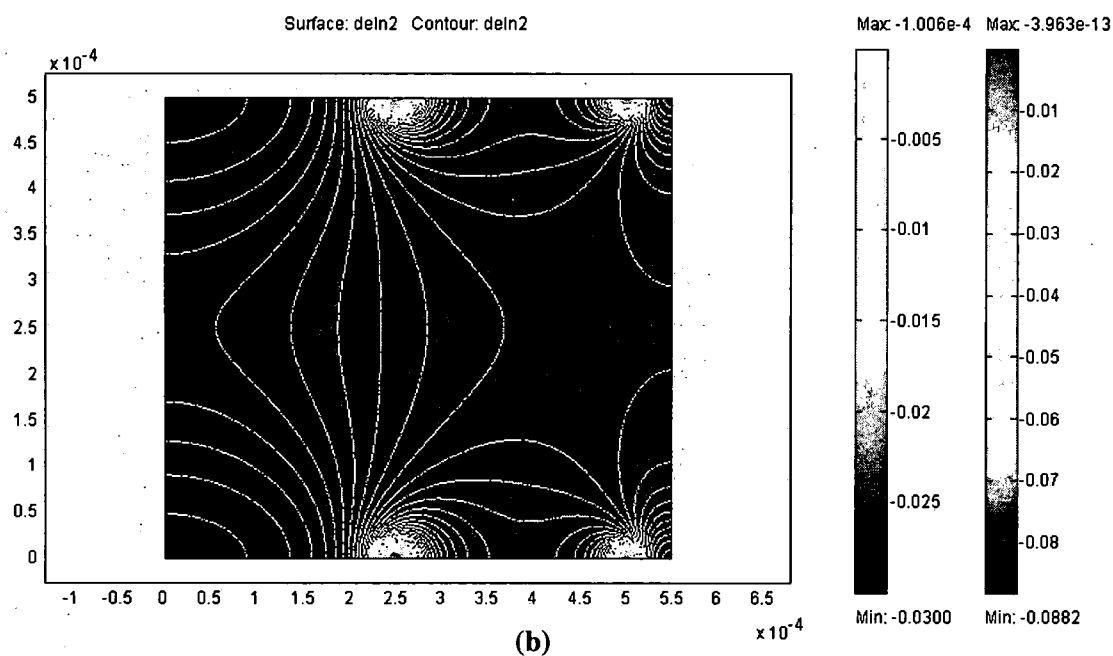
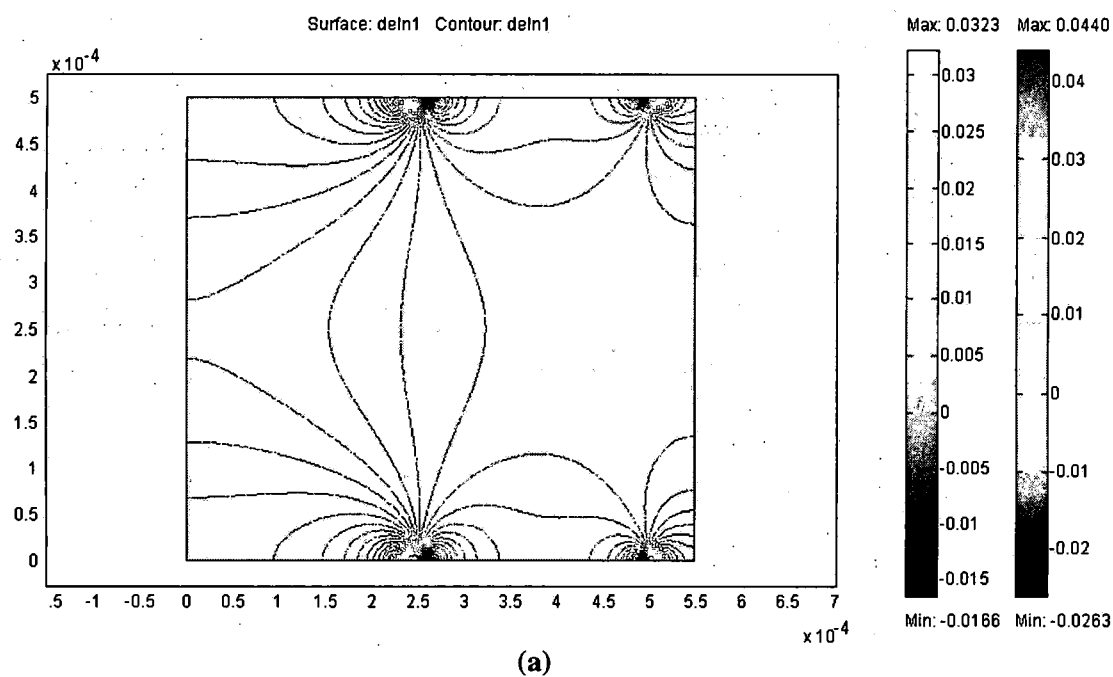
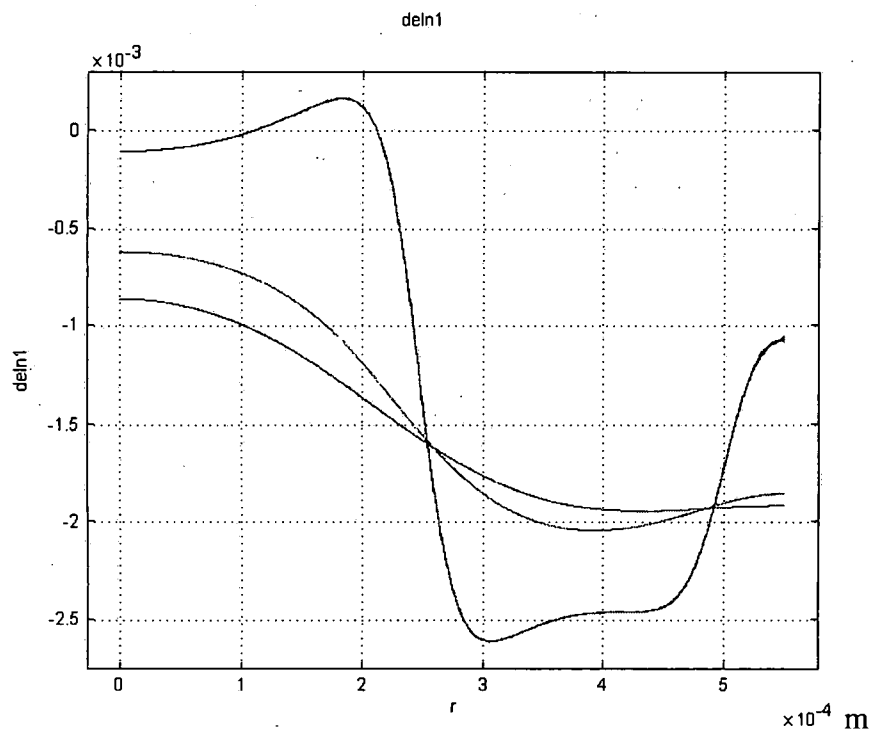
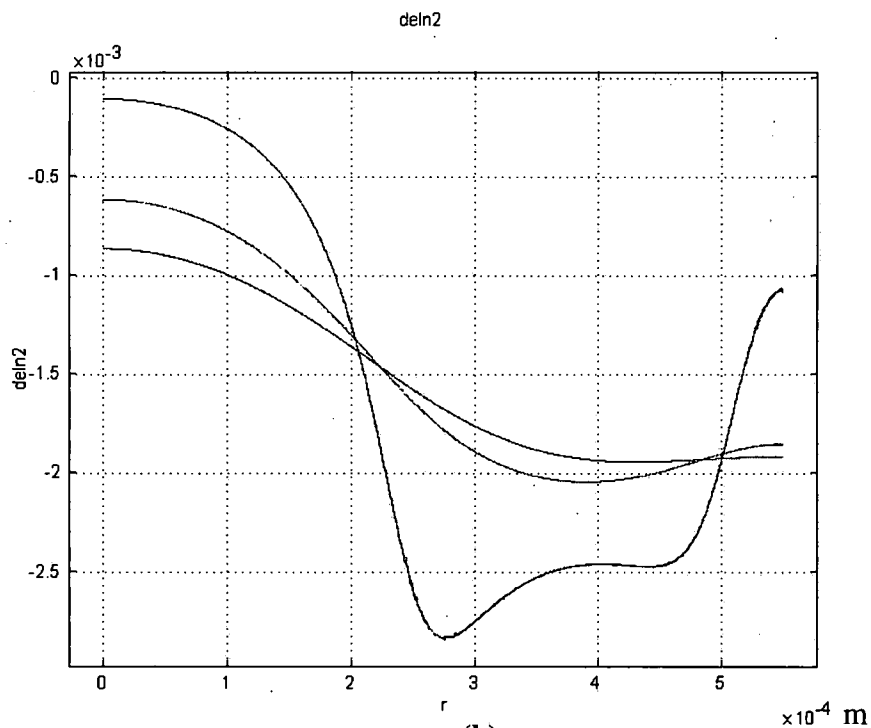


Figure 4.8 Utilizing Equation 2.48 one can obtain surface and contour plots for the Δn change within the PLZT material; (a) x-polarization, and (b) y-polarization.



(a)



(b)

Figure 4.9 The corresponding radial change of Δn at $100 \mu m$ intervals in the z -direction; (a) x -polarization, (b) y -polarization. Note the total resemblance with the z -components of the electrostatic potential.

$$\Delta\varphi = n_0 k_0 \sum_{i=1}^n \Delta z_i \Delta n_i, \quad (4.1)$$

where, $n_0 = 2.54$ is the refractive index of the PLZT at 0V, $k_0 \approx 10^7 \text{ m}^{-1}$ is the free space wave number, Δz is the layer thickness, and Δn is the refractive index profile within such layer. All calculation will be based on the use of HeNe laser @ 633nm. Since Δz will always be a fixed quantity, we can rewrite Equation 4.1 as follows

$$\Delta\varphi = n_0 k_0 \Delta z \sum_{i=1}^n \Delta n_i. \quad (4.2)$$

Since substrate thickness is $500\mu\text{m}$, $\Delta z = 5\mu\text{m}, 1\mu, 0.5\mu\text{m}$ for 100, 500, 1000 layers respectively. In our calculations we have found out that no matter how many layers were used in the calculation, the net phase change will always be the same. Therefore all of the following calculations were based on 500 layers.

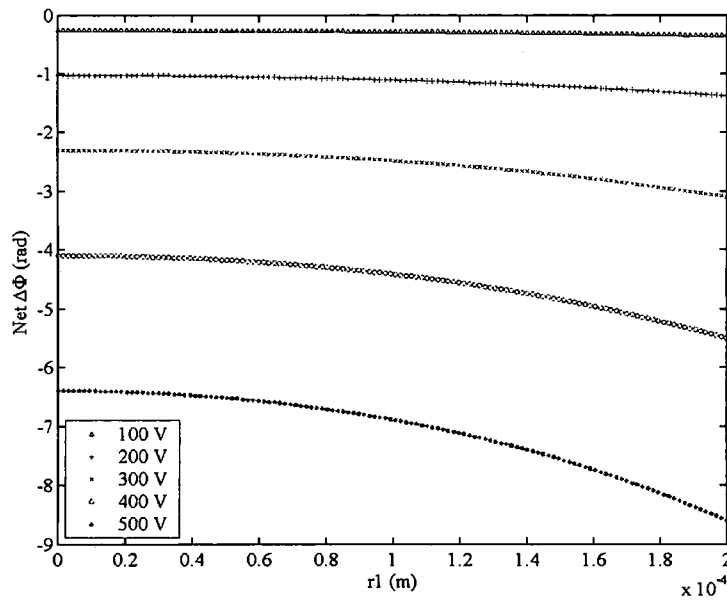


Figure 4.10 The net phase change due to various applied voltages. Note that we have a fill factor of 80%. Hence, we calculate the phase over 80% of the lens aperture. The plots are for $\frac{1}{2}$ of the lens aperture, since we have circularly symmetric lens design.

Once $\Delta\varphi$ is computed, based on Equation (4.2) as illustrated in Figure 4.10, we fit data point to a quadratic profile, assuming minimum induced lens aberration. It was shown previously that that minimum aberration can be achieved with lens aperture equal to the substrate thickness [90]. All simulation provided here is based on 1:1 ratio between the wafer thickness and lens aperture width. The equation for data fitting is in the form of

$$\Delta\varphi = ar^2 + br + c. \quad (4.3)$$

Since the optical field distribution immediately behind the lens is

$$E \propto \exp\left(\frac{jk_0 r^2}{2f}\right), \quad (2.53)$$

one can use the quadratic coefficient of Equation 4.3 and Equation 2.53 such that

$$\Delta\varphi = \frac{n_0 k_0 r^2}{2f} = ar^2, \quad (4.4)$$

hence,

$$f = \frac{k_0}{2an_0}. \quad (4.5)$$

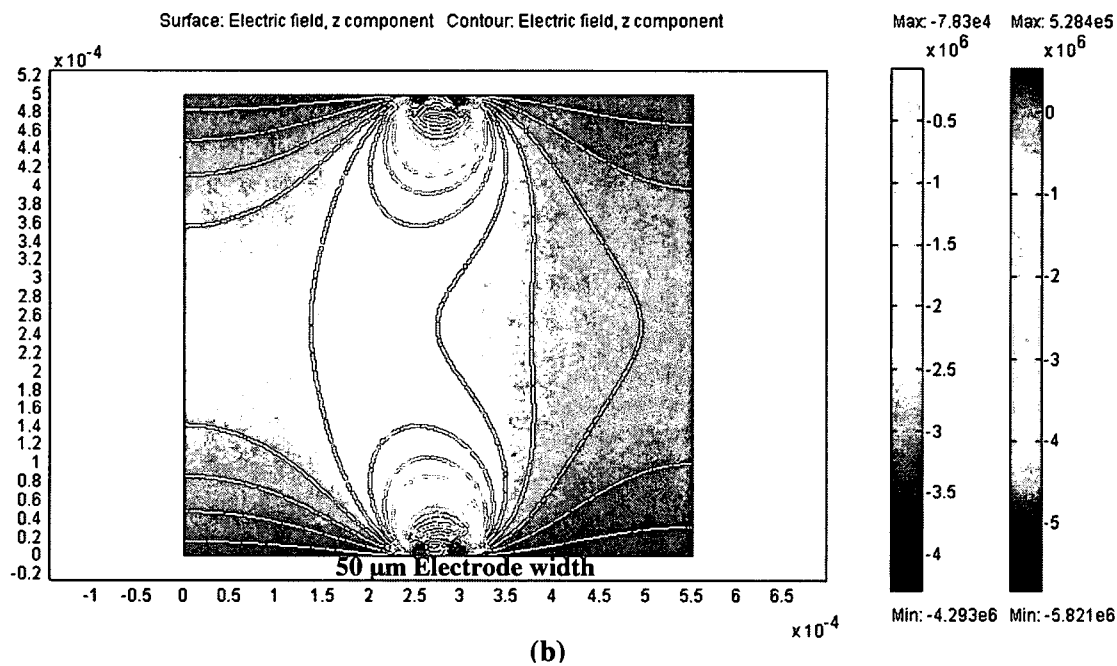
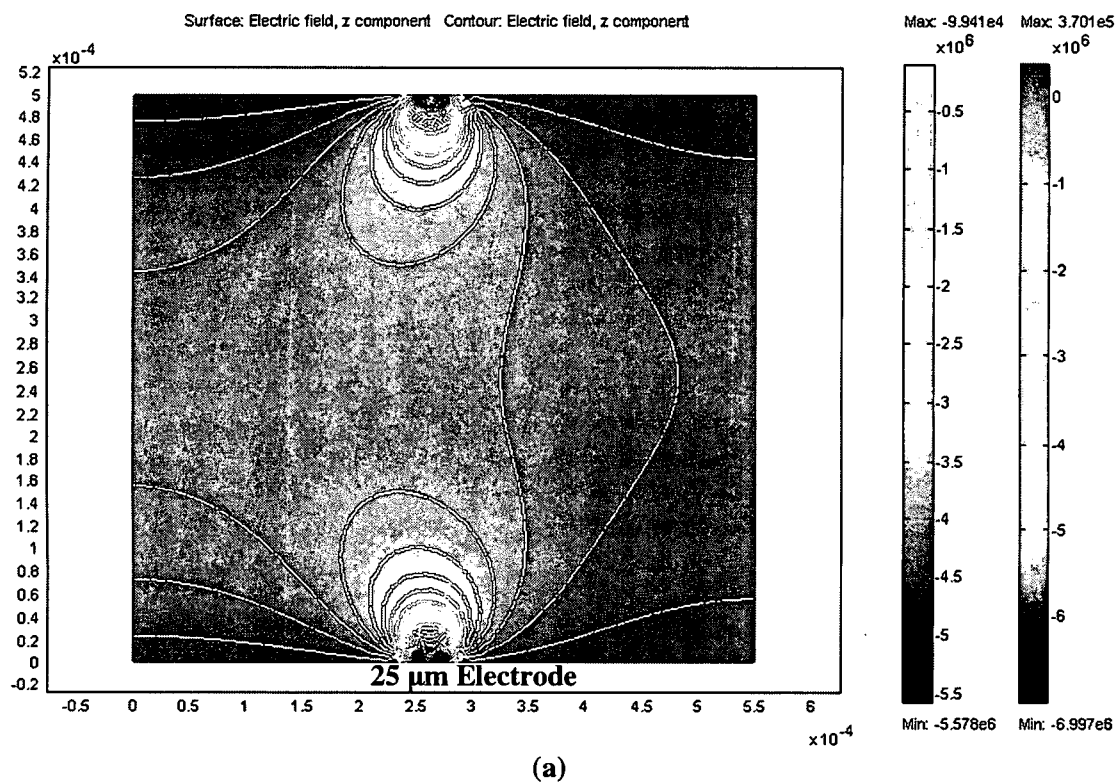
Table 4.1 shows the coefficient “ a ” obtained from fitting data in Figure 4.10 for various applied voltages. From the data in table 4.1 one finds that the coefficients a, b have negative signs, hence the FEMLAB simulation predicts that we will obtain an induced diverging lens with the shortest possible focal length of 3.27 cm. This will occur for a lens with electrode diameter, i.e. lens aperture of $500\mu m$. All the results here are for the x -polarized light.

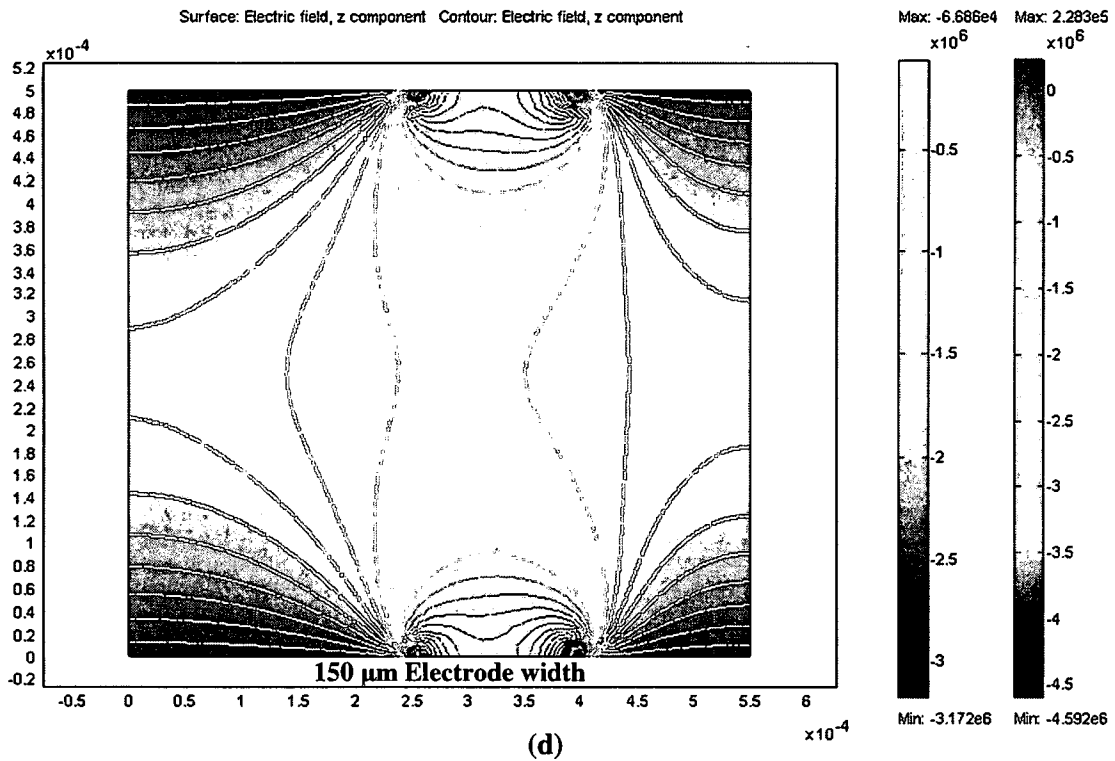
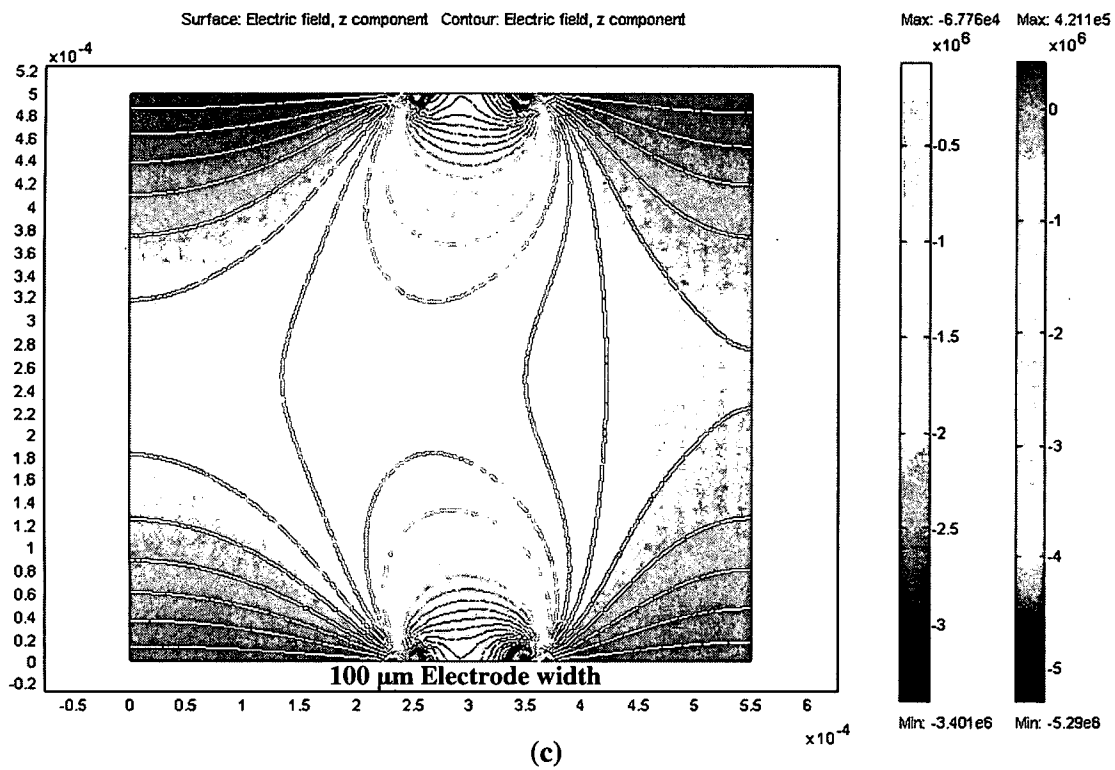
Applied Voltage (V)	Coefficients			Focal Length (cm)
	a	b	c	
100	-2.41E+06	53.17	-0.25658	-81.63
200	-9.65E+06	212.68	-1.0263	-20.41
300	-2.17E+07	478.53	-2.3092	-9.1
400	-3.86E+07	850.73	-4.1053	-5.1
500	-6.03E+07	1329.3	-6.4145	-3.27

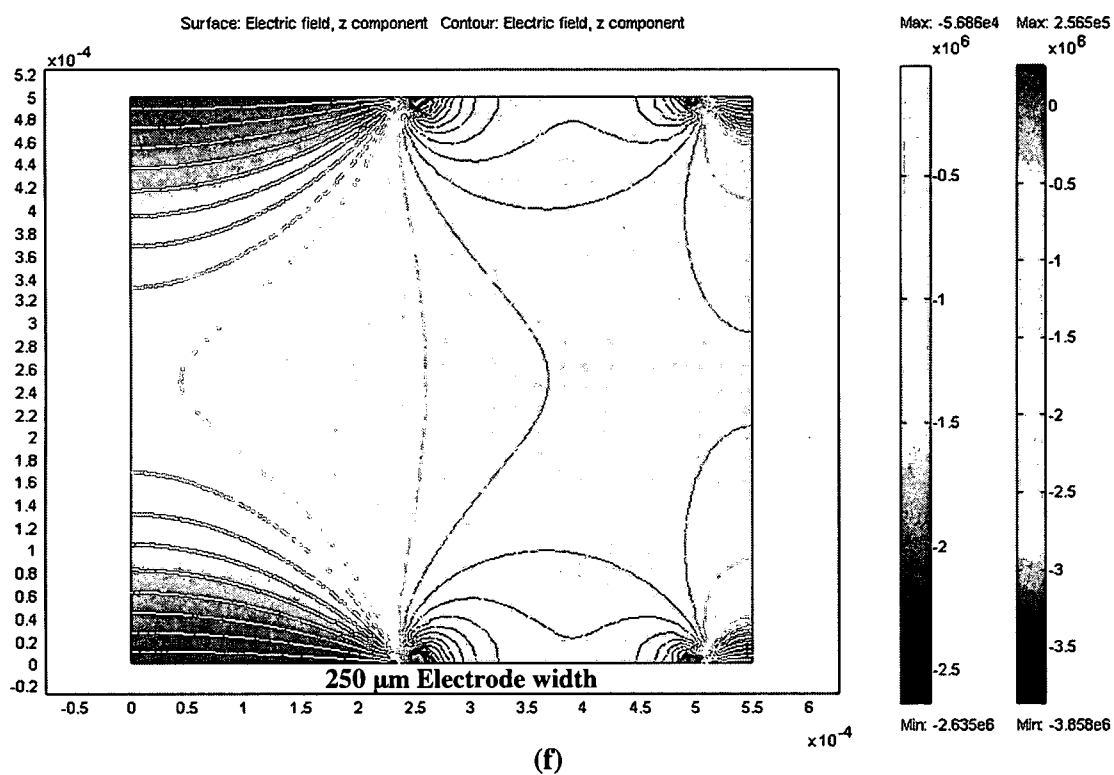
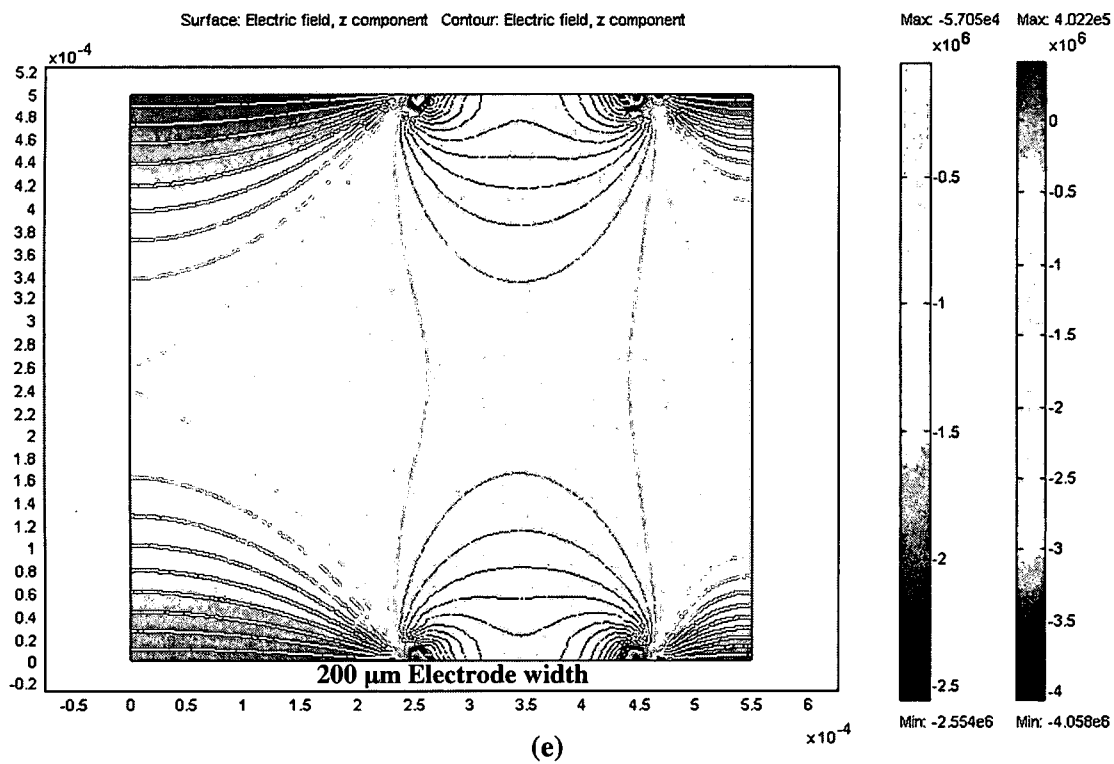
Table 4.1 The fitting coefficients of Equation 4.3 for the simulated net $\Delta\varphi$ for various applied voltages and the corresponding focal length based on Equation 4.5.

4.3.3 Effect of Electrode Widths

The main objective of miniaturization is achieving many devices on one chip and system integration. In the microlens array case, the need for integrating many lenslets closely packed is important for some applications. The limiting factor for close packing arrangement for the electro-optic microlens is the electrode width, hence the difference between the inner and outer electrode radiuses r_1 , r_2 . The electrode shape will affect the electrostatic field distribution within the lens structure, hence the induced refractive index change for various electrode widths. Ultimately this will impact the over all induced lens properties. In Figure 4-11 we examine the effect of electrode width on the z-component of the electrostatic field.







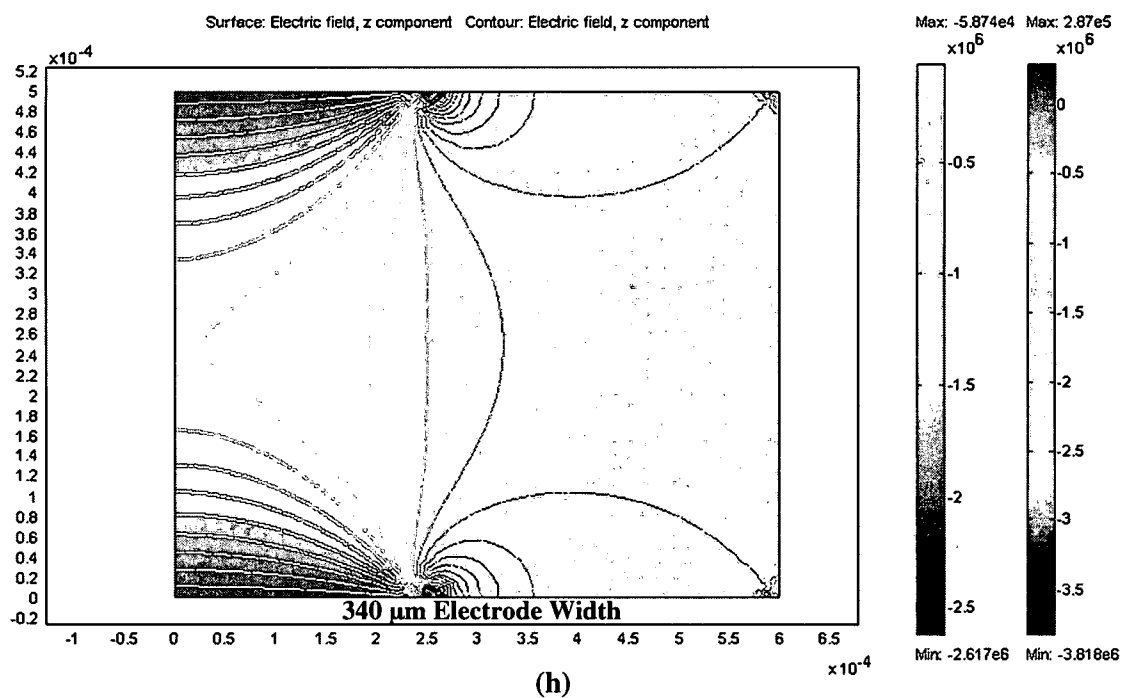
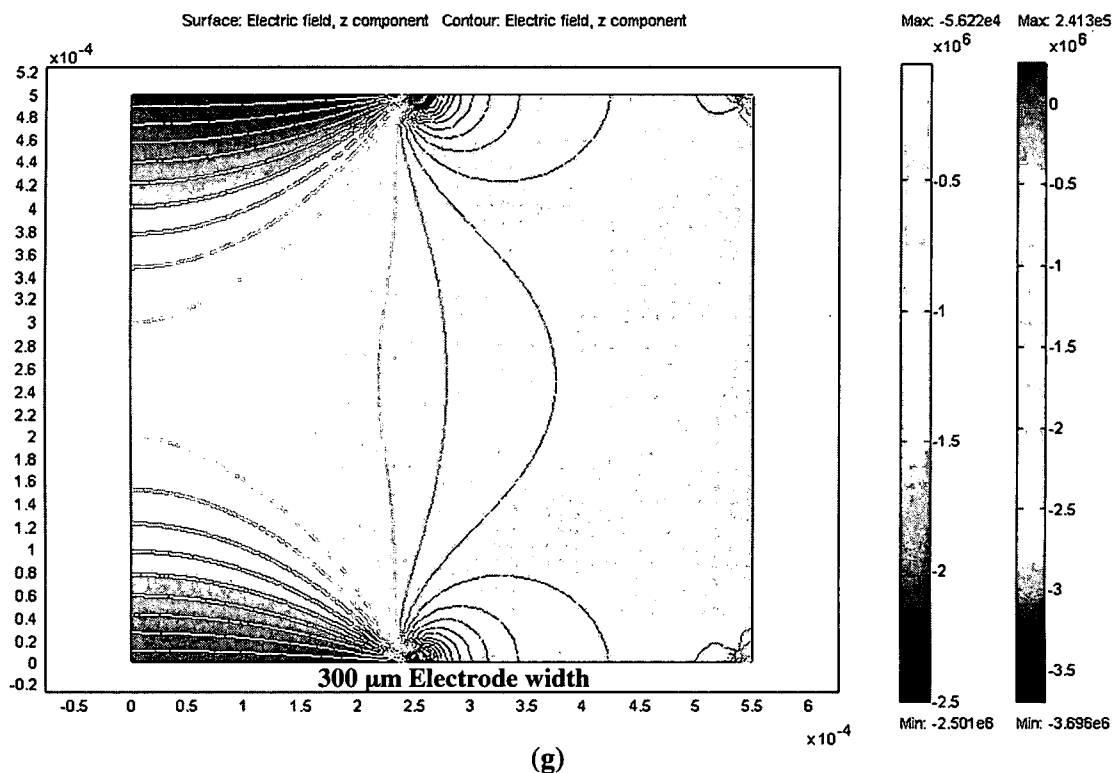


Figure 4.11 Surface and contour plots of the electrostatic field variation, z-component as a function of electrode width. Note that as the electrode widths increase the field changes becomes less.

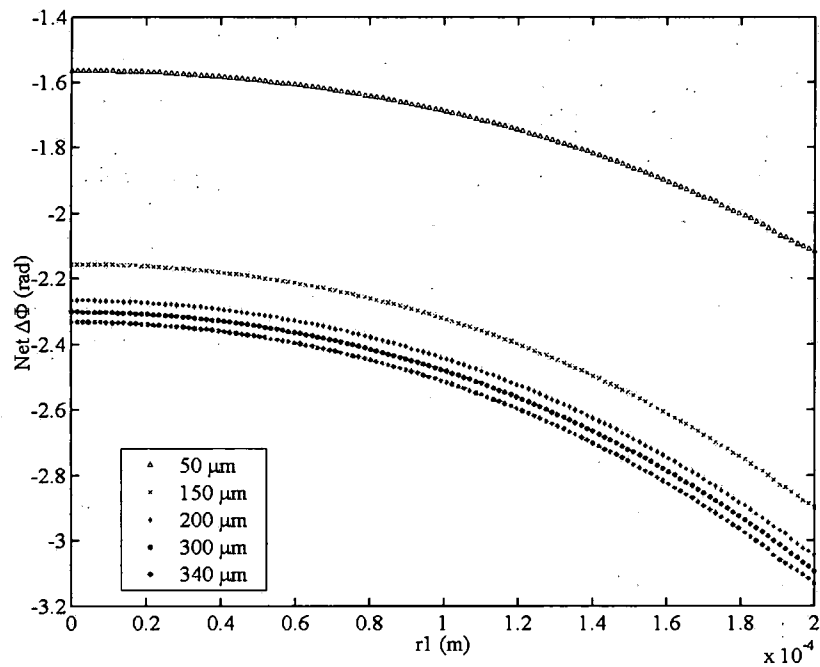


Figure 4.12 The net phase variation for various electrode widths at 300 V.

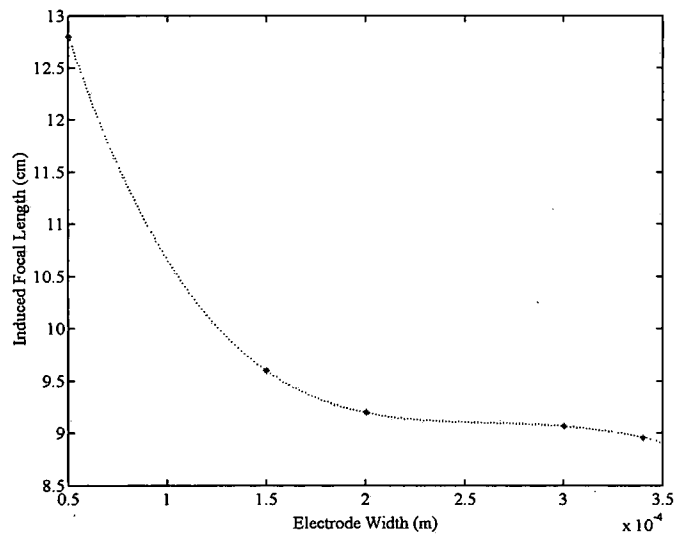


Figure 4.13 Effect of electrode width on the focal length variation. Note that the focal length values are moving towards saturation as the electrode width becomes very large

4.4 Experimental Determination of Focal Length

Using the z-scan method developed earlier we can determine the focal length. Since the finite element model predicts focal length in the range of 5- 80 cm, we have simulated part of this range in Figure 4.14. We have obtained the slope around $\Delta z = 0$ for each applied voltage z-scan on Figure 4.15a,-e for 100-500 V respectively. The resultant number is compared to the simulated numbers of Figure 4.14. In Figure 4.16 we compare the results listed in Table 4.1, i.e. simulated focal length values with that obtained from measurements. We note that at low voltage the difference between the measured and simulated focal length is much larger than those at higher voltages. The reason for that is under investigation.

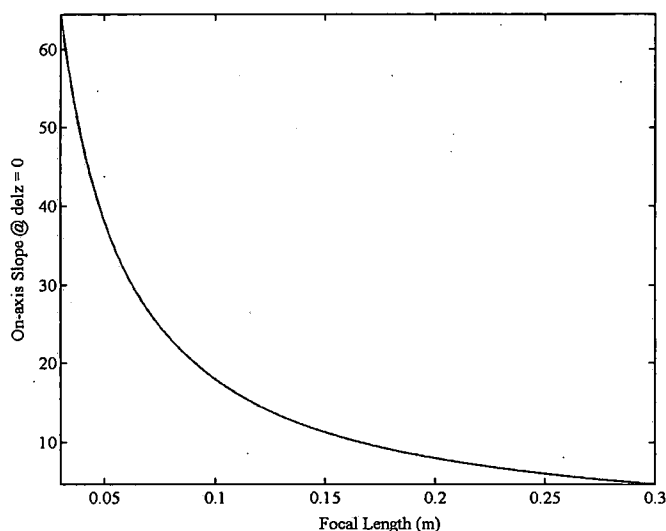


Figure 4.14 On-axis slope as a function of focal length. This is simulated data for longer focal length lenses.

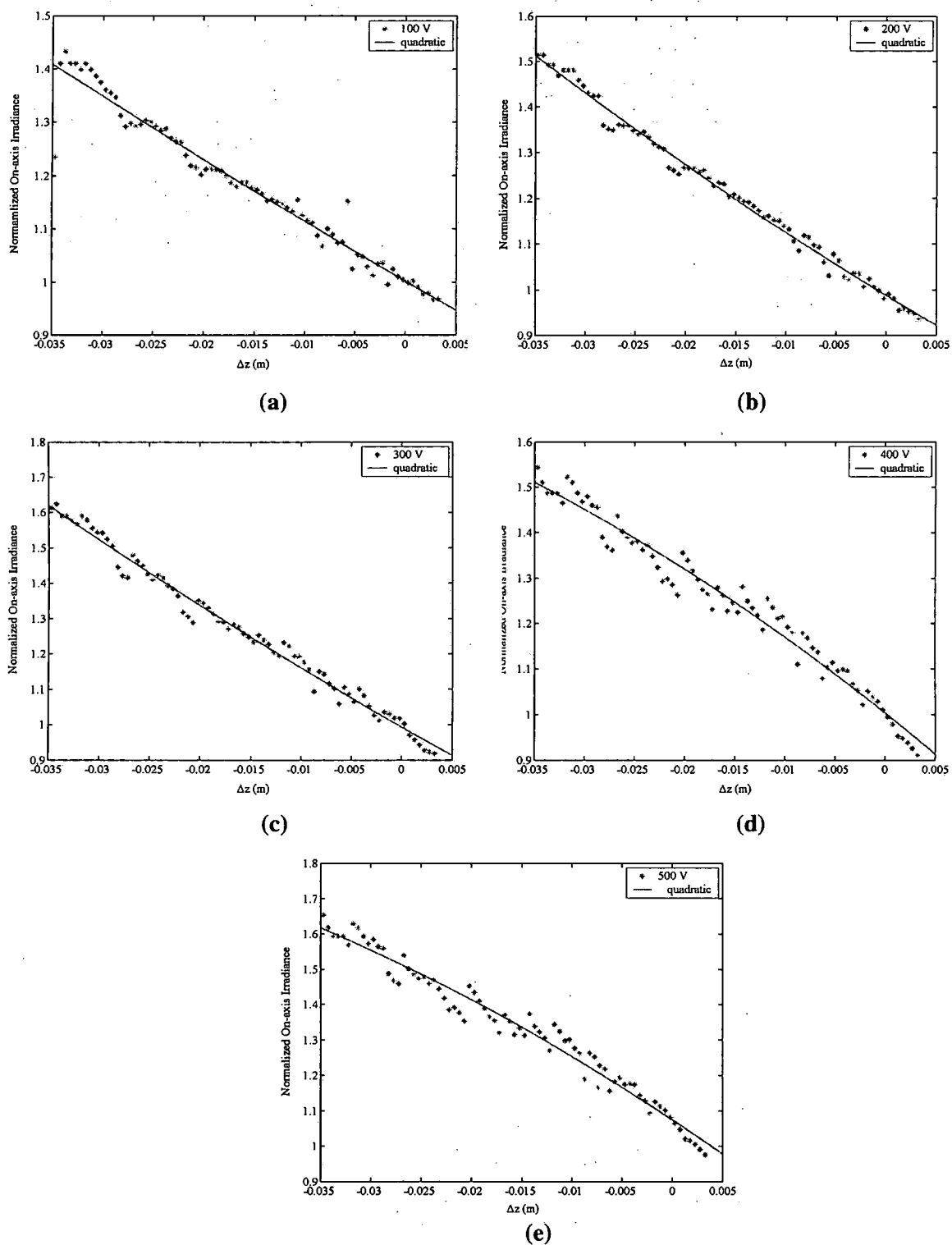


Figure 4.15 The measured on-axis irradiance as a function of Δz for various applied voltages. The quadratic fit is based on Equation 2.43.

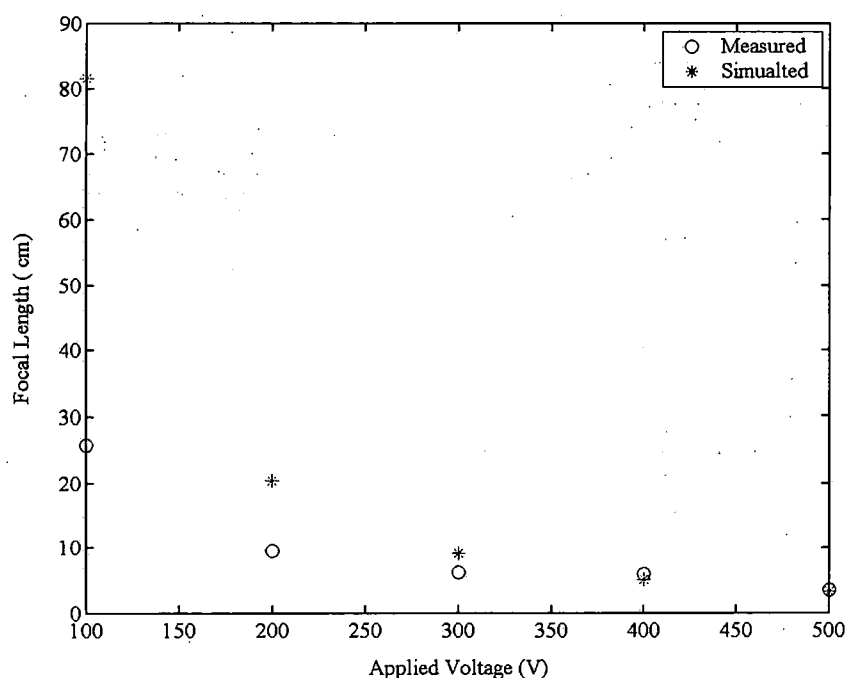


Figure 4.16 A comparison between the simulated and measured focal lengths.

4.5 Experimental Results

There are 2 sets of fabricated devices have been made. The first set was made of 2" non-polished PLZT wafers, while the second set was made of 4" polished wafers. Both sets were of 9/65/35 composition. The set of wafers was used to characterize EO properties of PLZT and get some idea of the micro-lens behavior for various electrode sizes.

It was necessary to lap and polish the PLZT wafers to flat-parallel surfaces with minimal surface roughness for optical clarity. To achieve this goal, blocking techniques was implemented in the manner described elsewhere [110]. The AFM surface scan of the polished PLZT is indicate Figure 4.17. We have achieved of 1-2 nm RMS value for the surface roughness with thickness uniformity of $\pm 2\mu m$ for 2" wafer. However, surface parallelism was not measured. This can be done using standard flat as the reference. By placing the polished PLZT wafer on top of the flat and using monochromatic light to

illuminate the wafer, we get interference fringes that the spacing between them will relate to the non-uniformity of the surfaces parallelism.

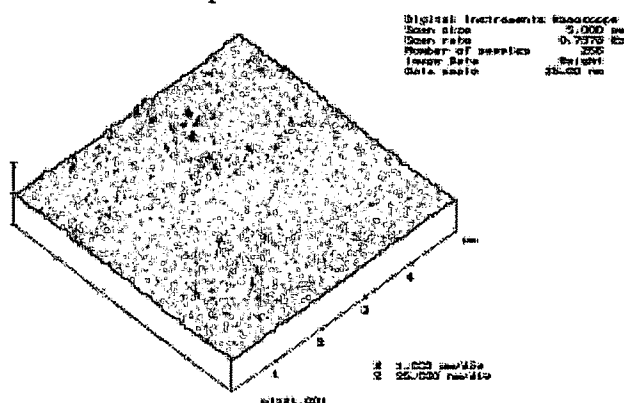


Figure 4.17 The AFM scan of polished PLZT wafer using the blocking technique described in [110].

The first set of fabricated structures is shown in Figure 4.18. We have utilized ITO as the electrodes. The laser drilled plastic package in (a) and the final packaged wafer. The electrical contacts were made by using conductive epoxy within the through holes while attaching electrical wiring. The longitudinal light modulator areas and the various lenslet arrays are indicated on Figure 4.18b. We have measured the resistivity of the ITO electrodes using 4-point probe. The sheet resistance value, after ITO annealing was $20 \Omega/$. It is worth noting the high wafer transparency and excellent optical surface.

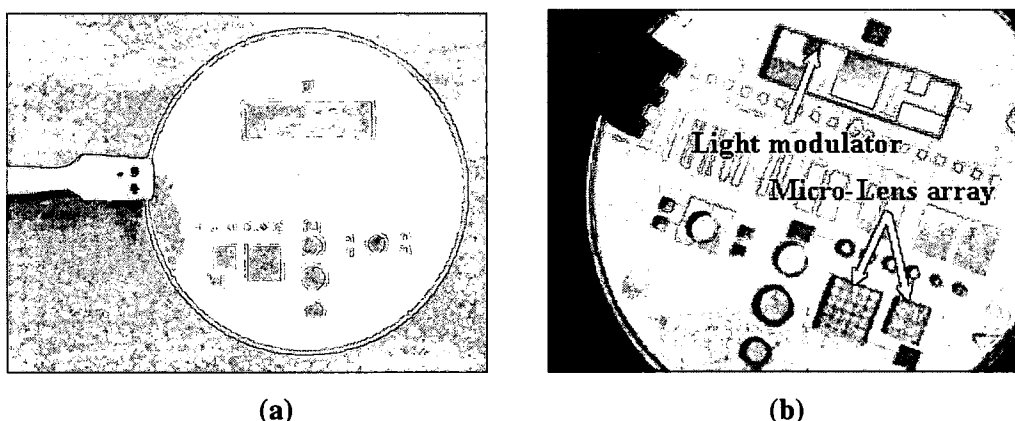
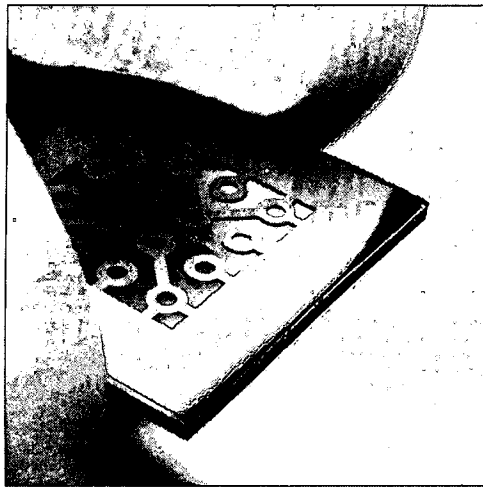
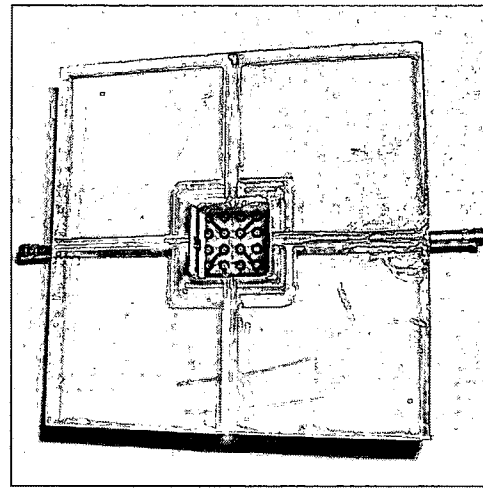


Figure 4.18 Packaging of the electro-optic module: (a) laser micromachined vias etched in a 2" plastic wafer, and (b) the final PLZT packaged module.

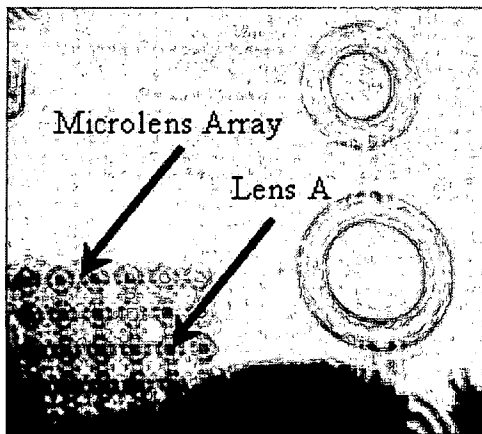


(a)

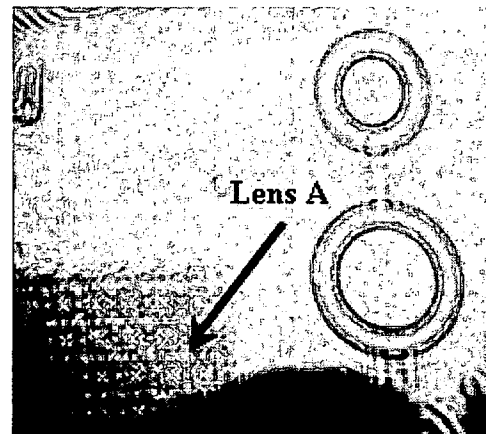


(b)

Figure 4.19 (a) A 1cm^2 die diced off a 4" wafer. The wafer's thickness was $500\mu\text{m}$ and contains 57 dies with various lens design. As mentioned in Chapter 3; (b) the packaged device that was tested.



(a)



(b)

Figure 4.20 A mini-picture of the experimental testing of the micro-lens array at different applied voltages, (a) at 50 V, and (b) at 150 V.

In Figure 4.19a we have a sample die with 12 lenslet array of $500\mu\text{m}$ size. The complete packaged device is shown in Figure 4.19b.

4.6 Micro-lens Array Results

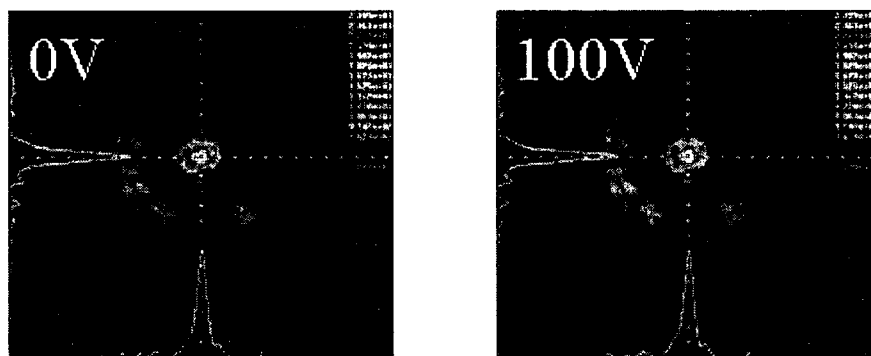
The qualitative experimental results of the micro-lens array PLZT module shown in Figure 4.18 is depicted in the micrograph of Figure 4.20. It is noticeable the change in

brightness of “Lens A” shown in Figure 4.20a-b, at 50 V and 150 V respectively. It is worth noting the electrode array used in our fabrication was transparent ITO. These lenslet have $300\mu m$ aperture size and the substrate thickness was $280\mu m$.

4.6.1 Aperture Effects

Earlier, in Chapter 2, we have pointed out that by taking the lens aperture effects into account one can characterize the lens aberration. Although we have not developed, rigorously, the theory for that, nonetheless Equations (2.32) and (2.33) can give us an indication whether the focal length increases or decreases with the increasing of the applied voltage. Furthermore, the on axis intensity variation will depend on the location of the location of the lens as explained in Section 2.6.2.1.

We have set up a lenslet right before the external lens focal point such that the lenslet aperture is smaller than the optical beam size. Using SPIRICON beam profiler we recoded micrographs of the diffraction pattern variation as we change the applied voltage. These results are shown in Figure 4.21. Note that the main lobe of the Airy pattern diminishes as voltage increases.



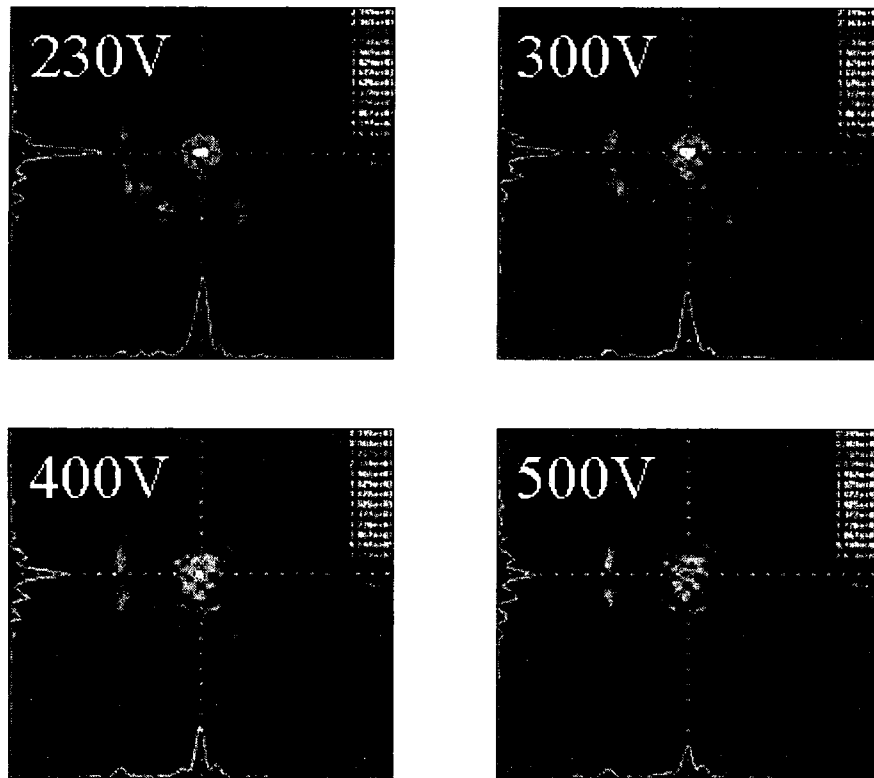


Figure 4.21 A photograph sequence taken by SPIRICON laser beam profiler of the diffraction pattern, of a lenslet, variation as a function of the applied voltage. The lenslet was set before the focal point of the external lens such that a Gaussian beam much larger than it aperture.

We also measured the Airy pattern main lobe size as a function of the applied voltage. The results are shown in Figure 4.22. Note that the linear dependence of the main lobe size. This is expected based on the results shown Figure 4.21, and Equation (2.33).

Finally, the intensity of the main lobe was measured as function of the applied voltage as shown in Figure 4.23. We find these results consistent with Equation (2.32) and also indicate that focal length of the lenslet under test decreases with higher applied voltages.

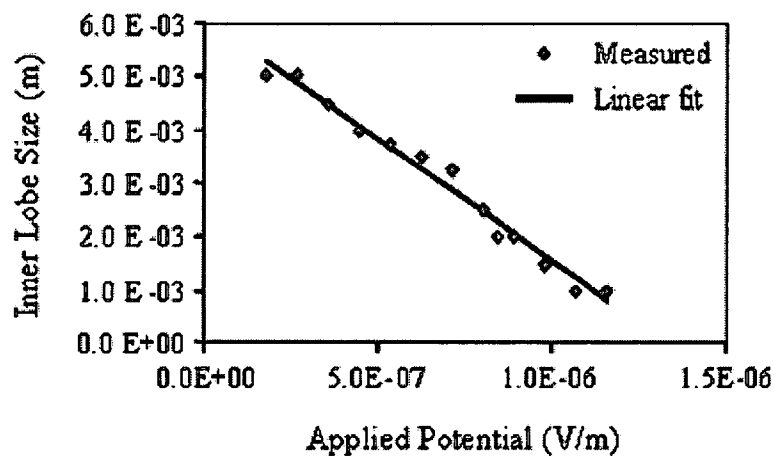


Figure 4.22 The inner lobe size of Airy pattern as a function of the applied potential. The lens under test was located before the focal point of the external lens f_2 .

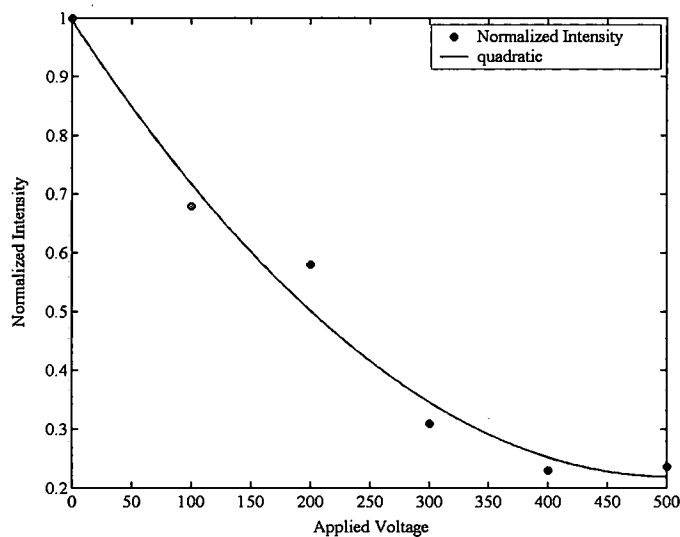


Figure 4.23 The measured on-axis intensity variation of the inner diffraction lobe with the applied voltage. Note the quadratic dependence, as indicated by Equation 2.32. This also means that the focal length decreases with higher voltages values.

Chapter 5

Beam Shaping using Hybrid Acousto-Optics with Feedback

5.1 Summary

In this chapter, we demonstrate that using electronic feedback one can obtain beam shaping in a hybrid acousto-optic device. Feedback, as used and illustrated in the following sections, helps to generate the additional sound pressure which can give beam shaping. Previous analysis of hybrid acousto-optic devices with feedback have been restricted to plane wave treatments only. We shall show that over a region of convergence, one can achieve beam shaping by using the detected optical output and feeding it back, electronically, together with the external radio frequency (RF) input signal. This is fundamentally different than just increasing the electrical input to the transducer.

In general, we can also select a certain range of spatial frequencies at the optical detector and use this for feedback purposes, this way; we are selectively feeding back a range of spatial frequencies of the optical beam, hence have better control over the resulting beam shape. Furthermore, this method lends itself for automatic beam shaping as we will indicate later.

5.2 Background

For over four decades, acousto-optic (AO) interactions have been extensively studied and applied to signal processing. AO modulators (AOMs) are 1-dimensional (1-D) devices in

the sense that light is diffracted in the direction of propagation of the sound. The use of AOMs for image processing has been more recently explored [92-98]. The novel feature of this technique is that lensless optical image processing can be achieved without the use of Fourier plane spatial filters. In fact, the 2-D optical image interacts with the sound fields in the AOMs, and the scattering or diffraction of the 2-D optical image actually carries the processed versions of the original 2-D input image. While 1-D image processing can be performed with one AOM, 2-D processing requires two AOMs with the sound field in each AOM propagating in the two orthogonal transverse directions. The processing operation is programmable in real-time by electronically varying the sound amplitude or frequency within the AOM.

The easiest way to understand lensless spatial filtering of images using AO is through spatial transfer functions describing AO interaction between the sound-induced moving grating and the input angular plane wave spectrum of the light field. The spatial transfer functions for an AO modulator working in the Bragg regime have been derived recently to show the spatial frequency selectivity of both the diffracted and the un-diffracted orders [92-99]. In short, under certain conditions, the undiffracted order has the characteristics of spatial high-pass filtering or spatial derivative operation [100] on the image, while the transfer function for the diffracted order shows low-pass characteristics. 2-D edge enhancement and corner detection have also been achieved with two AO cells with orthogonally propagating sound [96,101].

Previously, M. McNeill et al have studied, theoretically, Gaussian beam profile shaping by acousto-optic Bragg diffraction [118]. In this chapter, an electronic feedback is incorporated into the AO interaction scheme to demonstrate the enhancement in

performance of spatial filtering starting with a fixed value of the sound amplitude through the AO cell, and varying the feedback parameter.

Hybrid AO feedback devices have been used before to demonstrate optical hysteresis and bi-stability [119-122]. In addition, the effect of feedback on beam quality of the undiffracted and diffracted orders from an AO cell operating in the near-Bragg regime will be demonstrated. Both positive and negative feedback are studied, and the feedbacks from the detected undiffracted as well as diffracted orders are investigated.

5.3 AO Cell Spatial Transfer Functions for near-Bragg Incidence

For the benefit of readers, a summary of the essential steps in the derivation of the interaction transfer function during the diffraction of light by ultrasound in an AOM are introduced. Figure 5.1 shows the scattering of an arbitrary light field, ψ_{inc} , incident nominally at the Bragg angle ϕ_B , on the AOM. For Bragg incidence there are primarily two scattered orders, ψ_0 and ψ_{-1} . In order to derive the interaction transfer functions, the wave equation for a 2-D optical field $\vec{E}(x, z, t)$ polarized in the y-direction in the AOM is used:

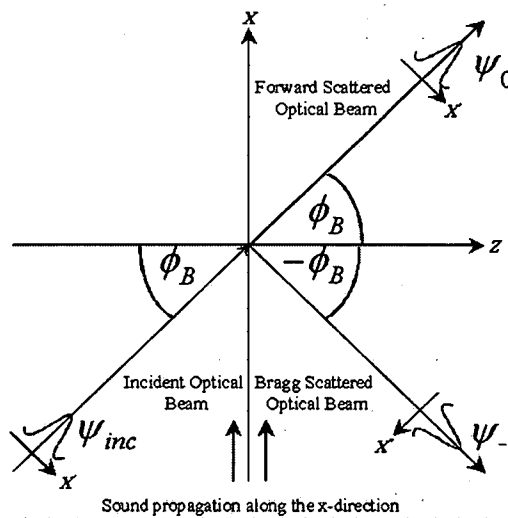


Figure 5.1 Diagram of the sound-light interaction.

$$\frac{\partial^2 \bar{E}}{\partial t^2} - v^2 \nabla^2 \bar{E} = -\left(\frac{\epsilon'}{\epsilon_0}\right) \frac{\partial^2 \bar{E}}{\partial t^2}, \quad (5.1)$$

where v is the light velocity in the AO medium, ϵ_0 is the intrinsic permittivity in the AO medium, and ϵ' represents the acoustically driven perturbation in the permittivity. The optical field in the AO cell can be expressed as

$$\bar{E}(x, z; t) = \sum_m \text{Re}[\psi_m(x, y, z) \exp(j[\omega_m t - k_{mx} x - k_{mz} z])] \hat{a}_y. \quad (5.2)$$

In Equation (5.2), ψ_m represents the complex amplitude of the m^{th} diffracted order; ω_m is the temporal frequency of the m^{th} order light; and k_{mx}, k_{mz} represent the x and z components of the propagation constants of the m^{th} scattered order. Also, \hat{a}_y is the unit vector along the y -direction. From a simple heuristic treatment of acousto-optics, it is readily seen that

$$\omega_m = \omega_0 + m\Omega, \quad (5.3)$$

where ω is the original angular frequency of the incident light, ω_m is the optical frequency of the m^{th} order diffracted light beam, and Ω is the angular frequency of the sound. The Bragg angle is defined as:

$$\phi_B \cong \frac{K}{2k} = \frac{\lambda_0}{2\Lambda n_0}, \quad \phi_m \cong \phi_{inc} + mK/k, \quad (5.4)$$

where λ_0 is the light wavelength in the free space, n_0 is the intrinsic refractive index of the AOM, Λ is the sound wavelength in the AOM, k represents the propagation constant of the light in the AO medium, and K is the propagation constant of the sound. Hence,

$$k_{mx} = k \sin \phi_m \text{ and } k_{mz} = k \cos \phi_m.$$

Assume a sound field is propagating along the positive x -direction with amplitude $S_e(x, z)$ in the AOM:

$$\varepsilon' = \varepsilon_0 \cdot C \cdot \text{Re}\{S_e(x, z) \exp j(\Omega t - Kx)\}, \quad (5.5)$$

where C is the AO interaction constant. Furthermore, assume $S_e(x, z) = A$, a constant, for simplicity. Upon substituting Equation (3.2) and (3.5) into Equation (5.1), and gathering the coefficients of $\exp j[\omega_0 + m\Omega]t$, we obtain

$$\begin{aligned} \frac{\partial^2 \psi_m}{\partial x^2} - 2j \left(k_{mx} \frac{\partial \psi_m}{\partial x} + k_{mz} \frac{\partial \psi_m}{\partial z} \right) + \left(\frac{k^2 C}{2} \right) \{ A \psi_{(m-1)} \exp[-j(k_{(m-1)z} - k_{mz})z] \\ + A^* \psi_{(m+1)} \exp[-j(k_{(m+1)z} - k_{mz})z] \} + \frac{\partial^2 \psi_m}{\partial y^2} + \frac{\partial^2 \psi_m}{\partial z^2} = 0. \end{aligned} \quad (5.6)$$

We assume slow variation of ψ_m w.r.t. z , i.e.,

$$\left| \frac{\partial^2 \psi_m}{\partial z^2} \right| \ll \left| k_{mz} \frac{\partial \psi_m}{\partial z} \right|. \quad (5.7)$$

This assumption is consistent with the conventional paraxial approximation of the Helmholtz equation in diffraction theory, which yields the Fresnel diffraction formula and the transfer function for propagation in a homogeneous medium [123]. For beam widths greater than a few wavelengths of light, the paraxial approximation gives accurate results, and thus is also used in all beam propagation methods [123]. In our case, we also assume that the wavelength of ultrasound is much larger than the wavelength of light (true for ultrasound frequencies from 10-100 Mhz); hence the slowly varying approximation above is justified. Using (5.7), Equation (5.6) becomes

$$\frac{\partial^2 \psi_m}{\partial x^2} - 2j \left(k_{mx} \frac{\partial \psi_m}{\partial x} + k_{mz} \frac{\partial \psi_m}{\partial z} \right) + \left(\frac{k^2 C}{2} \right) \{ A \psi_{(m-1)} \exp[-j(k_{(m-1)z} - k_{mz})z] \\ + A^* \psi_{(m+1)} \exp[-j(k_{(m+1)z} - k_{mz})z] \} + \frac{\partial^2 \psi_m}{\partial y^2} = 0.$$

$$+ A^* \psi_{(m+1)} \exp[-j(k_{(m+1)z} - k_{mz})z] + \frac{\partial^2 \psi_m}{\partial y^2} \approx 0. \quad (5.8)$$

Finally, upon Fourier transforming Equation (5.8), we find that the angular plane wave spectra of the various diffracted orders evolve according to

$$\frac{\partial \hat{\psi}_m}{\partial z} = j \frac{(k_x^2 + 2k_x k_{mx})}{2k_{mz}} \hat{\psi}_m + j \frac{k_y^2}{2k_{mz}} \hat{\psi}_m - jD \hat{\psi}_{m+1} - jE \hat{\psi}_{m-1}, \quad (5.9)$$

where

$$D = (kCA^* / 4) \cdot \exp[-jk(\cos(\phi_{m+1}) - \cos(\phi_m))z], \quad (5.10a)$$

$$E = (kCA / 4) \cdot \exp[-jk(\cos(\phi_{m-1}) - \cos(\phi_m))z]. \quad (5.10b)$$

In Equation (3.9), the angular spectra of the various scattered orders $\hat{\psi}_m$ are defined according to the Fourier transform relation given as

$$\hat{\psi}_m(k_x, k_y; z) = \mathfrak{F}_{xy} \{ \psi_m(x, y, z) \} = \int_{-\infty}^{\infty} \int_{-\infty}^{\infty} \psi_m(x, y, z) \exp(jk_x x + jk_y y) dx dy. \quad (5.11)$$

Also, in Equation (5.9), the first two terms on the right hand side represents the propagational diffraction effect; while the last two terms model the AO interaction.

For nominal Bragg incidence ($\phi_{inc} = \phi_B$), only the 0th and -1st diffracted orders exist and exact analytical expressions for the interaction transfer functions can be determined. For instance, from Equation (5.9) and for $\phi_{inc} = \phi_B$, we obtain

$$\frac{\partial \hat{\psi}_0}{\partial z} = \frac{j[k_x^2 + 2k_x k_{0x}]}{2k_{0z}} \hat{\psi}_0 + j \frac{k_y^2}{2k_{0z}} \hat{\psi}_0 - jE \hat{\psi}_{-1}, \quad (5.12)$$

$$\frac{\partial \hat{\psi}_{-1}}{\partial z} = \frac{j[k_x^2 + 2k_x k_{-1x}]}{2k_{-1z}} \hat{\psi}_{-1} + j \frac{k_y^2}{2k_{-1z}} \hat{\psi}_{-1} - jD \hat{\psi}_0, \quad (5.13)$$

where $k_{0x} = k \sin \phi_B$, $k_{0z} = k \cos \phi_B$, $k_{-1x} = k \sin \phi_B$, $k_{-1z} = k \cos \phi_B$. The constants D and E are simplified to $D = kCA^*/4$, $E = kCA/4$ because $\phi_{inc} = \phi_B$ and $\phi_{-1} = \phi_0 - 2\phi_B = -\phi_B$. From Equations (3.12) and (3.13), one can obtain the spatial transfer functions analytically for undiffracted and first diffracted orders as

$$H_0(k_x, z = L) = \exp \left[j \left(\frac{(k_x^2 + k_y^2)L}{2k} \right) \right] \left\{ \cos \left(\sqrt{\left(\frac{k_x k_{0x} L}{k} \right)^2 + \left(\frac{\alpha}{2} \right)^2} \right) + \left(\frac{jk_x k_{0x} L}{k} \right) \frac{\sin \left(\sqrt{\left(\frac{k_x k_{0x} L}{k} \right)^2 + \left(\frac{\alpha}{2} \right)^2} \right)}{\sqrt{\left(\frac{k_x k_{0x} L}{k} \right)^2 + \left(\frac{\alpha}{2} \right)^2}} \right\}, \quad (5.14)$$

$$H_{-1}(k_x, z = L) = \exp \left[j \left(\frac{(k_x^2 + k_y^2)L}{2k} \right) \right] \left(-j \frac{\alpha}{2} \right) \frac{\sin \left(\sqrt{\left(\frac{k_x k_{0x} L}{k} \right)^2 + \left(\frac{\alpha}{2} \right)^2} \right)}{\sqrt{\left(\frac{k_x k_{0x} L}{k} \right)^2 + \left(\frac{\alpha}{2} \right)^2}}, \quad (5.15)$$

where $\alpha = kC|A|L/2$ represents the peak phase delay of the light due to the AO interaction which is proportional to the sound pressure. L is the AO interaction length.

Also note that $\frac{k_{0x}L}{k} = \frac{Q\Lambda}{4\pi}$, where $Q = \frac{2\pi\lambda_0 L}{\Lambda^2 n_0}$ is the Klein-Cook parameter (for

definitions of notation, see [95]). The propagational diffraction effect through the length of AO cell is represented by the $\exp[j((k_x^2 + k_y^2)L/2k)]$ phase term. The remaining terms in Equations (5.14), (5.15) characterize the AO interaction process. Equations (5.14), (5.15) show that, in essence, the propagational diffraction effects are decoupled from the AO interaction process. Plots of the transfer functions appear in [96-97], and the physical explanation for the nature of the variation as a function of spatial frequency is given in

[101]. Briefly, a departure from the ideal Bragg incidence of a plane wave component of the incident spectrum will cause a reduction of the diffraction efficiency; therefore, more of the spectrum will be retained in the undiffracted order. Hence, the undiffracted order shows a high-pass spatial frequency response, while the diffracted order shows low-pass characteristics.

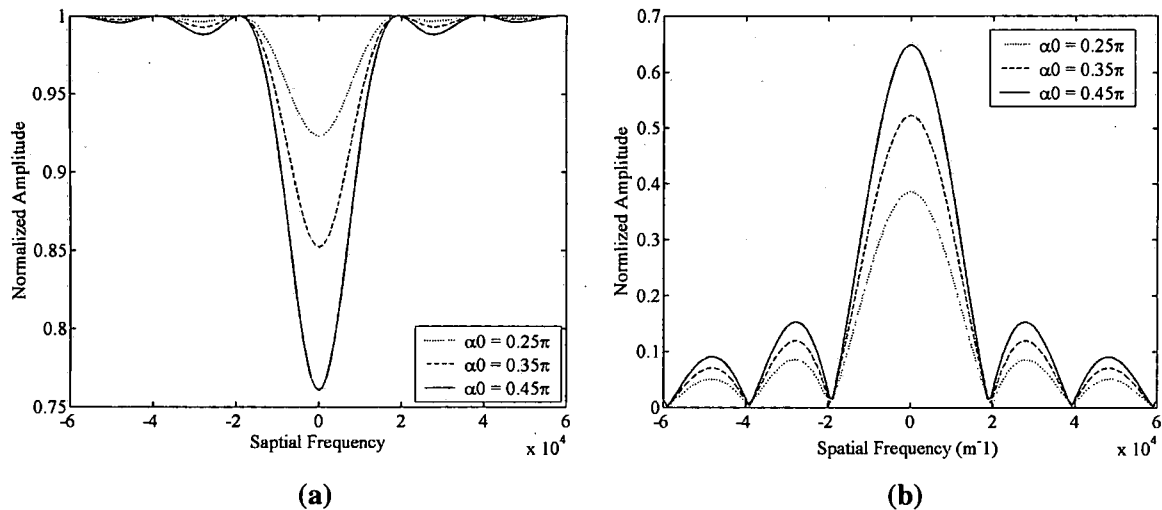


Figure 5.2 AO transfer functions as a function of spatial frequency for (a) the 0th order and (b) the -1st order with $Q \cong 21$ (corresponding to acoustic frequency of 40 MHz).

Figure 5.2 shows a typical variation of the magnitude of the AO transfer functions for the 0th and -1st orders versus spatial frequency k_x . For typical dimensions of the AO cell (IntraAction AOM 40), and typical frequencies of operation for the ultrasound and light, which was used (viz., 30-60 MHz for the ultrasound and light wavelength 633 nm), the corresponding values of the Klein-Cook parameter, Q , typically may vary from 11 to 46. Using the 0th order AO transfer function above, it is readily seen that for an initial Gaussian profile with a spectrum as shown in Figure 5a, the corresponding spectra of the processed profile after it interacts with the sound in the AO cell is as shown in Figure 5b. For an initial of $\alpha_0 = 0.35\pi$, the set of profiles shown in Figure 5.3b correspond to

ultrasound frequencies 30-60 MHz, implying values of Q from 11 to 46, respectively.

From the figures, it is clear that the values of α_0 and Q , along with the waist size of the incident profile, determine the shape of the spectrum of the processed Gaussian beam.

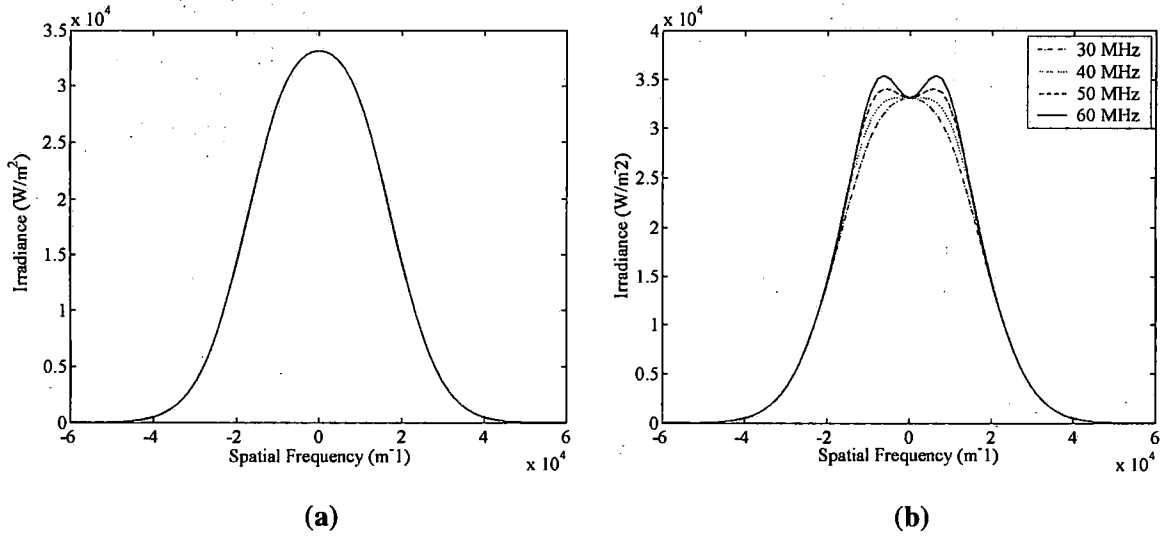


Figure 5.3 (a) The spectrum of input Gaussian profile with a beam waist of $75\mu\text{m}$. (b) the spectrum of processed profile with $\alpha_0 = 0.35\pi$ at acoustic frequencies 30/40/50/60 MHz, which correspond to $Q = 11/21/32/46$, respectively.

5.4 Acousto-optics with External Feedback

In the presence of external feedback as shown in Figure 5.4, the AO transfer function is modified to reflect the change in the peak phase delay. Often this is affected by changing α by an amount proportional to the intensity of 0th or -1st order.

Furthermore, the feedback can be positive or negative. This means that the value of $\Delta\alpha$ fed back into the AO cell can be added to or subtracted from the initial peak phase delay α_0 respectively, according to

$$\alpha = \alpha_0 \pm \Delta\alpha. \quad (5.16)$$

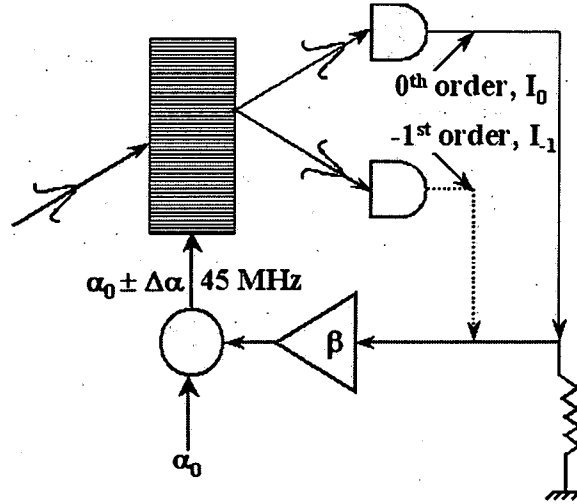


Figure 5.4 Schematic of AO interaction in the presence of feedback, according to Equation (5.16).

For low values of feedback, $\Delta\alpha \approx \beta I_{0,-1}$, where $I_{0,-1}$ is the intensity of the 0th or -1st order, and β is the feedback factor proportional to the gain, G , of the feedback amplifier and the conversion efficiency of the photodetector.

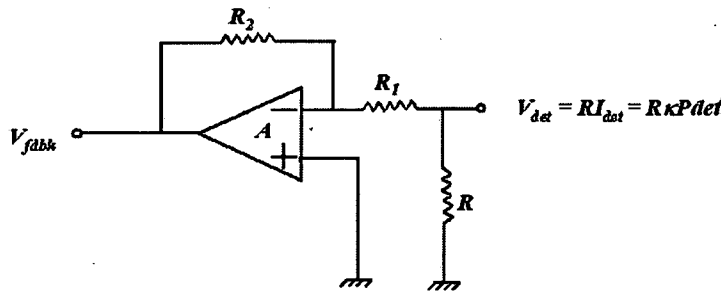


Figure 5.5 The details of the feedback stage necessary for the beam-shaping scheme. The input is $V_{det} = R \kappa P_{det}$, with κ is the responsivity of the photodetector and P_{det} is the detected power. The output is V_{fdbk} .

In what follows, we demonstrate how one can determine $\Delta\alpha$ in an actual experimental setup referring to the feedback circuit in Figure 5.5, where the feedback voltage V_{fdbk} is proportional to the detected power as explained earlier. The voltage, which is proportional to the photodetector current κP_{det} , can be expressed as

$$V_{\text{det}} = \kappa R P_{\text{det}}, \quad (5.17)$$

with κ is the responsivity of the photodetector and P_{det} is the detected power. Thus the feedback circuit output is

$$V_{\text{fdbk}} = -[(\kappa P_{\text{det}})RG] = -\left[(\kappa P_{\text{det}})R\left(\frac{R_2}{R_1}\right)\right]. \quad (5.18)$$

Since the peak phase delay α is proportional to the acoustic power, and hence to the square of the applied voltage, we can express it as

$$\alpha = K(V_{\text{rms}})^2 = K(V_{\text{gen}} + V_{\text{fdbk}})^2, \quad (5.19)$$

where K is a constant that depends on the AO cell. The value of K is best determined experimentally, as shown in the next Section. Hence

$$\alpha = \alpha_0 + \Delta\alpha = KV_{\text{gen}}^2 + 2KV_{\text{gen}}V_{\text{fdbk}} + KV_{\text{fdbk}}^2 \quad (5.20)$$

and from Equation (5.20)

$$\alpha_0 = KV_{\text{gen}}^2, \quad (5.21)$$

$$\Delta\alpha = 2KV_{\text{gen}}V_{\text{fdbk}} + KV_{\text{fdbk}}^2. \quad (5.22)$$

For low values of V_{fdbk} ($\ll V_{\text{gen}}$), $\Delta\alpha$ is proportional to the detected power, and hence to the detected intensity $I_{0,-1}$. In the following section, the determination of α_0 and the experimentally determined value of K will be explained.

5.5 Simulation Scheme and Results

In our simulation, we have used the far field intensity of the diffracted 0th and -1st orders as the feedback to update the value of α . Both positive and negative feedback are implemented in the simulations. This allows for a wide range of predicted beam shapes and intensities in the undiffracted and diffracted beams.

In order to achieve realistic simulation results, the value of K has been experimentally determined and utilized in the MATLAB program used for the simulation. To do this, we have measured integrated powers over the detector surface area from the 0th and -1st orders for a given value of the voltage driving the acoustic transducer. Using the simplified plane wave interaction theory,

$$I_0 = I_{inc} \cos^2(\alpha/2), \quad (5.23a)$$

$$I_{-1} = I_{inc} \sin^2(\alpha/2), \quad (5.23b)$$

with

$$\alpha = KV_{rms}^2, \quad (5.23c)$$

where V is the root mean square, RMS, value of the electrical signal driving the transducer and K is a proportionality constant. This constant is representative of the conversion efficiency of the acoustic input.

From experimental measurements, the constant K has been determined to be approximately $5.14 \times 10^{-3} \pi / V^2$ for the IntraAction AOM-40 cell. In addition, realistic values for the beam parameters, such as beam waist sizes in the range 50 μm - 75 μm , and a typical beam power of 10 mW, are used in the simulations. The photodetector responsivity κ is taken to be 0.01 A/W.

The MATLAB program used in this work runs iteratively with updated values of $\Delta\alpha$ until convergence is achieved. This means that for each value of the amplifier gain G , a new V_{fdbk} will result, and consequently a new $\Delta\alpha$ will be generated. This $\Delta\alpha$ value is compared to an updated $\Delta\alpha$ that results after one additional pass within the feedback loop. If two successive iterated values of $\Delta\alpha$ are within a tolerance limit, viz. 1% in our

case, we assume convergence of the program; otherwise, the last $\Delta\alpha$ value obtained is used through the loop again. The convergence loop is programmed to run for a maximum of 500 iterations. If convergence is achieved before the end of the 500 loops, the program terminates and takes the last $\Delta\alpha$ as the converged value. In case no convergence is achieved at the end of the 500 loops, the program prints out the last updated $\Delta\alpha$. In either case, once $\Delta\alpha$ is found, the values of the corresponding gain G and the feedback voltage V_{fdbk} are also known. Furthermore, the corresponding beam profiles can be simultaneously calculated. As our numerical results will show later, in some cases, for high positive values of G , the feedback from the -1st order does not converge. Furthermore, for higher positive and negative values of G , feedback from the 0th order may not converge as well. Lack of convergence is equivalent to instability in the system, and may result in bi-stability or multi-stability, which has been predicted and observed in hybrid AO devices with feedback [122].

We now present our simulation results for the effect of feedback on the beam shape. Since the feedback affects the AO transfer function, we present the evolution of the AO transfer functions, for 0th and -1st order, as a function of the feedback variation. Figures 5.6a, 5.6b show the AO transfer functions for the undiffracted and diffracted orders for a range of values of the feedback parameter $\Delta\alpha$ for an initial $\alpha_0 = 0.35\pi$ which corresponds to AO signal amplitude of $V_{rms} = 7.73V$. Figures 5.7a, 5.7b show the corresponding beam profiles, of the 0th order corresponding to 0th and -1st order feedback, respectively for initial Gaussian beam size of $75\mu m$. The set of simulated results in both figures are only for the converged values of $\Delta\alpha$. Note that the beam shapes are nearly identical for identical values of $\Delta\alpha$, irrespective of whether the feedback is from the 0th or -1st order,

as is to be intuitively expected. However, the range of the converged $\Delta\alpha$ is different as

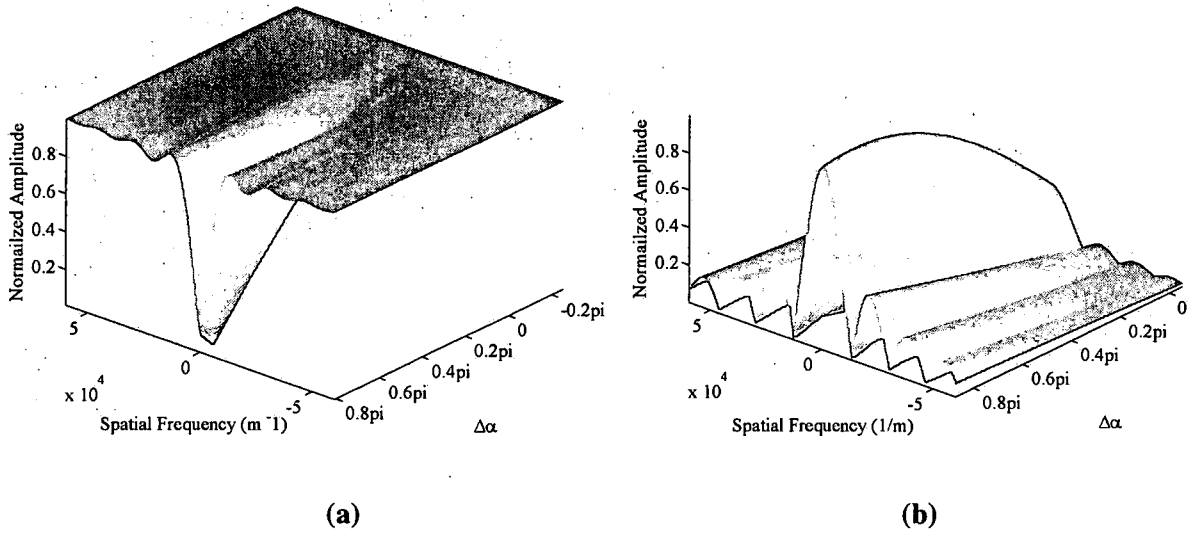


Figure 5.6 The effect of feedback on the AO transfer function, a) 0th order and b) -1st order. The sound frequency is taken as 45 MHz, which is equivalent to $Q = 26$. In this simulation $\alpha_0 = 0.35\pi$ and the incident power is 10 mW.

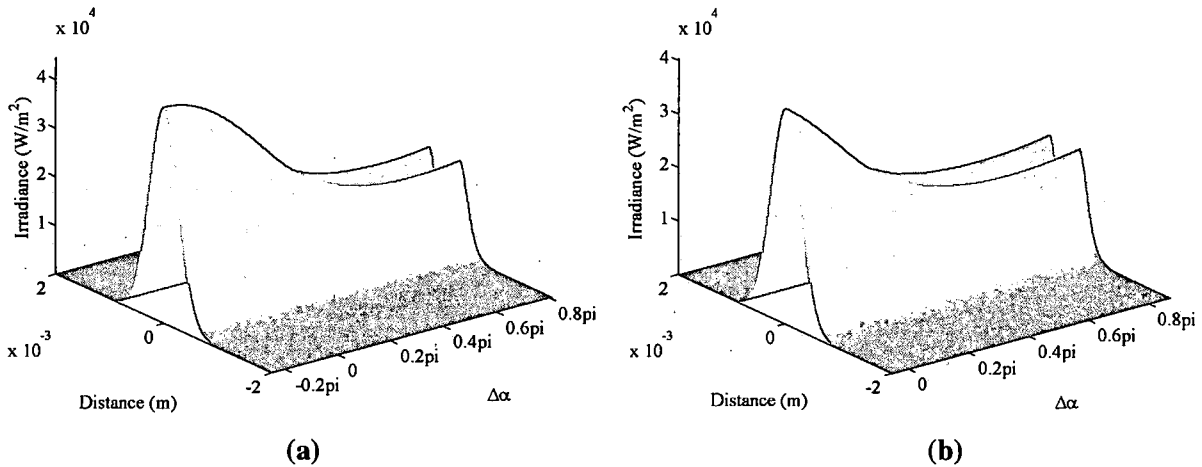


Figure 5.7 Beam shapes for an $75\mu\text{m}$ incident beam of 10 mW, corresponding to the parameters in Figure 5.6 for (a) 0th feedback, and (b) -1st order feedback. The far-field distance is 1 meter.

In order to bring out the effect of feedback on beam shapes, we show in Figure 3.8, typical cross-sections of Figures 5.7a, 5.7b for different feedback parameters. As evident from the figures, there is a unique value of the feedback parameter for a given value of

$\Delta\alpha$ for which the beam shape approaches a flat top profile. The best flat top profiles achieved are drawn in bold dotted lines of Figure 5.8, and occur for the values of $\Delta\alpha$ equal to 0.216π (-1^{st} order) and $0.18\pi - 0.2\pi$ (0^{th} order), respectively, in Figures 8a, 8b. Both of these values correspond to the new peak phase delay α of approximately $0.43\pi - 0.45\pi$, which corresponds to $V_{rms} = 9.2V - 9.36V$.

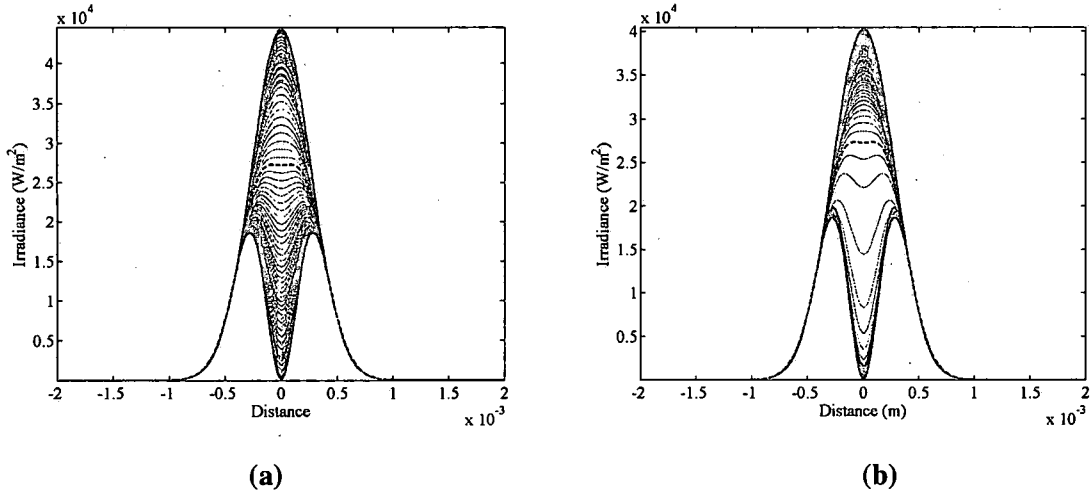
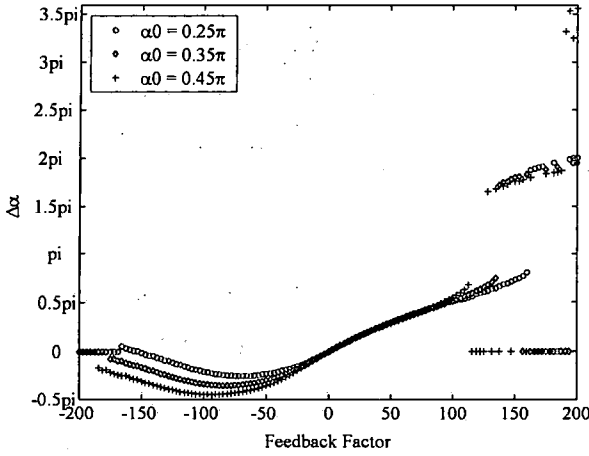
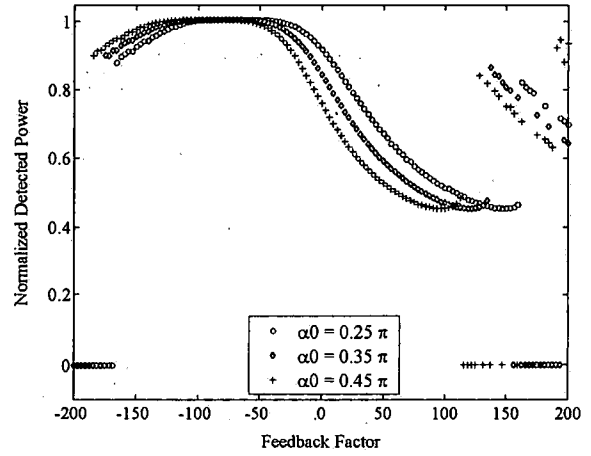


Figure 5.8 A cross section of the 0^{th} order beam shapes from Figure 7. (a) -1^{st} order feedback, and (b) 0^{th} order feedback.

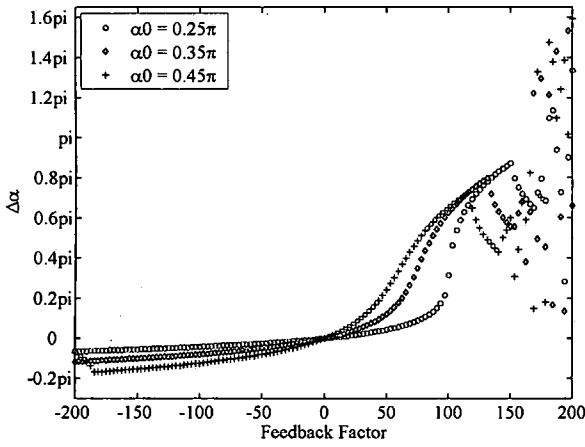
To further investigate the action of the feedback amplifier gain G on beam shaping and convergence issues, we present in Figure 5.9 the results of varying G within ∓ 200 range for various initial peak phase delay α_0 . All plots correspond to the value of Q in Figures 5.6a, 5.6b, input beam size of $75\mu m$ and include the converged and non-converged data points. It is worth noting that results will be different for different Q and initial beam size and shape. Note that the Q , the α , and the input beam profile and size control the beam shaping results.



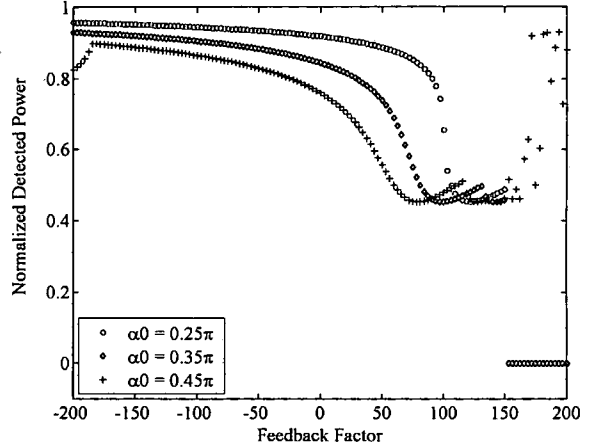
(a)



(b)



(c)



(d)

Figure 5.9 (a) The $\Delta\alpha$ variation with the feedback amplifier gain factor G for various initial α_0 for 0th order feedback; (b) the corresponding normalized power detected in the undiffracted order; (c) The $\Delta\alpha$ variation with the feedback amplifier gain factor G for various initial α_0 for -1st order feedback; (d) the corresponding normalized power detected in the undiffracted order.

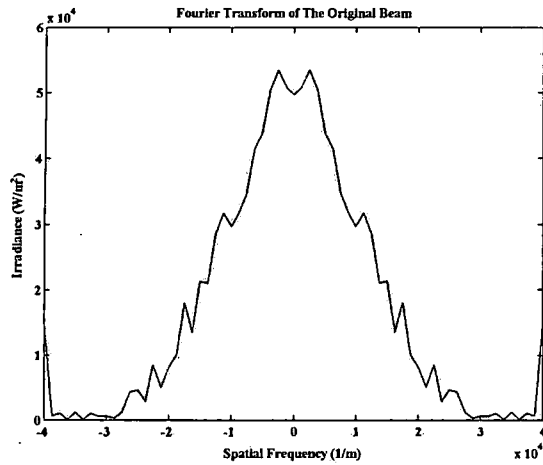
In general for shaping a specific beam, we need the initial beam information that depends on the input beam to automatically control the final beam shape. Figures 5.9a, 5.9c show the plots of $\Delta\alpha$ variation versus the feedback amplifier gain factor G for both 0th and -1st order feedbacks respectively. The corresponding normalized output powers are shown in Figures 5.9b, 5.9d. We observe that there is a range of data where the variations are smooth with a clear trend. Outside this range, most of the values of G give

corresponding values for $\Delta\alpha$ which oscillate between successive increments of G at the end of the 500 iterations with no specific trend. The highest values of α in this case are typically above π . As discussed earlier, this corresponds to lack of convergence or instability. All other values of G (even when converged) yield nonphysical values for $\alpha(>\pi)$. For example for $\alpha_0 = 0.35\pi$, such a convergent range for G lies between ± 165 , where $\Delta\alpha$ and the normalized output power varies smoothly. Typically, in this range, converge is achieved after 3-5 iterations. We note that with the increase of α_0 , the range of G , where convergence is possible, becomes smaller for both 0th and 1st orders feedback, which is expected. Furthermore, we observe that the convergence range for the 1st order feedback is narrower than that of the 0th order feedback case. Finally, non-converged values for $\Delta\alpha$ occur for positive and negative G values for the 0th order feedback, while it occurs only for positive G values for the 1st order feedback case.

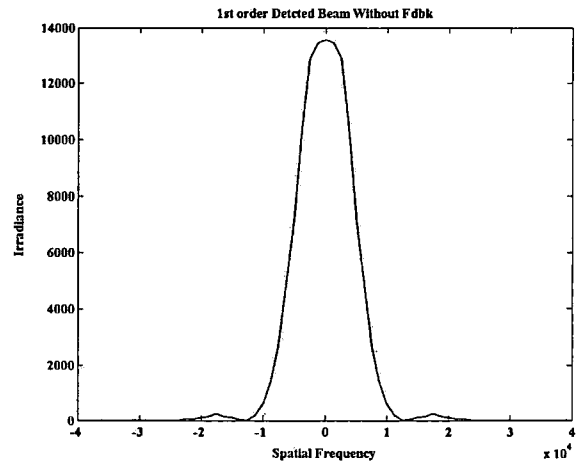
5.6 Concluding remarks: effect on noise cancellation

We have analyzed beam shaping through positive and negative feedback of the undiffracted and diffracted orders in an AO hybrid device with feedback. The results show that beam shaping can be readily achieved by changing the value and the nature of the feedback, along with the peak phase shift. The results will be useful in designing flattop optical profiles for applications in holographic readout. The results can be extended to the design of arbitrary beam profiles and specific spatial frequency selective image processing in the future.

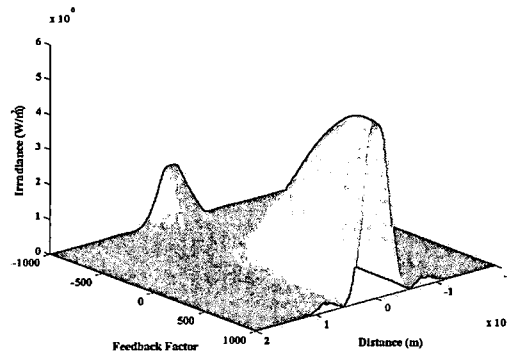
We have furthermore modeled AO interaction with and without feedback in the case when the incident beam has additive high (spatial) frequency noise, as shown in Figure 5.10.



(a)



(b)



(c)

Figure 5.10 The spatial filtering of the high frequency noise as detected from -1st diffracted order. (a) Added high frequency noise in the spatial domain; (b) the detected signal without noise; (c) 3-D representation as a function of the feedback factor.

Consider, first the simpler case of AO interaction without feedback. Due to the frequency selective nature of the transfer functions, as indicated in Figure 5.2 and explained in Section 5.2, it is evident that noise having spatial frequency components centered around 0.5×10^4 radians/m will be attenuated from the -1st diffracted order. The noise rejection will be greater for larger values of α_0 . The first set of simulations performed using normalized values of beam parameters; sound strength etc. verifies this conjecture. Detailed calculations using the realistic parameters used in the report will be

performed in the near future. In the presence of external feedback this effect is expected to be more pronounced for lower values of α_0 due to the added contribution from the feedback to the net α in the AOM.

Chapter 6

Hybrid Acousto-Optics Beam Shaping Results

6.1 Introduction

In this chapter, we will present the preliminary experimental results of the AO beam shaping. First, we will introduce an illustration and detailed explanation of the experimental setup. Data and some analysis will be introduced. Finally, we will close with some remarks.

6.2 Experimental Setup

An illustration of the experimental setup used for the optical beam shaping experiment is shown in Figure 6.1. A HeNe laser beam is focused to $75\mu m$ using a $200mm$ lens into an AO cell. A RF signal generator with a frequency range of 40-60 MHz drives the AO cell. The diffracted and undiffracted beams output of the AO pass through a beam splitter (BS) and pinholes (PH) to split and select the optical beam (diffracted/undiffracted) order that will be feedback and detected simultaneously. The first beam component passes through a neutral density filter (NDF) and detected by SPIRICON* (CCD) beam profiler which is connected to a PC. The second component is feed back, through the analog output of a detector (D), to the feedback (FB) circuit. The feedback circuit output is then serve as the RF signal generator amplitude modulation (AM) external input. This will complete

the feedback loop required for this experiment. Photographs of the setup are shown in Figure 6.2.

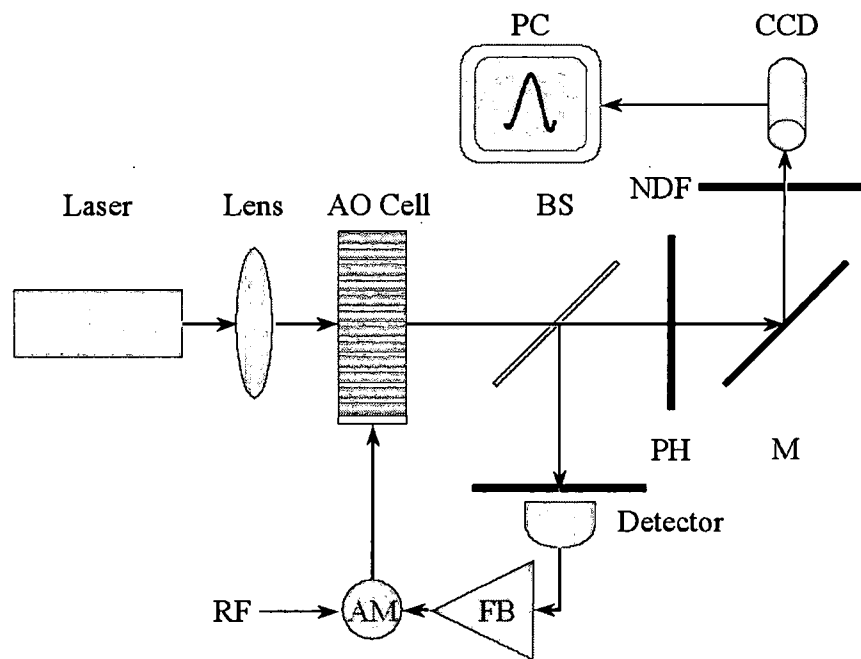
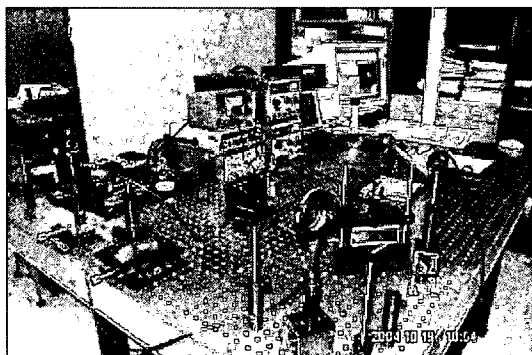


Figure 6.1 An illustration of the beam shaping experimental layout.



(a)



(b)

Figure 6.2 Experimental setup photographs, (a) a general view, and (b) a close up to the feedback circuit.

6.3 Feedback Circuit

In this section, a general overview of the feedback circuit is introduced. Furthermore, we elaborate on the circuit design choice explaining the advantages of such design.

6.3.1 Background

The analog output of the optical detector has been measured experimentally for our setup, and found to be 0.5 Volts. This voltage is required to be amplified, according to our simulation, to 9-15 Volts for the beam shaping effects to take place. Therefore, it is required to amplify such signal, with enough stability and accuracy, to the appropriate level to be feedback to the AM external input of the RF signal generator. The best candidate to perform this function is an operational amplifier (Op-Amp). A depiction of the Op-Amp is shown in Figure 6.3a. For small signal amplification with high precision and stability, especially in the sensing applications, we require the difference amplifier circuit shown in Figure 6.3a to have the following characteristics: extremely high (ideally infinite) common-mode and differential-mode input impedances; very low (ideally zero) output impedance; accurate and stable gain [123].

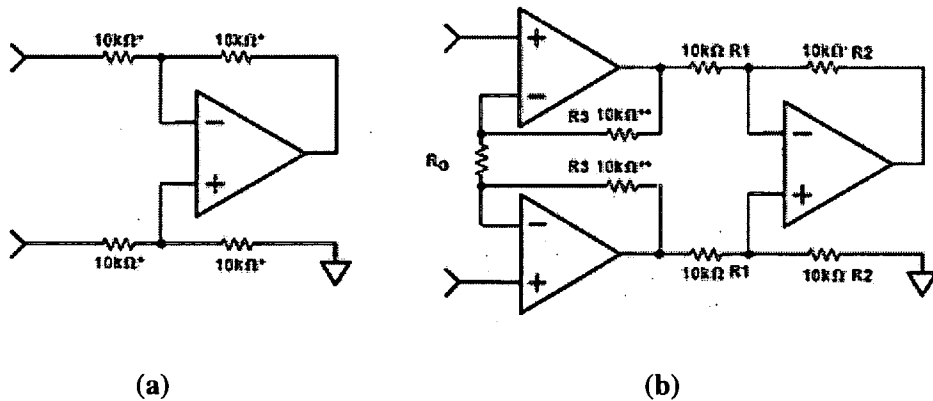


Figure 6.3 A depiction of (a) 1-stage difference amplifier, and (b) 3-stage difference amplifier.

Since both differential-mode and common-mode input resistances are finite, the circuit shown in Figure 6.3a fails to meet the high input impedance requirements. Consequently, it will load down the circuit supplying both input voltages. Furthermore, the common mode rejection ratio (CMRR) will be degraded. To overcome these drawbacks, the Op-Amp circuit is preceded with two high input impedance buffers as shown in Figure 6.3a, which is known as the Triple-Op-Amp Instrumentation Amplifier (IA) [123]. The total gain of the circuit shown in Figure 6.3b is:

$$A = \left(1 + 2 \frac{R_3}{R_G}\right) \times \left(\frac{R_2}{R_1}\right) = \left(1 + 2 \frac{R_3}{R_G}\right). \quad (6.1)$$

Since the two Op-Amps at the input stage operate in a non-inverting configuration, their closed loop input resistances are extremely high. Likewise, the closed loop output resistance of the Op-Amp at the output stage is quite low. The proper trimming of one of the second stage resistances can maximize the CMRR. Furthermore, the overall gain A can be accurately controlled by the external resistance ratios of R_3/R_G .

6.3.2 Circuit Used in Our Experiment

The above discussion lends itself to conclude that the Triple-Op-Amp IA design is an ideal candidate that should be used for our experiment. Such IA is available in Integrated Circuit (IC) form, where you can control the overall gain by changing the value of R_G only. The monolithic construction of the IC and laser wafer trimming allow for tight matching and tracking of circuit components, thus insuring the high level of performance inherent in this circuit. In addition, R_G also determines the transconductance of the preamp stage. This will have the advantage of; (a) reducing gain errors; (b) optimizing frequency response; (c) and reducing input noise. Furthermore, the simplicity and ability

to automate the gain changing process by incorporating computer control via automatic gain control (AGC) circuit is profound for the automation of the beam shaping process. This will be discussed in later chapter.

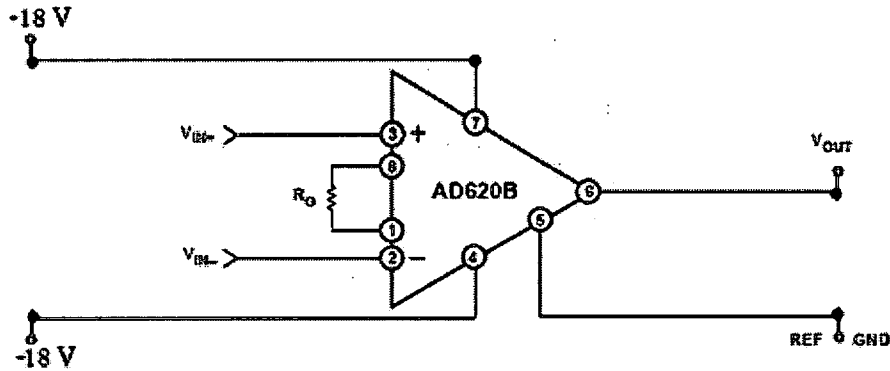


Figure 6.4 A simplified block diagram for the *AD620 IA* from Analog Devices. The gain is controlled only by R_G .

6.3.3 Our Feedback Circuit

We have used the *AD620 IA* from Analog Devices, that has a gain of up to 1000, as our feedback circuit for its simplicity, where controlling the gain is done only by changing R_G . The maximum output we can obtain is limited by the Op-Amp circuit power supply's value, i.e. $\pm 18V$. For this particular *IA*, the internal gain resistors R_3 are trimmed precisely to the value of $24.7K\Omega$. This means Equation (6.1) becomes

$$A = 1 + \frac{49.4K\Omega}{R_G}, \quad (6.2-a)$$

or

$$R_G = \frac{49.4K\Omega}{A-1}. \quad (6.2-b)$$

6.4. Experimental Results

6.4.1. Feedback Circuit Results

The following table shows the measured values of R_G and the corresponding feedback circuit output for an input voltage of 0.5 Volts. In addition, the final RMS values of the RF signal feeding the AO cell.

	R_G (K Ω)	Gain	$V_{out}(fdbk)$ Volts	V_{rms} Volts
1	1.2	40	2.59	8.6
2	1.5	34	2.95	8.38
3	1.8	28	3.53	7.69
4	2.2	23	3.84	8.08
5	2.7	19	4.16	7.73
6	3.3	16	4.95	8.12
7	3.9	14	5.79	8.94
8	4.7	12	6.92	9.78
9	5.6	10	8.07	10.67
10	6.8	8	9.42	11.35
11	7.5	8	11.77	11.76
12	8.2	7	14.25	12.09
13	10	6	16.98	13.44
14	12	5	17.14	13.49

Table 6.1 The gain values of the feedback circuit and the corresponding output voltage and RMS value of the RF signal. These values correspond to 0.5 V input signal to the feedback circuit.

As shown in the table, the V_{rms} values saturate for higher $V_{out}(fdbk)$ values.

6.4.2. Beam Shaping Results

In this section, we introduce the beam shaping experimental results. However, it is instructional to compare experimental and simulation results. Therefore, we first

introduce in Figure 6.5 the simulation results for various applied V_{rms} values as indicated.

We have used the same Matlab program as in the previous chapter.

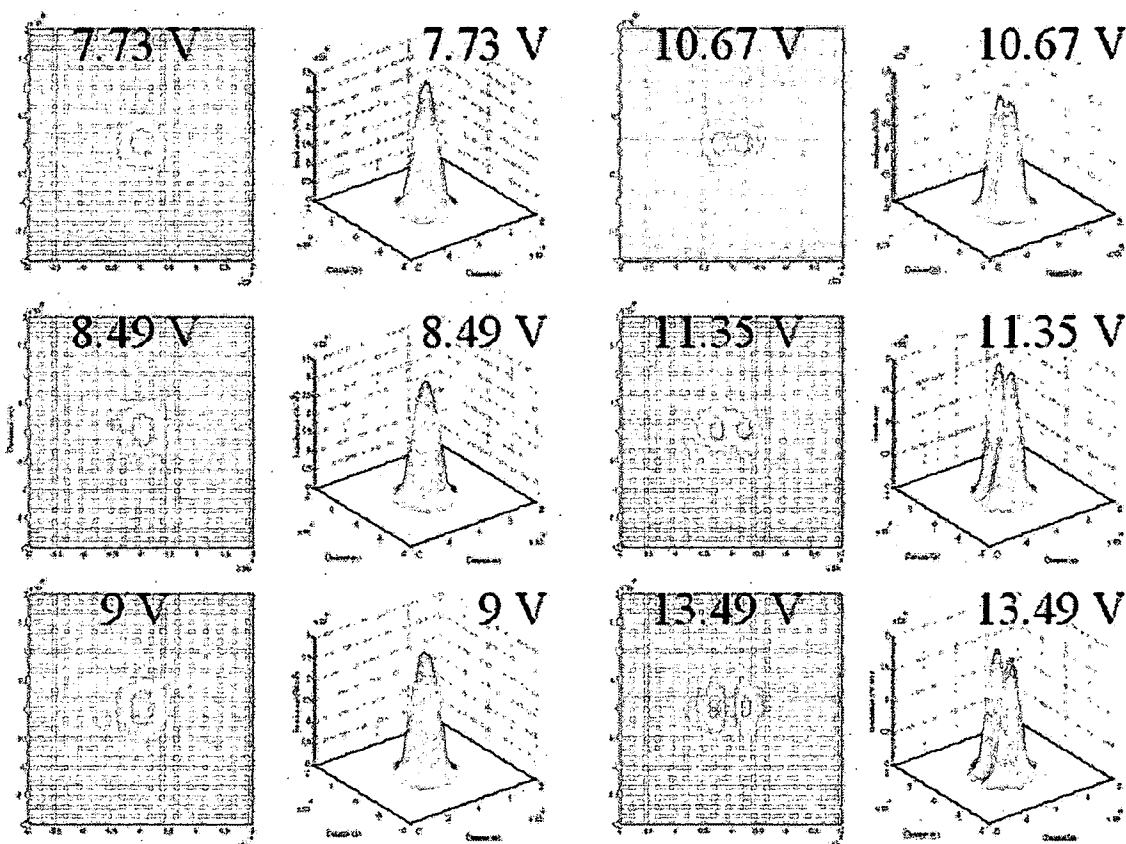


Figure 6.5 Simulated Optical beam shapes because of various V_{rms} values.

It can be seen from the Figure 6.5 that the beam shape evolution from Gaussian shape in x-y plane results in beam shaping in one direction, while in the other direction the shape remains Gaussian. This is very clear from Figure 6.6a, b, where a cross-section of the beam in the x and y directions, respectively, show that beam shaping is taking place in only the x-direction since the AO effect is only one dimensional. The results shown in Figure 6.5 are all for RF signal frequency of 50 MHz. It is very clear that a flattop beam is achieved at V_{rms} value of 9 Volts.

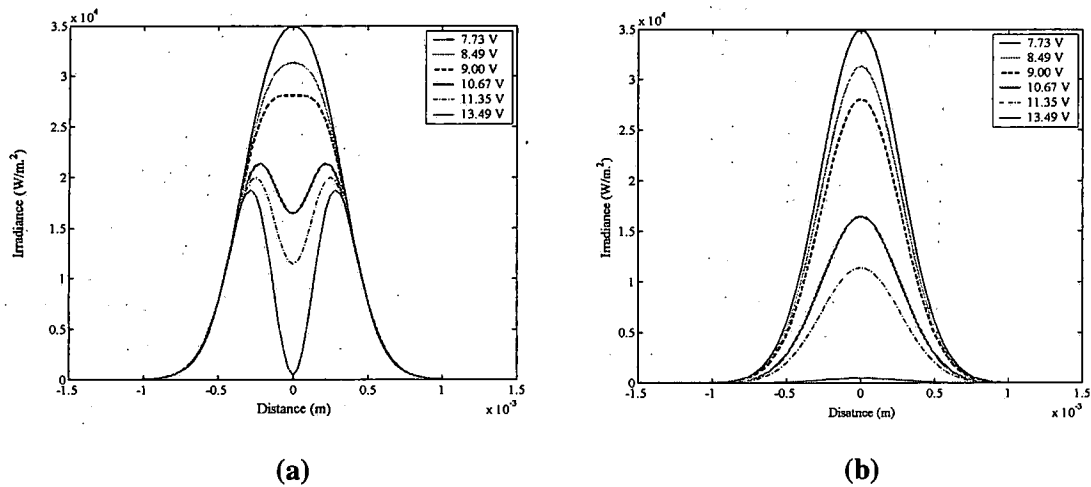


Figure 6.6 Cross sections of the optical beam showing the beam shaping effects are taking place only in (a) the x-direction, (b) while the Gaussian shape is preserved along the y-direction. Note that the amplitude of the beam in the y-direction is reduced as the total beam energy is reduced.

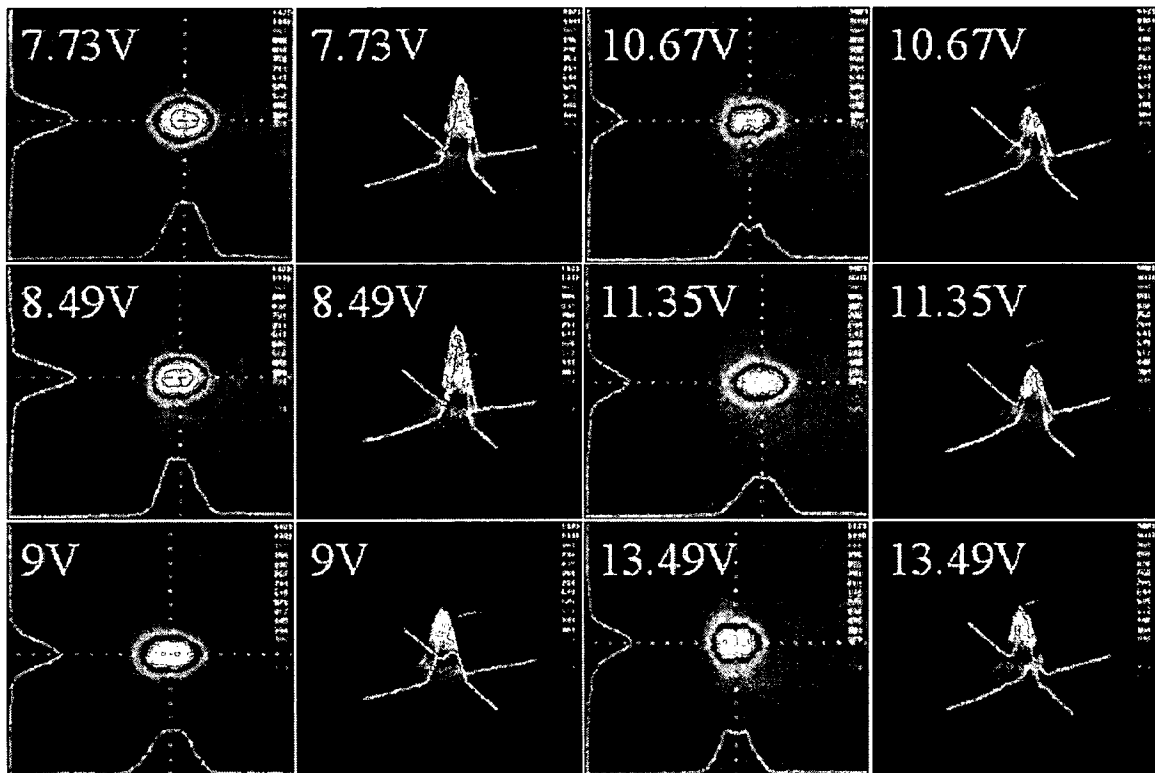


Figure 6.7 Snap shots of the experimental results using SPIRICON beam profiler. A quick comparison with Figure 5. indicates a similar beam shaping trend, however, at higher V_{rms} values, we do not achieve similar shape. We believe this is due to the alignment accuracy.

In Figure 6.7 the snap shots of the experimental results are shown at similar V_{rms} values. These photographs were obtained using SPIRICON beam profiler. It can be observed, comparing with Figure 6.5, a similar trend of beam shaping effects taking place. We notice the initial reduction in beam amplitude while preserving its Gaussian shape up to 8.49 V. At 9 V, we notice the beam elongation, in the x-direction only, to become a flattop. At a higher voltage, in addition to the amplitude reduction, we obtain a deeper cut in the on-axis amplitude. However, it does not go as far as the simulation show in Figure 6.5. We believe this is due to limitation in the alignment of our experimental setup.

It is very important to point out to the importance of the experimental setup alignment process. Since the optical beam diffraction is a function of the Bragg angle, it is crucial to have an accurate alignment for each RF signal frequency and amplitude. The setup is sensitive to the alignment, so that for every feedback value an adjustment of the beam incident angle is essential to observe optical beam shaping. Any misalignment can cause discrepancies between experimental results and theoretical simulation as indicated in Figures 6.5 and 6.7.

Chapter 7

Discussion and Conclusions

7.1 Summary

In Chapter 4 we have presented the preliminary simulation and experimental results of the electro-optic microlens fabrication and characterization. In addition, the experimental results of the adaptive beam shaping using hybrid AO device with electronic feedback was introduced in Chapter 6. In the following sections we will discuss the significance of such results and its correlation to the theoretical aspects developed in Chapters 2 and 5 respectively. Furthermore, some of the electro-optic microlens fabrication issues will be elaborated upon. Finally, we will outline future work to enhance the performance of various devices presented in this dissertation work.

7.2 Microlens Fabrication Process

The fabrication process of the PLZT microlens described in Chapter 3 is very simple, yet requires some careful considerations during the application. First, care must be taken during the mask design process. Since we have top and bottom electrodes for our devices, back-side alignment is required. Alignment marks were included to address global and local fields. This means that for mask aligners with 2" spacing in their field of view, global alignment marks were available. In addition, we made the same alignment marks around each die's field. All alignments marks were to

address various resolutions with line widths. It is essential to have good alignment since, as shown in Section 4.3.3, the electrode width and the inner electrode diameter affects the induced lens phase profile. Misaligned inner electrodes will result in further aberrations of the wave front.

The second most important step is wafer cleaning. Using standard Si wafer cleaning techniques is of great importance. By using the first two steps of the RCA cleaning process one will remove any organic materials and make the PLZT surface hydrophilic. It has been shown previously [125] that hydroxyl group (OH) will adhere onto the surface. This in turn will help during the subsequent ITO/Pt deposition inducing better electrode adhesion by forming an oxide layer at the electrode/substrate interface. Another cleaning process right after the lithography step and before the electrode sputtering was conducted using O₂ plasma treatment for 1 minute. This ashing process makes sure that any residual organic material left from the lithography process is cleared off.

The last step of the fabrication process is the electrode deposition. Previously we have used Cr/Au evaporated electrodes. Cr layer was evaporated as an adhesion promotion layer. However poor adhesion has prevented the realization of complete devices. It has been shown previously that the adhesion of evaporated thin film Cr to be function of the addition of oxygen to the deposition atmosphere [126]. These studies have shown that depending on the oxygen partial pressure, the evaporated Cr film undergo transition from a condition of low adhesion to one of high adhesion [126]. These studies suggest that increased adhesion is based on an oxide layer formation mechanism. Apart from the direct chemical interaction, a weak, second order contribution to the bonding process also comes from the mechanical locking at the interface [126]. It has been suggested that a

strong mechanical bonding occurs when the surface of the substrate is anatomically rough [126]. We have noticed difficult Cr adhesion for the wafer polished at the laboratory with 1~ 2 nm RMS surface roughness or better. The Cr adhesion problem would have been resolved by incorporating the O₂ to the evaporation chamber environment; however this was not available to us. Better adhesion have been achieved previously [68] for the sputtered ITO. We were able to achieve high quality 0.3–0.5 μm films with sheet resistance of 20 Ω/\square . However, due to ITO transparency, we have observed during the aperture effects study more complex diffraction pattern in the far field. This may be attributed not only to the inner and outer electrode edges, but also due to the induced phase modulation within the electrode width itself. Therefore blocking the light was important, hence using non-transparent layer, thus Platinum electrodes were used. Furthermore, it has been shown that the Pt/ITO electrodes will have better ohmic contacts [127].

In summary, hydroxylated PLZT surface due to base cleaning process, have better adhesion to ITO [125]. Furthermore the terminated surface of the ITO with hydrolyzed oxides of Indium and a Tin, including In(OH)₃ and InOOH, which form immediately after exposure to air contribute greatly to the better adhesion between Pt and ITO [128]. This gives in even better results if we anneal the electrodes after deposition to achieve the required resistivity of the ITO.

7.3 Microlens Characterization and Performance Optimization

The ability to tune lens characteristics is of great importance. The microlens array fabricated and characterized during the course of this work will be accepted for more applications if we are able not only tune the focal length, but also control its aberration.

7.3.1 Microlens Tuning Range

Upon close examination of Figure 4.16 we observe that at low applied voltages the measured focal length is much smaller than that of the simulated. Previously, PLZT piezoelectric properties have been investigated [129]. The piezoelectric coefficient has been reported to be 160 pC/N for 8/65/35 composition [129]. This may cause stresses within the PLZT 9/65/35 composition as well, which may cause more lensing effect. At higher voltages, i.e. above 300 V, we find that the FEMLAB and measured results are in good agreement. In general, scattering and depolarization effects [101] as well as the piezoelectric effects [129] were not included in our modeling.

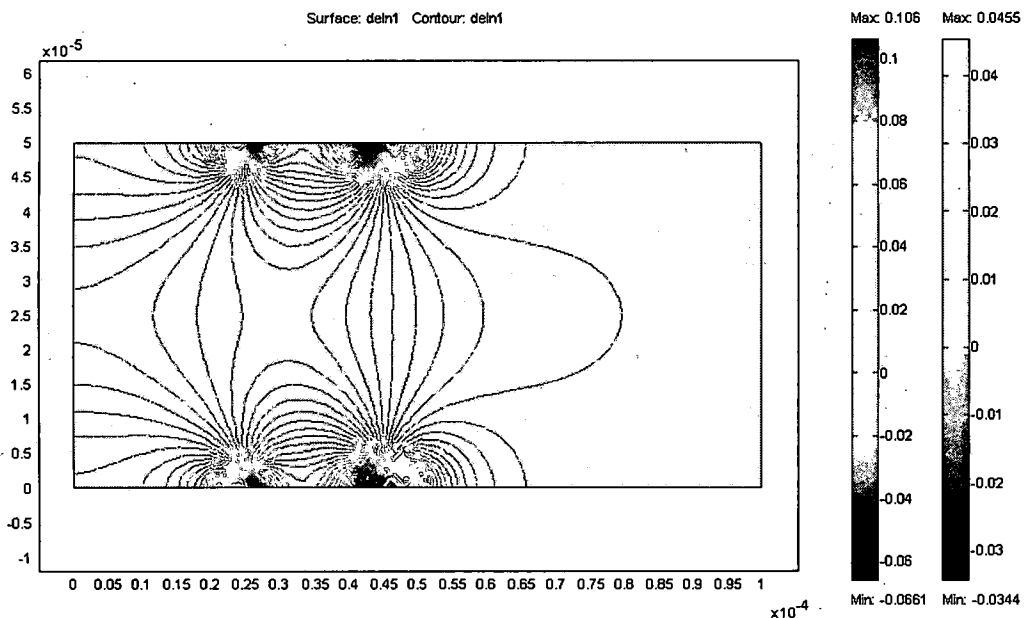


Figure 7.1 Surface and contour plots of the induced change in refractive index for x -polarization for PLZT substrate thickness of $50 \mu\text{m}$ and electrode width of $25 \mu\text{m}$. Note that the lens aperture diameter is $50 \mu\text{m}$, and the inner aperture size ratio w.r.t. electrode width is the same as the $500 \mu\text{m}$ diameter lens discussed in Chapter 6.

According to simulation and measurement results the focal length may vary from $3 \sim 80 \text{ cm}$. Higher voltages are required to achieve shorter focal lengths. Figure 7.1 shows the refractive index distribution within a $50 \mu\text{m}$ thick substrate that has surface

electrode width of $25\mu m$. Our calculations predict a minimum of $3.4mm$ focal length at 50V applications. This is an order of magnitude reduction in the applied voltage, and focal length. Although we may apply higher voltages to achieve yet smaller focal lengths, however, scattering and depolarization effects will take place at field above $1\times 10^6 V/m$ [130]. This will contribute to saturation in EO coefficient; hence the phase value will not incur more changes.

7.3.2 Electrode Design Optimization and Aberration Control

It has been shown previously that for aberration free PLZT microlens the inner electrode diameter to the substrate thickness ratio must be 1:1 [90]. We have chosen the same ratio for both simulated and fabricated devices. It was also shown that trapezoidal electrode shape will make the distortion in an optical beam wavefront almost negligible [131]. In Figure 7.2 surface and contour plots of the refractive index change, demonstrate two cases of trapezoidal and elliptical electrode shapes. Although trapezoidal electrode configuration can be achieved using RIE, nonetheless it is difficult the shape of the trench, since wafer orientation must be changed during the etching process inside the etching chamber. It should be much easier to achieve the semi-circular trenches using wet etching for PLZT, as described previously with well controlled parameters [132]. A summary of the errors in the phase, due to higher order terms in the quadratic fit of the phase data, is shown in Table 7.1. Notice that the error in the case of thinner substrates and smaller aperture is 1/3 of that larger one. Furthermore, the errors increase as the applied field increases. Hence, it is expected that smaller focal length lenses may show more phase errors. Finally, we found that the etched electrode provide shorter focal lengths of $2.4mm$, $2.5mm$ for elliptical and trapezoidal configurations respectively.

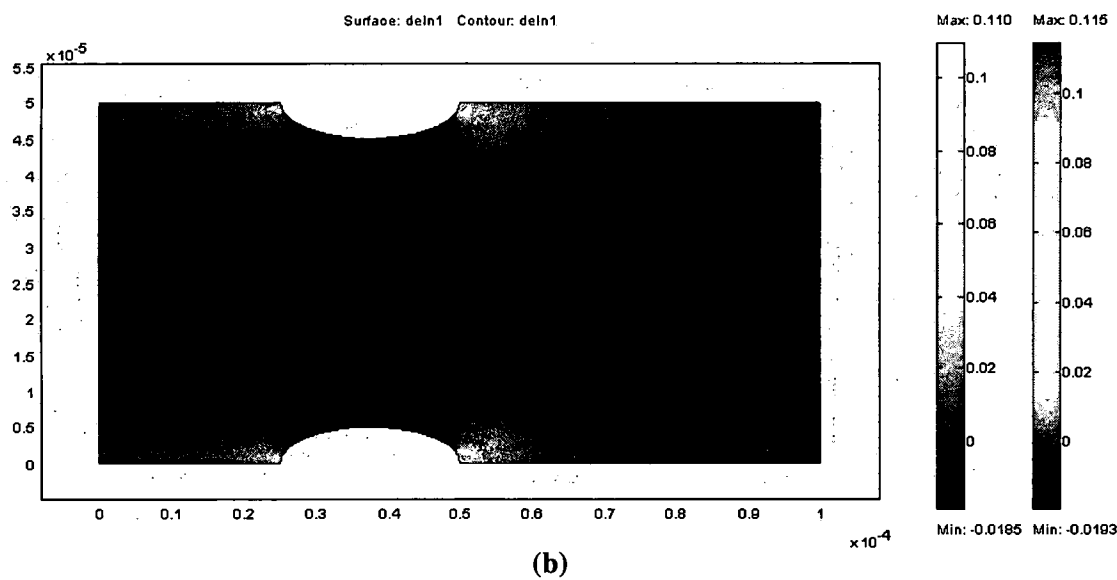
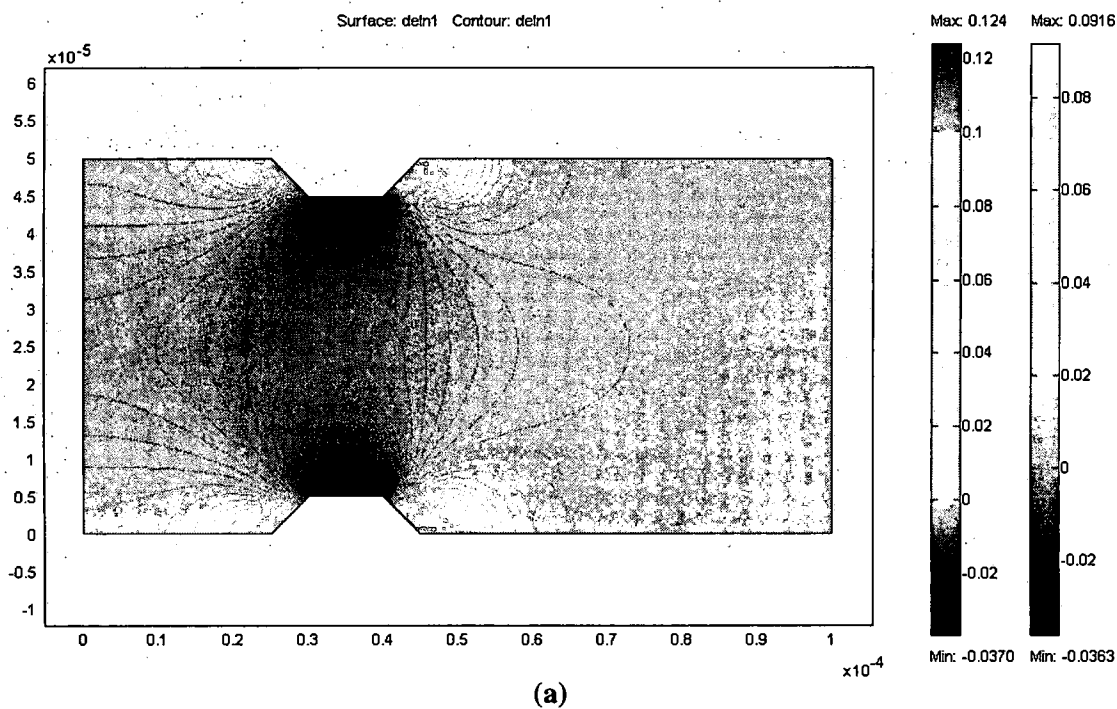


Figure 7.2 Surface and contour plots of the relative change of refractive index in the x-polarization for (a) Trapezoidal and (b) elliptical electrode configurations.

Electrostatic (V/m)	500 microns lens phase error~thick subst./Surf Electr.	50 microns lens phase error~thin subst./Surf. Electr.	50 microns lens phase error~thin subst./Ellip. Electr.	50 microns lens phase error~thin subst./Trapz Electr.
2.00E+05	0.022 π			
4.00E+05	0.045 π			
6.00E+05	0.07 π			
8.00E+05	0.092 π			
1.00E+06	0.115 π	0.045 π	0.041 π	0.041 π

Table 7.1 The calculated relative phase error in radians due to different electrode configurations and PLZT substrate thicknesses. Note that we kept the ratio between the electrode widths to lens aperture the same.

7.3 Future Work for PLZT-based Microlenses

Several aspects of the adaptive microlens characterization and fabrication need more investigations. First, the z-scan model should be extended to address the aberration issues. Furthermore, Equation 2.14 should be solved numerically so that full far-field 2-D diffraction evolution can be obtained. In addition, phase un-wrapping techniques should be used to extrapolate the microlens induced phase. Addition of such algorithm to the beam profiler software will prove to be handy. Once such numerical issues are resolved, addition modeling should be made with various electrode structure and substrate thickness. Since our resources were limited to fabricate more devices with various

electrode structures, this should be the topic of more research to verify our preceding discussions. Finally, spatial filters can be added, along with intentionally aberrated wavefronts and their effects on beam shaping should be addressed as well.

7.4 Hybrid AO Beam Shaping; Comments and Future Work

According to the ISO standards, the flatness and uniformity of an optical beam is defined as the flatness factor F , where

$$F = \frac{\text{AverageEnergy}}{\text{MaximumEnergy}}, \quad 0 < F < 1, \quad (7.1)$$

and the uniformity factor U , which is defined as

$$U = \frac{1}{E_{ave}} \sqrt{\frac{1}{A'_{ave}} \iint (E(x, y) - E_{ave})^2 dx dy} . \quad (7.2)$$

Where A'_{ave} is the average beam amplitude. The above expressions represent the basis upon which the SPIRICON laser beam profiler is operating to determine how flat-top is a Gaussian beam. This is clearly a 2-D treatment of the problem. To fully characterize the efficiency by which AO cell, one must solve the problem in 2-D. This will require 2 AO cells in tandem to process light beam in the x and y directions. This is currently under development, where the 2-D problem will be extended in our simulation software. In addition, the calculation of the terms F and U will be incorporated as well.

Several improvements can be added to our experimental setup. First a computer control feedback circuit can be devised. Second, since the AO cell/light interaction is very sensitive to the incident angle, the alignment process should be automated.

Ultimately, a data acquisition system should be in control of the entire process where LABVIEW program can remotely control and monitor the beam shaping process. This can be achieved by processing the “shaped beam” signal through the SPIRICON beam

profiler and calculating the factors F and U . These values will be compared against ideal values. In the mean time and based on the processed data, the beam profiler can automatically trigger the feedback circuit to change its value such that a variation of the F and U factors is attained for optimization of our goal. Furthermore, the automatic alignment process should also be part of the feedback process so that the incident angle should be accurate enough to maximize the flatness and uniformity of the beam.

Finally, another area of future development is the selection of some of the spatial components of the optical beam and feeding it back to the AO cell, thereby providing optical feedback. This process may benefit the final beam shape by selectively shaping portions of the optical beam.

Appendix A

In the following sections we introduce the programs used to simulate various problems associated with this dissertation work. All programs were developed using MATLAB code.

A.1 Beam Shaping Using Zero-order Feedback

This program simulate the hybrid AO beam shaping problem based on Figures 3.4, and 3.5, which have been detailed more in Figure 4.1. The main issue to point out for this program is that in the feedback loop we have utilized the detected 0th –order beam to modulate the amplitude of RF signal, hence changing the values of the peak phase delay α_0 as explained in Section 3.5.

```
% #####  
% This program studies the effect of feedback on the AO Beam Shaping.  
% The feedback process is implemented by taking the detected power of the  
% 0th-order beam and feeding it back unto the AO cell.  
% #####  
  
clear all  
N=128 ;  
x1 = 10.^-3.*[-2:4./(N):2] ; % Non-normalized distance  
x2 = 10.^-3.*[-2:4./(N):2] ;  
ng = 1.54 ; % glass refractive index  
zL = 1 ; % Far field distance where the detector lies (m)  
  
% #####  
% For the incident beam power "P" of 10 mW, we can determine the electric  
% field which is equal to E=sqrt(P*R/A), R is the c/c impedance (377 ohm),  
% A is beam cross-sectional area.  
% #####  
y0 = 0.632*10^-6 ; % Light wave length (m)
```

```

w0 = 75*10^-6 ; % beam width (m)
p = 10*10^-3 ; % beam power (w)
k0 = 2*pi/y0 ; % original beam spatial frequency
A0 = pi*(w0/2).^2 ; % beam area (m^2)
E = sqrt((p*377)/A0) ; % electric field amplitude V/m
R = 0.01 ; % detector responsivity (A/W)
Vrms = 7 ; % [7,8.26,9.36] ; % generated AO voltage
R1 = 1000 ; % resistance (ohm)
L1 = 0.05 ; % AO interaction length (m)
v0 = 3.96*10^3 ; % Speed of sound (m/s)
delz2 = 2*zL/k0 ;
F = (50)*10^6 ; % Sound frequency (Hz)
y1 = v0/F ; % Sound wavelength (m)
k1 = 2*pi./(1.*y1) ; % Sound spatial frequency
const = 0.005135*pi ; % Measured constant (rad/V.^2)
Qp = k1^2*L1/(1*k0) ; % The Klein-Cook parameter
y = E*(exp(-(x1.*x1)./(w0.^2)))*(exp(-(x2.*x2)./(w0.^2))) ; % optical Field

energy1=sum(sum(abs(y.^2))) % Units of V^2/m^2

yIrr = (1./(((1.5064437).^2)*377)).*abs(y.^2) ; % Irradiance of the original beam as
% seem from the source (W/m^2)

yIrr = (1./(((3.0080).^2)*377)).*abs(y.^2) ;
pwrCheck1 = sum(sum(yIrr))*A0;

u1 = 3*10^4*[-2:4/(N):2] ; % Spatial Frequency Range (1/m)
u2 = 3*10^4*[-2:4/(N):2] ; % coressponding to Fourier
% Transform of the Gaussian Beam

z1 = (fft2(y)) ; % Fourier Transform of the beam at the
% AO cell entrance
z1=fftshift(z1) ;

delz = 1.632888377176588e-009; % Equals (L/2k0), where L is the AO interaction
% length (about 5cm) and k0 is the saptial frequency
% for the incident beam (2pi/0.632 microns)

v = (exp(i*u1.*u1*delz))*(exp(i*u2.*u2*delz)) ; % v is the AO transfer function of
%propagation
alpha0 = const*(Vrms)^2 ; % Initial peak phase delay
x = sqrt((Qp.*u1.*y1./(4*pi)).^2+(alpha0/2).*(alpha0/2)) ;

% 2-D AO transfer function w/ 1-D Diffraction Grating Effect,
% the second dimension contains only the transfer function of
% propagation

```

```

vao0=
(i*(exp(i*u1.*u1*delz)).*(Qp.*u1.*y1./(4*pi)).*sin(x)./x+(exp(i*u1.*u1*delz)).*(cos(x))
)*(exp(i*u2.*u2*delz)) ;

zp0 = z1.*vao0 ;           % output beam (Zero order AO transfer function)
                             % at the detection point without feedback

xw=u1.*zL./k0 ; % Far field distance
TF = (exp(i*u1.*u1*zL./2*k0 ))*(exp(i*u2.*u2*zL./2*k0 )) ; % Free space propagation
%function
TF = fftshift(TF) ;        % Aligned Propagation Transfer function
ZFF0 = zp0.*TF ;          % Beam at the detector (Spatial Frequency Domain)

ZFF0 = fftshift(ZFF0) ;
Z0ff = (ifftshift(ZFF0)) ; % Actual Beam shape at the Detector

wb=2.68*10.^-3 ; % 2*beam width in the far field (m)
delx1=wb/(N+1) ; % Discrete spacing values
Ints0 = (1./(377*((N+1)^2))).*sum(sum(abs(Z0ff.^2))) ; % Detected Intensity (w/m^2)
PowerDet0 = (1./(377*((N+1).^2))).*sum(sum(abs(Z0ff.^2))).*(delx1.^2) ; % detected
%power in 2-D (watt)
Vgen0 = PowerDet0*R*R1 ; % Vgen=DC value at the detector (Volts). i/p of the
%fdbk circuit
beta0 = 2*const*Vgen0*R1*1*R*(delx1).^2 ; %Feedback factor
deltalpha0 = beta0*Ints0 ; % The change in the peak phase delay due to fdbk

% #####
% The following is the feedback loop
% #####

ii=0 ;
for G = 75*[-2:4/(N):2] ; % OpAmp circuit gain
    ii = ii+1 ;
    for k = 1:30;
        Vfdbk0 = G*Vgen0
        deltalpahaFB0 = 2*const*Vrms*Vfdbk0+const*Vfdbk0.^2;
        alphan = alpha0+ deltalpahaFB0;
        x = sqrt((Qp.*u1.*y1./(4*pi)).^2+(alphan/2).*(alphan/2)) ;
        % 2-D AO transfer function w/ 1-D Diffraction Grating Effect,
        % the second dimension contains only the transfer function of
        % propagation
        v1D=exp(i*u1.*u1*delz);
        vao1DFB = i.*v1D.*(Qp.*u1.*y1./(4*pi)).*sin(x)./x+v1D.*(cos(x));
        vao1DFBmat(ii,:) = vao1DFB ;
    end
end

```

```

vaoFB0 =
(i*(exp(i*u1.*u1*delz)).*(Qp.*u1.*y1./(4*pi)).*sin(x)./x+(exp(i*u1.*u1*delz)).*(cos(x))
)'.*(exp(i*u2.*u2*delz));

```

```

zpFB0 = z1.*vaoFB0 ;    % output beam (Zero order AO transfer function)
                        % at the detection point without feedback

```

```

xw=u1.*zL./k0 ;    % Far field distance
TF = (exp(i*u1.*u1*zL./2*k0 ))*(exp(i*u2.*u2*zL./2*k0 )) ;% Free space
%propagation function
TF = fftshift(TF) ;           % Aligned Propagation Transfer function
ZFF0 = zpFB0.*TF ;           % Beam at the detector (Spatial Frequency Domain)
ZFF0 = fftshift(ZFF0) ;
ZOff = (ifftshift(ZFF0)) ;    % Actual Beam shape at the Detector
BeamShpd = ((1/(377*((N+1).^2))).*abs(ZOff(65,:).^2)) ;
BeamNorm = ((1/(377*((N+1).^2))).*abs(ZOff(:,65).^2));
wb=2.86*10.^-3 ;            % 2*beam width in the far field (m)
delx1=wb/(N+1) ;           % Discrete spacing values
IntsFB0 = (1./(377*((N+1).^2))).*sum(sum(abs(ZOff.^2))) ; % Detected Intensity
%(w/m^2)
PowerDetFB0 = (1./(377*((N+1).^2))).*sum(sum(abs(ZOff.^2))).*(delx1.^2) ; %
%detected power in 2-D (watt)
VgenFB0 = PowerDetFB0*R*R1 ;    % Vgen=DC value at the detector (Volts). i/p of
% the fdbk circuit
betaFB0 = 2*const*VgenFB0*R1*1*R*(delx1).^2 ; %Feedback factor

```

```

%#####

```

```

% Coverage Loop

```

```

%#####

```

```

if (abs(VgenFB0-Vgen0)/Vgen0)<1e-2
    Vfdbk0 = G*VgenFB0
    kout=k;
    koutMat(ii,:) = kout;
    Gout = G;
    GoutMat(ii,:) = Gout;
    alphanconv = alphan;
    alphanconvMat(ii,:) = alphanconv;
    break
end
Vgen0 = VgenFB0;
end
BeamShpdmat(ii,:) =BeamShpd ;
BeamNormmat(:,ii) = BeamNorm ;
VgenFB0mat(ii,:) = VgenFB0 ;
PowerDetFB0mat(ii,:) = PowerDetFB0 ;

```

```

        deltaPhiFB0mat(ii,:) = deltaPhiFB0 ;
        alphaPhiMat(ii,:) = alphaPhi ;
        Vfdbk0mat(ii,:) = Vfdbk0 ;
    end
end

```

A.2 Beam Shaping Using First-order Feedback

This program simulates the hybrid AO beam shaping problem based on Figures 3.4, and 3.5, which have been detailed more in Figure 4.1. The only distinction between this program and the one introduced in the previous section is that in the feedback loop we utilize the detected diffracted 1st-order to modulate the peak phase delay α_0 as explained in Section 3.5. Observation of the adaptive beam shaping is done for the 0th-order.

```

% #####
% This program studies the effect of feedback on the AO Beam Shaping.
% The feedback process is implemented by taking the detected component of the
% diffracted 1st-order beam and feeding it back into the AO cell.
% #####

clear all
N = 128 ;
% G = 50 ;                % Operational Amplifier Circuit Gain
x1 = 10^-3.*[-2:4./(N):2] ; % Non-normalized distance
x2 = 10^-3.*[-2:4./(N):2] ;
ng = 1.54 ;                % glass refractive index
zL = 1 ;                   % Far field distance where the detector lies (m)

% #####
% For the incident beam power "P" of 10 mW, we can determine the electric
% field which is equal to E=sqrt(P*R/A), R is the c/c impedance (377 ohm),
% A is beam cross-sectional area.
% #####

y0 = 0.632*10^-6 ;          % Light wave length (m)
w0 = 75*10^-6 ;             % beam width (m)
p = 10*10^-3 ;              % beam power (w)
k0 = 2*pi/y0 ;              % original beam spatial frequency
A0 = pi*(w0/2).^2 ;         % beam area (m^2)
E = sqrt((p*377)/A0) ;      % electric field amplitude V/m

```

```

R = 0.01 ; % detector responsivity (A/W)
Vrms = 7; % [7,8.26,9.36] ; % generated AO voltage
R1 = 1000 ; % resistance (ohm)
L1 = 0.05 ; % AO interaction length (m)
v0 = 3.96*10^3 ; % Speed of sound (m/s)
delz2 = 2*zL/k0 ;
F = (50)*10^6 ; % Sound frequency (Hz)
y1 = v0/F ; % Sound wavelength (m)
k1 = 2*pi./(1.*y1) ; % Sound spatial frequency
const = 0.005135*pi ; % Measured constant (rad/V.^2)
Qp = k1^2*L1/(1*k0) ; % The Klein-Cook parameter
y = E*(exp(-(x1.*x1)./(w0.^2)))*(exp(-(x2.*x2)./(w0.^2))) ; % optical Field

yIrr = (1./(((3.0080).^2)*377)).*abs(y.^2) ; % Irradiance of the original beam as
% seem from the source (W/m^2)
u1 = 3*10^4*[-2:4/(N):2] ; % Spatial Frequency Range (1/m)
u2 = 3*10^4*[-2:4/(N):2] ; % coressponding to Fourier
% Transform of the Gaussian Beam

z1 = (fft2(y)) ; % Fourier Transform of the beam at the
% AO cell entrance
z1=fftshift(z1) ;
% energy2 = sum(sum(abs(z1.^2))) % If divided by (65^2) will give exact number as
line 37

delz = 1.632888377176588e-009; % Equals (L/2*ng*k0), where L is the AO
%interaction
% length (about 5cm) and k0 is the spatial frequency for the incident beam (2pi/0.632
%microns)
v = (exp(i*u1.*u1*delz))*(exp(i*u2.*u2*delz)) ; % v is the AO transfer function of
propagation
alpha0 = const*(Vrms)^2 ; % Initial peak phase delay
x = sqrt((Qp.*u1.*y1/(4*pi)).^2+(alpha0/2).*(alpha0/2)) ;

% #####
% 2-D AO transfer function w/ 1-D Diffraction Grating Effect, the second dimension
%contains only the transfer function of propagation
%#####

vao1=(i*(exp(i*u1.*u1*delz)).*(alpha0/2).sin(x)./x)*(exp(i*u2.*u2*delz)); % AO 1st
%order transfer function

zpl=z1.*vao1; % 1st order diffracted beam just
% before the detector without feedback

xw=u1.*zL./k0 ; % Far field distance

```



```

TF = (exp(i*u1.*u1*zL./2*k0 ))*(exp(i*u2.*u2*zL./2*k0 )) ;% Free space propagation
%function
TF = fftshift(TF) ;           % Aligned Propagation Transfer function
ZFF1 = zp1.*TF ;
ZFF1 = fftshift(ZFF1) ;
Z1ff = (ifftshift(ZFF1)) ;   % Actual Beam shape at the Detector

wb=2.68*10.^-3 ;           % 2*beam width in the far field (m)
delx1=wb/(N+1) ;           % Discrete spacing values
Ints1 = (1./(377*((N+1)^2))).*sum(sum(abs(Z1ff.^2))) ; % Detected Intensity (w/m^2)
PowerDet1 = (1./(377*((N+1).^2))).*sum(sum(abs(Z1ff.^2))).*(delx1.^2) ; % detected
%power in 2-D (watt)
Vgen1 = PowerDet1*R*R1 ;    % Vgen=DC value at the detector (Volts). i/p of the
%fdbk circuit
beta1 = 2*const*Vgen1*R1*1*R*(delx1).^2 ; %Feedback factor
deltapha1 = beta1*Ints1 ; % The change in the peak phase delay due to fdbk
% #####
% The following is the feedback loop
% #####

ii=0 ;
for G = 75*[-2:4/(N):2] ;    % OpAmp circuit gain
    ii = ii+1 ;
    for k = 1:500 ;
        Vfdbk1 = G*Vgen1 ;
        deltaxFB1 = 2*const*Vrms*Vfdbk1+const*Vfdbk1.^2
        alphan1 = alpha0+ deltaxFB1 ;
        x = sqrt((Qp.*u1.*y1./(4*pi)).^2+(alphan1/2).*(alphan1/2)) ;

        % #####
        % 2-D AO transfer function w/ 1-D Diffraction Grating Effect, the
        % second dimension contains only the transfer function of propagation
        % #####

        v1D=exp(i*u1.*u1*delz);
        vao11DFB = i*v1D.*(alphan1/2).*sin(x)./x;
        vao11DFBmat(ii,:) = vao11DFB ;

        vao1FB=(i*(exp(i*u1.*u1*delz)).*(alphan1/2).*sin(x)./x)*(exp(i*u2.*u2*delz));
% AO 1st order transfer function
        zp1FB=z1.*vao1FB; % 1st order diffracted beam just before the detector without
%feedback
        xw=u1.*zL./k0 ; % Far field distance
        TF = (exp(i*u1.*u1*zL./2*k0 ))*(exp(i*u2.*u2*zL./2*k0 )) ;% Free space
%propagation function
        TF = fftshift(TF) ;           % Aligned Propagation Transfer function

```

```

ZFF1 = zp1FB.*TF ;           % Beam at the detector (Spatial Frequency Domain)
energy4 = sum(sum(abs(ZFF1.^2)));
ZFF1 = fftshift(ZFF1) ;
Z1ff = (ifftshift(ZFF1)) ;   % Actual Beam shape at the Detector
wb=2.86*10.^-3 ;           % 2*beam width in the far field (m)
delx1=wb/(N+1) ;           % Discrete spacing values
IntsFB1 = (1./(377*((N+1).^2)).*sum(sum(abs(Z1ff.^2))) ; % Detected Intensity
% (w/m^2)
PowerDetFB1 = (1./(377*((N+1).^2)).*sum(sum(abs(Z1ff.^2))).*(delx1.^2) ; %
%detected power in 2-D (watt)
VgenFB1 = PowerDetFB1*R*R1 ;   % Vgen=DC value at the detector (Volts).
%i/p of the fdbk circuit
VgenFB1mat(ii,:) = VgenFB1 ;
PowerDetFB1mat(ii,:) = PowerDetFB1 ;
deltalphaFB1mat(ii,:) = deltalphaFB1 ;
alphan1mat(ii,:) = alphan1 ;
Vfdbk1mat(ii,:) = Vfdbk1 ;
betaFB1 = 2*const*VgenFB1*R1*1*R*(delx1).^2 ; %Feedback factor
if (abs(VgenFB1-Vgen1)/Vgen1)<1e-6
    kout=k
    koutMat(ii,:) = kout;
    Gout = G;
    GoutMat(ii,:) = Gout;
    alphanconv = alphan1;
    x = sqrt((Qp.*u1.*y1./(4*pi)).^2+(alphanconv/2).*(alphanconv/2)) ;
    v1D=exp(i*u1.*u1*delz);
    vao11DFB = i*v1D.*(alphan1/2).*sin(x)./x;
    vao11DFBmat(ii,:) = vao11DFB ;

vao1FB=(i*(exp(i*u1.*u1*delz)).*(alphan1/2).*sin(x)./x)*(exp(i*u2.*u2*delz)); % AO
%1st order transfer function
zp1FB=z1.*vao1FB; % 1st order diffracted beam just before the detector
%without feedback
xw=u1.*zL./k0 ; % Far field distance
TF = (exp(i*u1.*u1*zL./2*k0 ))*(exp(i*u2.*u2*zL./2*k0 )) ; % Free space
%propagation function
TF = fftshift(TF) ;           % Aligned Propagation Transfer function
ZFF1 = zp1FB.*TF ;           % Beam at the detector (Spatial Frequency
%Domain)
energy4 = sum(sum(abs(ZFF1.^2)));
ZFF1 = fftshift(ZFF1) ;
Z1ff = (ifftshift(ZFF1)) ;   % Actual Beam shape at the Detector
wb=2.86*10.^-3 ;           % 2*beam width in the far field (m)
delx1=wb/(N+1) ;           % Discrete spacing values
IntsFB1 = (1./(377*((N+1).^2)).*sum(sum(abs(Z1ff.^2))) ; % Detected
%Intensity (w/m^2)

```

```

        PowerDetFB1 = (1./(377*((N+1).^2))).*sum(sum(abs(Z1ff.^2))).*(delx1.^2) ; %
%detected power in 2-D (watt)
        VgenFB1 = PowerDetFB1*R*R1 ;    % Vgen=DC value at the detector
%(Volts). i/p of the fdbk circuit
        VgenFB1mat(ii,:) = VgenFB1 ;
        PowerDetFB1mat(ii,:) = PowerDetFB1 ;
        deltalpFB1mat(ii,:) = deltalpFB1 ;
        alphan1mat(ii,:) = alphan1 ;
        Vfdbk1mat(ii,:) = Vfdbk1 ;
        betaFB1 = 2*const*VgenFB1*R1*1*R*(delx1).^2 ; %Feedback factor
    break
    end
    Vgen1 = VgenFB1;
end
% alphanconvMat(ii,:) = alphanconv/pi;
vaoFB0 =
(i*(exp(i*u1.*u1*delz)).*(Qp.*u1.*y1./(4*pi)).*sin(x)./x+(exp(i*u1.*u1*delz)).*(cos(x))
)*exp(i*u2.*u2*delz)) ;
zpFB0 = z1.*vaoFB0 ;    % output beam (Zero order AO transfer function) at the
%detection point without feedback
TF = (exp(i*u1.*u1*zL./2*k0 ))*(exp(i*u2.*u2*zL./2*k0 )) ; % Free space
%propagation function
TF = fftshift(TF) ;    % Aligned Propagation Transfer function
ZFF0 = zpFB0.*TF ;    % Beam at the detector (Spatial Frequency Domain)
ZFF0 = fftshift(ZFF0) ;
Z0ff = (ifftshift(ZFF0)) ;    % Actual Beam shape at the Detector

figure(12), plot(x1, (1/(377*((N+1).^2))).*abs(Z0ff(:,65).^2)) ; % units(W/m^2)
xlim([-1.5*10^-3 1.5*10^-3])
hold on
BeamShpd = ((1/(377*((N+1).^2))).*abs(Z0ff(65,:).^2)) ;
BeamNorm = ((1/(377*((N+1).^2))).*abs(Z0ff(:,65).^2));
BeamShpdmat(ii,:) = BeamShpd ;
BeamNormmat(:,ii) = BeamNorm ;
wb=2.86*10.^-3 ;    % 2*beam width in the far field (m)
delx1=wb/(N+1) ;    % Discrete spacing values
IntsFB0 = (1./(377*((N+1).^2))).*sum(sum(abs(Z0ff.^2))) ; % Detected Intensity
%(w/m^2)
PowerDetFB0 = (1./(377*((N+1).^2))).*sum(sum(abs(Z0ff.^2))).*(delx1.^2) ; %
%detected power in 2-D (watt)
PowerDetFB0mat(ii,:) = PowerDetFB0 ;
PowerDetFB0matNORM = PowerDetFB0mat/p;
end
end

```

A.3. Z-Scan Program

The program developed in this section is based on the theory developed in Section 2.6.2.

The main objective is to plot the on-axis intensity variations as a function of the scanned distance Δz , for various focal length lenses. This is then followed by monitoring the slope of the intensity plot at $\Delta z = 0$. First, we calculate the on-axis intensity based on Equation 2.22. Then we calculate the slope of the resulting data.

```
clear all
format short e
L1=0.6328*10^-6; % Wavelength
k0=2*pi/L1; % Wave number
for w0=[20].*10^-6; % beam waist at the focus of the external lens
    r0=500*10^-6; % Microlens aperture
    L=550*10^-3; % observation distance
    fvalues=0.001*[1:49./512:50]; % Assumed focal lengths variation
    for n = 1:length(fvalues)
        ftest = fvalues(n);
        fprintf('focus %g %d \n',ftest,n);
        x(n) = ftest;
        p0=(k0.*w0.^2)./2; % Confocal parameter (Raleigh length)
        q0=j.*p0;
        delz=9.5*[-p0/2.*p0./512:p0]; % Scanning increments

%#####
% The following lines for calculation of the expression of Equation 2.22
%#####

        qL=(L.*ftest.*(q0+delz))./(L.*ftest+ftest.*(q0+delz)-L.*(q0+delz));
        x1=-(j.*k0)./(2.*pi.*L.*ftest);
        x2=q0./(q0+delz);
        xr=real(qL);
        xi=imag(qL);
        x4=cos((k0.*r0.^2.*xr)./(2.*abs(qL.^2)));
        xphs=(k0.*r0.^2.*xr)./(2.*abs(qL.^2));
        x7=exp(-(k0.*r0.^2.*xi)./(2.*abs(qL.^2)));
        x8=exp(-(k0.*r0.^2.*xi)./abs(qL.^2));
        xL=abs(x1.^2).*abs(x2.^2).*abs(qL.^2);
        Iff2 = xL.*(1+x8-2.*x7.*x4); % Equation 2.22
        Iff2mat(n,:)=Iff2;
        D=convn(Iff2,[1 0 -1],'same')./convn(delz,[1 0 -1],'same'); % On-axis slope at
%delz=0
```

```
D(1)=(Iff2(2)-Iff2(1))/(delz(2)-delz(1)); % slope at the starting data point
D(513)=(Iff2(513)-Iff2(512))/(delz(513)-delz(512)); slope at the end data point
y(n) = D(257)/max(abs(D)); % slope normalization
end
end
```

Bibliography

1. F. M. Dickey, S. C. Holswade, "Laser beam shaping; Theory and techniques" Optical Engineering Series, Marcel Dekker, Chapter 1, (2000).
2. F. M. Dickey, "Laser beam shaping" Optics and Photonics News, 30-35, April (2003).
3. J.-L. Ocana, A. Garcia-Beltrán, F. Laguarda, J. Armengol, N. Lupón, and F. Vega, "Laser heat treatments driven by integrated beams: role of irradiation uniformities", Applied Optics, **38**, 4570-4576 (1999).
4. E. Forsén, P. Carlberg, L. Montelius, A. Boisen, "Laser lithography on resist bi-layer for nanomelectromecahnical system prototyping", Microelectronics Engineering, **73-74**, 491-495 (2004).
5. M. Dunbar and K. Sager, "A novel, media-compatible pressure sensor for automotive applications, Sensor Magazine, **17**, (2000).
6. N. Streibl, U. Nölscher, J. Jahns,a and S. Walker, "Array generation with lenslet array", Applied Optics, **30**, 2739-2742 (1991).
7. S. Heinemann, "Computer generated beam shaping and focusing optical elements for laser materials processing", Optics Communications, **119**, 613-622 (1995).
8. A. Schilling, H. P. Hertzog, L. Stauffer, U. Vokinger, and M. Rossi, "Efficient beam shaping of linear, high power diode laser by use of microoptics", Applied Optics, **40**, 5852-5858 (2001).
9. R. Hild, J.C. Escalera, M.J. Yzuel, and G. Nitzsche, "High focal depth beam shaping elements", Microelectronics Engineering, **35**, 205-208 (1997).
10. R.L. Aagrað, "Methods for optimizing the beam shape in a focused coherent optical system", Applied Optics, **13**, 1633-1638 (1974).
11. W.W. Simmons, G.W. Leppelmeier and B.C. Johnson, "Optical beam shaping using polarization effects", Applied Optics, **13**, 1629-1632 (1997).
12. W.B. Veldkamp, "Overview of microoptics: Past, present, and future", Miniature and Micro-Optics, SPIE Proceedings, **1544**, (1991).
13. K. Peterson, "Silicon as a mechanical material", IEEE Proceedings, **70**, 420-448 (1982).
14. M. Huff, "MEMS Fabrication", Sensor Review, **22**, 18-33 (2002).
15. I.B. Heard, R. Coquillé, D. Rivière, P.-Y. Klimonda, "Characterization and reliability of a switch matrix based on MOEMS technology", Microelectronics' Reliability, **43**, 1935-1937 (2003).
16. S. Sinzinger and J. Jahns, "Microoptics", Wiley-VCH Verlag, (1999).
17. Y. Huang, E.L. Mather, J.L. Bell, M. Madou, "MEMS-based sample separation for molecular diagnostics", Journal Bioanalytical Chemistry, **372**, 49-65 (2002).

18. U. Staufer, T. Akiyama, C. Beuret, S. Gautsch, W. Noell, G. Schurmann, C. Stebler_ and N.F. de Rooij, "Micro-electromechanical systems for nanoscience", *Journal of Nanoparticle Research*, **2**, 413–418 (2000).
19. P.L. Gourley, "Biocavity laser for high-speed cell and tumor biology", *J. Phys. D: Applied Physics*, **36**, R228–R239 (2003).
20. W.P. Eatony and J.H. Smith, "Micromachined pressure sensors: Review and recent developments", *Smart Materials and Structures*, **6**, 530–539 (1997).
21. K.A. Jose, W.D. Suh, P.B. Xavier, V.K. Varadan, V.V. Varadan, "Surface acoustic wave MEMS gyroscope", *Wave Motion*, **36**, 367–381 (2002).
22. H.G. Yu, L.Z., K.D., R.W., S. Tadigadapa, S. Trolier-McKinstry, "Lead zirconate titanate MEMS accelerometer using interdigitated electrodes", *Sensors and Actuators, A* **107**, 26–35 (2003).
23. J.A. Walker, "The future of MEMS in telecommunications network", *J. of Micromechanics and Microengineering*, **10**, R1-R7 (2000).
24. W.V. and E. Palmer, "Qualification of 3-D space-grade memory cubes utilizing low temperature cofired ceramic (LTCC) technology," *Proceedings of the 1993 International Electronics Packaging Conference*, **1119**, 1003-1009 (1993).
25. R. Wood, R. Mahadevan, V. Dhuler, B. Dudley, A. Cowen, E. Hill, K. Markus, "MEMS microrelays", *Mechatronics*, **7**, 424-436 (1998).
26. C.T. Pan, "Silicon-based coupling platform for optical fiber switching in Free Space", *Journal of Micromechanics and Microengineering*, **14**, 129–137 (2004).
27. D.W. Monk, R.O. Gale, "The digital micromirror device for projection display", *Microelectronic Engineering*, **27**, 489-493 (1995).
28. Y. Liu, A. Borgioli, A.S. Nagra, R.A. York, "Distributed MEMS transmission lines for tunable filter applications", *International Journal of RF and Microwave Computer-Aided Engineering*, **11**, 254-260 (2001).
29. P.S. Petrou, I. Moser, G. Jobst, "BioMEMS device with integrated microdialysis probe and biosensor array", *Biosensors and Bioelectronics*, **17**, 859-865 (2002).
30. I. Horváth, P. Panayotatos, Y. Lu, "A Si MEMS microbearing with integrated safety sensors for surgical applications", *Microelectronics Journal*, **32**, 1–9 (2001).
31. S.S. Sastry, M. Cohn, F. Tendick, "Milli-robotic for remote, minimally invasive surgery", *Robotics and Autonomous Systems*, **21**, 305-316 (1997).
32. R.S. Shawgo, A.C.R. Grayson, Y. Li, M.J. Cima, "Bio-MEMS for drug delivery," *Current Opinion in Solid State and Materials Science*, **6**, 229–334 (2002).
33. A.K. Deisingh, "MEMS technology in analytical chemistry", *the Analyst*, **128**, 10-11 (2002).
34. C. Strandman, L. Smith, L. Tenerz, B. Hök, "A production process of silicon elements for a fiber-optic pressure sensor", *Sensors and Actuators, A* **63**, 69-74 (1997).
35. P.J. O'Connell, G.G. Guilbault, "Sensors and food quality", *Sensors: A Comprehensive Survey, Update 9*, John Wiley & Sons, 255-282 (2001).
36. D. De Bruyker and R. Puers, "Experimental characterization of the reference channel of a differential pressure sensor using pressure shock Waves", *Journal Micromechanics and Microengineering*, **11**, 390–396 (2001).
37. W.M. van Spengen, "MEMS reliability from a failure mechanisms perspective", *Microelectronics Reliability*, **43**, 1049–1060 (2003).

38. R. Muller-Fiedler, V. Knoblauch, "Reliability aspects of microsensors and micromechatronic actuators for automotive applications", *Microelectronics Reliability*, **43**, 1085–1097 (2003).
39. V. Cambel, S. Kicin, M. Kuliffayova, E. Kovacova, J. Novak, I. Kostic, A. Forster, "Preparation of patterned GaAs structures for MEMS and MOEMS", *Materials Science and Engineering*, **C 19**, 161–165 (2002).
40. J.-L. Leclercq, M. Garrigues, X. Letartre, C. Seassal and P. Viktorovitch, "InP-based MOEMS and related topics", *Journal of Micromechanics and Microengineering*, **10**, 287–292 (2000).
41. M. Mehregany, C.A. Zorman, "SiC MEMS: Opportunities and challenges for applications in harsh environments", *Thin Solid Films*, **355-356**, 518-524 (1999).
42. X. Wang, J. Engel and C. Liu, "Liquid crystal polymer (LCP) for MEMS: Processes and applications" *Journal of Micromechanics and Microengineering*, **13**, 628–633 (2003).
43. J.-M. Sallese, P. Fazan, "Switch and RF ferroelectric MEMS: A new concept", *Sensors and Actuators*, **A 109**, 186–194 (2004).
44. M.J. Feldstein, J.P. Golden, C.A. Rowe, B.D. MacCraith and F.S. Ligler, "Array biosensor: Optical and fluidic system", *Journal of Biomedical Devices*, **1:2**, 139-153 (1999).
45. A.E. Bruno, E. Baer, R. Völkel and C.S. Effenhauser, "Microoptical fluorescence detection for chip-based multiplexed analysis systems", *3rd International Conference on μ -TAS*, 281-285 (1998).
46. V. Lehmann, S. Rönnebeck, "MEMS techniques applied to the fabrication of anti-scatter grids for X-ray imaging", *Sensors and Actuators*, **A 95**, 202-207 (2002).
47. P. Nussbaum, R. Vökel, H.P. Herzig, M. Eisner, S. Haselbeck, "Design, fabrication and testing of microlens arrays for sensors and microsystems", *Pure Applied Optics*, **6**, 617-636 (1997).
48. M. Davidson, "A microlens direct-write concept for lithography", *Emerging Lithographic Technologies*, *SPIE Proceedings*, **3048**, 346-355 (1997).
49. N. Streibl, U. Nolscher, J. Jahns, and S. Walker, "Array generation with lenslet arrays", *Applied Optics*, **30**, 2739-2742 (1991).
50. M. Kufner, S. Kufner, "Monolithically integrated refractive optical interconnection networks", *Miniature and Microoptics*, *SPIE Proceedings*, **1992**, 150-158 (1993).
51. R. Göring and S. Glöckner, "The potential of transmittive microoptical systems for miniaturized scanners, modulators and switches", *Miniaturized Systems and Microoptics*, *SPIE Proceedings*, **3008**, 70-81 (1997).
52. P. Savander, H-J. Haumann, "Microlens array used for collimation of linear laser diode array", *Measurement Science Technology*, **4**, 541-543 (1993).
53. M.F. Dautartas, A.M. Benzoni, Y.C. Chen, G.E. Blonder, B.H. Johnson, C.R. Paola, E. Rice, and Y.-H. Wong, "A Silicon-based moving-mirror optical switch", *Journal of Lightwave Technology*, **10**, No. 8, (1992).
54. M. Hoffmann and E. Voges, "Bulk silicon micromachining for MEMS in optical communication systems", *Journal of Micromechanics and Microengineering*, **12**, 349–360 (2002).

55. J.-C. Roulet, H.P. Herzig, E. Verpoorte, N.F. de Rooij, R. Dandliker, "Integration of micro-optical systems for fluorescence detection in μ -TAS application", *Micro Total Analysis Systems 2000*, Kluwer Academic Publisher, 163-166 (2000).
56. G.A. Morton, "Image intensifiers and the scotoscope", *Applied Optics*, **3**, 651-672 (1964).
57. Hamamatsu Photonics K. K. Technical Report Sept. (2001).
58. K.F. Harsh, B. Su, W. Zhang, V.M. Bright, Y.C. Lee, "The realization and design considerations of a flip-chip integrated MEMS tunable capacitor", *Sensors and Actuators*, **A 80**, 108-118 (2000).
59. C. Gimkiewicz, D. Hagedorn, "Multichip module with free-space optical interconnects and VCSEL-solder-joints", *Microsystem Technologies*, **7**, 249-255 (2002).
60. A. Manz, H. Becker, "Microsystem technology in chemistry and life sciences", *Topics in current chemistry*, Springer-Verlag, **194**, 2, 28 (1998).
61. R.T. Kennedy, "Bioanalytical applications of fast capillary electrophoresis", *Analytica Chimica Acta*, **400**, 163-180 (1999).
62. G.J.M. Bruin, "Recent developments in electrokinetically driven analysis on microfabricated devices", *Electrophoresis*, **21**, 3931-3951 (2000).
63. J.R. Epstein and D.R. Walt, "Fluorescence-based fiber optic arrays: a universal platform for sensing", *Chemical Society Review*, **32**, 203-214 (2003).
64. G. Ocvirik, T. Tang and D.J. Harrison, "Optimization of confocal epifluorescence microscopy for microchip-based miniaturized total analysis systems", *the Analyst*, **123**, 1429-1434 (1998).
65. Y. Shi, P.C. Simpson, J.R. Scherer, D. Wexler, C. Skibola, M.T. Smith, and R.A. Mathies, "Radial capillary array electrophoresis microplate and scanner for high performance nucleic acid analysis", *Analytical Chemistry*, **71**, 5354-6361 (1999).
66. J.C. Roulet, K. Fluri, E. Verpoorte, R. Völkel, H.P. Herzig, N.F. de Rooij, R. Dandliker, "Micro-optical systems for fluorescence detection in μ -TAS applications", 3rd International Conference on μ -TAS, 287-290 (1998).
67. J.-C. Roulet, H.P. Herzig, E. Verpoorte, N.F. de Rooij, R. Dandliker, "Integration of micro-optical systems for fluorescence detection in μ -TAS application", *Micro Total Analysis Systems 2000*, Kluwer Academic Publisher, 163-166 (2000).
68. Y. Abdelaziez, and C.H. Ahn, "PLZT-based electro-optic modules for micromachined bio-photonics systems", *SPIE Proceedings*, **4561**, 171-182 (2001).
69. G. Schlingloff, H.-J. Kiel, and A. Schober, "Microlenses as amplification for CCD-based detection devices for screening applications in biology, biochemistry, and chemistry", *Applied optics*, **37**, 1930-1933 (1998).
70. Eugene Hecht, "Optics", Addison-Wesley Publishing, 2nd edition, 152,172 (1990).
71. G.H. Heartling, and C.B. McCampell, "A new longitudinal display mode for ceramic electrooptic devices", *Proceedings of IEEE*, (1972).
72. G.H. Heartling, "PLZT Electrooptic Materials and Applications", *Ferroelectrics*, **75**, 25-55 (1987).
73. R. Hook, "Micrographia", the Royal Society of London, (1665).
74. D. Gabor, "Improvement in or relating to optical systems composed of lenticules", UK patent, 541753 (1941).

75. D. Gabor, "Microscopy by reconstructed wave-fronts", *Proceedings of the Royal Society, A* **197**, 454-487 (1949).
76. Y. Baharav, B. Spektor, J. Shamir, D. Crowe, W. Rhodes, R. Stroud, "Wavefront sensing by pseudo-phase-conjugate interferometry", *Applied Optics*, **34**, 108-113, (1995).
77. T. Binnie, "Fast imaging microlenses", *Applied Optics*, **33**, 1170-1174 (1994).
78. K. Hamanaka, N. Hiroyuli, M. Oikawa, E. Oikuda, T. Kishimoto, "Multiple imaging and multiple Fourier transformation using planar microlens array", *Applied Optics*, **29**, 4064-4070 (1990).
79. F.W. Ostermayer, P.A.Kohl, R.H. Burton, Photoelectrochemical etching of integral lenses on InGaAsP/InP", *Applied Physics Letters*, **43**, 642-644 (1983).
80. D. Daly, "Microlens arrays", Taylor and Francis Publisher, Chapter 3 (2001).
81. S.-d. Moon, N. Lee and S. Kang, "Fabrication of a microlens array using micro-compression molding with an electroformed mold insert", *Journal of Micromechanics and Microengineering*, **13**, 98-103 (2003).
82. W.R. Cox, D.J. Hayes, T. Chen and D.W. Ussery, "Fabrication of micro-optics by microjet printing", *Miniature and Micro-Optics, SPIE Proceedings*, **2383**, (1995).
83. L.G. Commander, S.E. Day, D.R. Selviah, "Variable focal length microlenses", *Optics Communications*, **177**, 157-170 (2000).
84. H. Ren, Y.-H. Fan and S.-T. Wu, "Polymer network liquid crystal for tunable microlens arrays", *Journal of Applied Physics*, **D 37**, 400-403, (2004).
85. K.T. Gahagan, V. Gopalan, J.M. Robinson, Q.X. Jia, T.E. Mitchell, M.J. Kawa, T.E. Schlesinger and D.D. Stancil, "Integrated electro-optic lens/scanner in LiTaO₃ single crystal", *Applied Optics*, **28**, 1186-1190 (1999).
86. B. Bergea and J. Peseux, "Variable focal lens controlled by an external voltage: an application of electrowetting", *The European Physical Journal E*, **3**, 159-163 (2000).
87. N. Chronis, G.L. Liu, K.-H. Jeong, and L.P. Lee, "Tunable liquid-filled microlens array integrated with microfluidic network", *Optics Express*, **11**, 2370-2378 (2003).
88. Q.W. Song, X.M. Wang, and R. Bussjager, "Lanthanum-modified lead Zirconate Titanate ceramic wafer-based electro-optic dynamic diverging lens", *Optics letters*, **21**, 242-244 (1996).
89. T. Tatebayashi, T. Yamamoto and H. Sato, "Electro-optic variable focal-length lens using PLZT ceramic", *Applied Optics*, **30**, 5049-5055 (1991).
90. M. Kulishov, "Adjustable electro-optic microlens with two concentric ring electrodes", *Optics letters*, **23**, 1936-1938 (1998).
91. Personal communication with Dr. Mykola Kulishov.
92. V.I. Balakshy, "Scanning of images", *Soviet Journal of Quantum Electronics*, **6**, 965-971 (1979).
93. J.N. Mait, D.W. Prather and R.A. Athale, "Acousto-optic processing with electronic feedback for morphological filtering", *Applied Optics*, **31**, 5688-5699 (1992).
94. J. Xia, D. Dunn, T.-C. Poon and P.P. Banerjee, "Image edge enhancement by Bragg diffraction", *Optics Communications*, **128**, 1-7 (1996).
95. P.P. Banerjee, D. Cao and T.-C. Poon, "Basic image processing operations by the use of acousto-optics", *Applied Optics*, **36**, 3086-3089 (1997).

96. D. Cao, P.P. Banerjee and T.-C. Poon, "Image edge enhancement with two cascaded acousto-optic cells with counterpropagating sound", *Applied Optics*, **37**, 3007-3014 (1998).
97. P.P. Banerjee, D. Cao and T.-C. Poon, "Notch spatial filtering with an acousto-optic modulator", *Applied Optics*, **37**, 7532-7537 (1998).
98. S. Case, "Fourier processing in the object plane", *Optics Letters*, **4**, 286-288 (1979).
99. R. Gonzalez and R. Woods, *Digital Image Processing*, Addison Wesley, New York, (1993).
100. D. Cao, *AO Interaction Transfer Functions and Applications to Image Processing*, PhD Thesis, University of Alabama in Huntsville (1998).
101. P.E. Shames, P.-C. Sun and Y. Fainman, "Modeling of scattering and depolarization electro-optic devices. 1 Characterization of Lanthanum-modified Lead Zirconate Titanate" *Applied Optics*, **37**, 3717-3725 (1998).
102. Y. Xiang, "Focus retrocollimated interferometry for focal-length measurements", *Applied Optics*, **41**, 3874-3885 (2002).
103. J.D. Mansell and E.K. Gustafson, "Focal plane position detection with a diffractive optic for Shack-Hartmann wave-front sensor fabrication", *Applied Optics*, **40**, 1065-1073 (2001).
104. A. Büttner and U.D. Zeitner, "Calculation of the average lenslet shape and aberrations of microlens arrays from their far-field intensity distribution", *Applied Optics*, **41**, 6841-6848 (2002).
105. R. Gerchberg, and W. Saxton, "A practical algorithm for the determination of phase from image and diffraction plane pictures", *Optik (Stuttgart)*, **35**, 237-246 (1972).
106. P.P. Banerjee and T.-C. Poon, "Principles of applied optics", Aksen Associates Inc. Publisher, (1991).
107. M. Sheik-bahae, A.A. Said, and E.W. Van Stryland, "High-sensitivity, single-beam n_2 measurements", *Optics Letters*, **14**, 955-957 (1989).
108. P. Das, "Laser and optical engineering", Springer-Verlag, 109 (1991).
109. M. Born, and E. Wolf, "Principles of optics", Cambridge University Press, 7th edition, 442-443 (1999).
110. G.R. Laguna, "A production polishing process for thin PLZT wafers", *Ferroelectrics*, **27**, 187-190 (1980).
111. The RCA cleaning procedure, developed by RCA laboratories (1970), has three major steps used sequentially:
 1. Removal of insoluble organic contaminants with a 5:1:1 $\text{H}_2\text{O}:\text{H}_2\text{O}_2:\text{NH}_4\text{OH}$ solution (SC1).
 2. Removal of a thin silicon dioxide layer where metallic contaminants may accumulated as a result of (I), using a diluted 50:1 $\text{H}_2\text{O}:\text{HF}$ solution.
 3. Removal of ionic and heavy metal atomic contaminants using a solution of 6:1:1 $\text{H}_2\text{O}:\text{H}_2\text{O}_2:\text{HCl}$ (SC2).
112. G.H. Heartling, and C.B. McCampell, "A New longitudinal display mode for ceramic electrooptic devices", *Proceeding of IEEE*, April (1972).
113. W.D. Smith and C.E. Land, "Scattering mode ferroelectric photoconductor image storage and display devices", *Applied Physics Letter*, **20**, 169-171 (1972).
114. L.M. Levison, "Electronic ceramics properties, devices and applications", Mercel Dekker Publisher, **398**, 442-445 (1988).

115. FEMLAB technical computing magazine
116. A. Sheffer, and A. Üngör, "Efficient adaptive meshing of parametric models", ACM Symposium on Solid Modeling and Applications, Ann Arbor, MI, 59-70 (2001).
117. T.-C. Poon, and P.P. Banerjee, "Contemporary optical image processing with MATLAB", Elsevier Science, Chapter 2 (2001).
118. M. McNeill and T.-C. Poon, "Gaussian-beam shaping by acousto-optic Bragg diffraction", Applied Optics, **33**, 4508-4515 (1994).
119. J. Chrostowski and C. Delisle, "Bistable optical switching based on Bragg diffraction", Optics Communications, **41**, 71-81 (1982).
120. J. Chrostowski, R. Vallee, and C. Delisle, "Self-pulsing and chaos in acousto-optic bistability", Canadian Journal of Physics, **63**, 1143-1148 (1983).
121. H. Jerominek, C. Delisle, J.Y.D. Pomerleau and R. Tremblay, "Bistability, optical regenerative oscillations and chaos in an integrated acousto-optic device", Canadian Journal of Physics, **63**, 227-233 (1985).
122. P.P. Banerjee, U. Banerjee and H. Kaplan, "Response of an acousto-optic device with feedback to time-varying inputs", Applied Optics, **31**, 1842-1852 (1992).
123. T.-C. Poon and P.P. Banerjee, "Contemporary optical image processing with MATLAB", Elsevier Science, 111-117 (2001).
124. S. Franco, "Design with operational amplifiers and analog integrated circuits", McGraw-Hill, Chapter 2 (1998).
125. K. Eda, K. Onishi, H. Sato, Y. Taguchi and M. Tomita, "Direct bonding of piezoelectric materials and its applications", IEEE Ultrasonic Symposium, 299-308 (2000).
126. R.C. Budhani, S. Prakash, H.J. Doerr and R.F. Bunshah, "Oxygen enhanced adhesion of platinum films deposited on thermally grown alumina surfaces", Journal of Vacuum Technologies A, **4** (6), 3023-3024 (1986).
127. "Robust Group III Light Emitting Diode for high reliability in standard packaging applications" Patent Application [US 0030301453], Oct 2003.
128. N. Armstrong, C. Carter, C. Donley, A. Simmonds, P. Lee, M. Brumbach, B. Domercq and S. Yoo, "Interface modification of ITO thin films: organic photovoltaic cells", Thin Solid Films, **445**, 342-352 (2003).
129. A. Levstik, V. Bonnar, Z. Kutnjak, and M. Kosec, "Fatigue and piezoelectric properties of Lead Lanthanum Zirconate Titanate ceramics", Journal of Applied Physics, **31**, 2894-2897 (1998).
130. P. Shames, P.C. Sun, and Y. Fainman, "Modeling and optimization of electro-optic phase modulator" SPIE Proceeding, **2693**, 787-796 (1996).
131. P.E. Shames, P.C. Sun, and Y. Fainman, "Modeling of scattering and depolarizing electro-optic devices. II. Device simulation", Applied Optics, **37**, 3726-3734 (1998).
132. P.F. Baude, C. Ye, T. Tamagawa, D.L. Polla, "Fabrication of sol-gel derived ferroelectric $\text{Pb}_{0.865}\text{La}_{0.09}\text{Zr}_{0.65}\text{Ti}_{0.35}\text{O}_3$ optical waveguides", Journal of Applied Physics, **73**, 7960-7962 (1993).

R702031618